

AKBAR DARABI

**Detection and Estimation of Defect Depth in Infrared Thermography
Using Artificial Neural Networks and Fuzzy Logic**

Thèse
présentée
à la Faculté des études supérieures
de l'Université Laval
pour l'obtention
du grade de Philosophiae Doctor (Ph. D.)

Département de génie électrique et de génie informatique

FACULTÉ DES SCIENCES ET DE GÉNIE

UNIVERSITÉ LAVAL

QUÉBEC

AOÛT 2000



National Library
of Canada

Acquisitions and
Bibliographic Services

395 Wellington Street
Ottawa ON K1A 0N4
Canada

Bibliothèque nationale
du Canada

Acquisitions et
services bibliographiques

395, rue Wellington
Ottawa ON K1A 0N4
Canada

Your file Votre référence

Our file Notre référence

The author has granted a non-exclusive licence allowing the National Library of Canada to reproduce, loan, distribute or sell copies of this thesis in microform, paper or electronic formats.

The author retains ownership of the copyright in this thesis. Neither the thesis nor substantial extracts from it may be printed or otherwise reproduced without the author's permission.

L'auteur a accordé une licence non exclusive permettant à la Bibliothèque nationale du Canada de reproduire, prêter, distribuer ou vendre des copies de cette thèse sous la forme de microfiche/film, de reproduction sur papier ou sur format électronique.

L'auteur conserve la propriété du droit d'auteur qui protège cette thèse. Ni la thèse ni des extraits substantiels de celle-ci ne doivent être imprimés ou autrement reproduits sans son autorisation.

0-612-55806-1

Canada

Résumé

Les méthodes d'évaluation non destructive (ÉND) jouent actuellement un rôle grandissant dans les technologies modernes. Ces méthodes utilisent différentes techniques de mesure afin d'évaluer l'intégrité d'une structure ou d'un matériau sans l'endommager. Elles sont utilisées dans le domaine médical, sur la chaîne de production, pour des essais de structure et dans le domaine militaire. L'une de ces méthodes d'inspection concerne l'évaluation non destructive par thermographie (ÉNDT). Cette méthode est complètement sans contact et peut inspecter une grande surface dans un intervalle de quelques secondes. L'ÉNDT est aussi intéressante pour la détection de défauts dans les plastiques renforcés avec fibres de carbone (PRFC) qui sont largement utilisés en industrie aérospatiale, en industrie automobile et dans d'autres industries.

À cause de la nature non linéaire complexe du problème thermique inverse, l'ÉNDT a été considérée depuis plusieurs années comme une méthode qualitative d'inspection. Récemment, les réseaux de neurones ont été appliqués à l'ÉNDT afin d'extraire des informations quantitatives à partir d'images infrarouges. Les réseaux de neurone (RN) peuvent manipuler des problèmes non linéaires complexes à partir de données partiellement disponibles ou bruitées. Les travaux de recherche en ÉNDT quantitative basés sur les RN, ont jusqu'à présent été appliqués à des matériaux homogènes comme l'aluminium ou le plastique et la majorité de ces travaux utilisent des données expérimentales afin d'entraîner et tester l'architecture du réseau.

Cette thèse traite en premier lieu des problèmes de conduction thermique en 3-D pour modéliser des échantillons asymétriques ou non homogènes inspectés en thermographie pulsée (TP). La solution numérique est présentée. La solution analytique du problème de conduction thermique en 1-D est donnée afin de comparer la précision de la solution numérique. Cette solution analytique a été obtenue en utilisant le théorème de Duhamel. L'implantation de l'approche numérique dans une architecture parallèle comme l'ordinateur MasPar est brièvement expliquée. Les principes de base des RN et de la logique floue sont étudiés. L'inspection quantitative des matériaux composites tels les CFRP a été effectuée en appliquant deux RN respectivement comme détecteur de défauts et estimateur de profondeur de défauts et ce, en se basant sur l'algorithme de rétropropagation. Ces réseaux ont été testés avec des données de simulation provenant de la modélisation numérique de la conduction de chaleur proposée. Enfin, pour résoudre le problème d'entraînement des RN de type perceptron multicouches relié à l'algorithme de rétropropagation qui est à la fois très lent et incertain, un estimateur de profondeur est suggéré. Celui-ci se base sur un système en logique neuro-floue. Les deux approches proposées pour la technique quantitative d'ÉNDT, à savoir les RN et la logique neuro-floue, ont été testées en utilisant des données expérimentales et de simulation.

Résumé Court

À cause de la nature non linéaire complexe du problème thermique inverse, l'ÉNDT (Évaluation Non Destructive par Thermographie) a été considérée depuis plusieurs années comme une méthode qualitative d'inspection. Récemment, les réseaux neurones ont été appliqués à l'ÉNDT afin d'extraire des informations quantitatives à partir d'images infrarouges. Les réseaux de neurone (RN) peuvent manipuler des problèmes non linéaires complexes à partir de données partielles ou bruitées. Les travaux de recherche en ÉNDT quantitative basés sur les RN, ont jusqu'à présent été appliqués à des matériaux homogènes comme l'aluminium ou le plastique et la majorité de ces travaux utilisent des données expérimentales afin d'entraîner et tester l'architecture de tels réseaux. Dans cette thèse, l'inspection quantitative des matériaux composites tel le graphite époxy a été effectuée en appliquant des approches de RN et de logique neuro-floue. Les estimateurs de profondeur de défaut et le détecteur proposés sont formés avec des données simulées extraites de notre modélisation numérique de la conduction de chaleur appliquée à la thermographie infrarouge (TI). ~~Des approches RN et de logique neuro-floue appliquées à l'ÉNDT quantitative ont été testées en utilisant des données simulées et expérimentales.~~

Abstract

Nondestructive evaluation (NDE) methods are now playing an increasing role in modern technology and human living systems. These methods use various measurement techniques to evaluate the integrity of a structure or material without imposing harmful effect on the item. They find applications in medical, production line, structure testing and military fields among others. One such inspection method is called the thermal nondestructive evaluation (TNDE) technique. This method is totally non-contact and can inspect a large area in a matter of few seconds. TNDE is also attractive for detection of defects in Carbon Fiber Reinforced Plastics (CFRP) which are widely used in aerospace, car and other industries.

Due to the complex non-linearity nature of the inverse thermal problem, for long time TNDE has been limited as a qualitative inspection methods. Recently, neural networks have been applied to TNDE to extract quantitative information from recorded infrared images. Neural networks (NN) can handle complex non-linear problems with access to partially available or noisy data. Up to now, the quantitative TNDE research works based on developed NNs, were applied to homogenous material such as aluminum or plastic and most of them used experimental data to train network architecture.

This thesis first deals with 3-D heat conduction problems to model asymmetrical or non-homogenous samples inspected in pulsed thermography (PT), the numerical solution

is then developed. Analytical solution of the 1-D heat conduction problem in PT is given to compare the numerical solution precision. This analytical solution is found using Duhamel's theorem. Implementation of the numerical approach on a parallel architecture such as the MasPar computer is briefly explained. Fundamentals of supervised NN and fuzzy logic are studied. Quantitative inspection of composite materials such as CFRP is approached by applying two NN as defect detector and defect depth estimator based on the back propagation algorithm. These networks are trained with simulated data extracted from the proposed numerical heat conduction modeling. Finally, in order to solve the training problem of multilayer perceptron neural networks using the back propagation algorithm which is generally slow and uncertain, a depth estimator is suggested. It is based on a neuro-fuzzy system. Both NN and neuro-fuzzy approaches to quantitative TNDE are tested using simulated and experimental data.

Short Abstract

Due to complex non-linearity nature of inverse thermal problem, TNDE was limited to be a qualitative inspection method for many years. Recently, neural networks have been applied to TNDE to extract quantitative information from recorded infrared images. Neural networks (NN) can handle complex non-linear problems with access to partially available or noisy data. The quantitative TNDE research works based on NN, which have been carried out by now, are applied to homogenous material such as aluminum or plastic and most of them use experimental data to train suggested network architecture. In this thesis, Quantitative inspection of composite materials such as CFRP is treated by applying NN and neuro-fuzzy approaches. The proposed defect depth estimators and defect detector are trained with simulated data extracted from our numerical heat conduction modeling applied to infrared thermography (IT). Both NN and neuro-fuzzy approaches to quantitative TNDE are tested using simulated and experimental data

Acknowledgements

Thanks God who is most merciful and compassionate.

I wish to thank whom, they kindly encouraged me during my studies in Iran and abroad. I wish to express my gratitude and appreciation to my supervisor Prof. Dr. Xavier Maldague for his cordially guidance and advice during both my M. Sc. and Ph. D. studies at Université Laval.

I would also to present my sincere appreciation to all my professors, members of guiding committee and external examiners of my defence.

Special acknowledgement is extended to Iranian nation and the Ministry of Culture and Higher Education of the Islamic Republic of Iran for awarding me Graduate Studies Scholarship.

I would also to thank all my dear family members especially my father, my mother, my wife, Akram and her family, my sons, Hamed, Sajad and Mohammad-Hosseini, my brothers and sisters for their continuous love, support and patience. This thesis is dedicated to my family.

Akbar Darabi

August, 2000, Québec

Table of Contents

Résumé.....	ii
Résumé Court.....	iv
Abstract.....	v
Short Abstract	vii
Acknowledgements.....	viii
Table of Contents.....	ix
List of Figures	xiv
List of Tables	xxii
List of Abbreviation and Symbols	xxiii

CHAPTER 1

Introduction.....	1
1.1 Introduction.....	1
1.2 Infrared Thermography.....	3
1.2.1 Passive Thermography.....	3
1.2.2 Active Thermography	4
1.3 Artificial Neural Networks	6

1.4 Related works.....	8
1.5 Research Objectives.....	9
1.6 Thesis outline	11
1.7 References.....	13

CHAPTER 2

A Review of Transient Heat Transfer Modeling Applied to

Infrared Thermography	17
2.1 Introduction.....	17
2.2 Fundamentals of Heat Transfer.....	18
2.2.1 Conduction heat transfer	18
2.2.2 Convection Heat Transfer.....	19
2.2.3 Radiation Heat Transfer.....	20
2.3 Finite Difference Modeling.....	21
2.3.1 Mathematical Approach.....	22
2.3.2 Nodes on the Surface	23
2.3.3 Nodes Inside the Sample.....	24
2.3.4 Nodes on an Adiabatic(insulated) Boundary	25
2.3.5 Stability Criteria.....	26
2.4 Analytical Solution of the Heat Conduction Problem in Active IR Thermography	29
2.5 Delamination Model Description.....	33
2.6 Conclusion and Contribution	37
2.7 References.....	39

CHAPTER 3

Massively Parallel Implementation of the Heat Transfer Problem

in IR Thermography.....	40
3.1 Introduction.....	40
3.2 SIMD Processing	41
3.3 MasPar Parallel Processor.....	41
3.4 Implementation of the Direct problem on MasPar	43
3.4.1 Initialization (kx, ky, kz, Cp, r, Dx, Dy and Dz)	44
3.4.2 Restriction of Boundary Conditions to Parallel Algorithm	45
3.4.3 Communication.....	45
3.5 Delamination Model Implementation on MasPar.....	47
3.6 Advantages of the Direct Problem Implementation on MasPar System.....	52
3.7 Conclusion	55
3.8 References.....	56

CHAPTER 4

Artificial Neural Networks	57
4.1 Introduction.....	57
4.2 Artificial Neurons	58
4.3 Network Architectures	60
4.4 Learning	61
4.5 Perceptron Learning Rule	61
4.6 Back-Propagation Learning Rule.....	66
4.7 Conclusion	72

4.8 References	74
----------------------	----

CHAPTER 5

Neural Networks Based Defect Detection in TNDE	75
5.1 Introduction	75
5.2 Thermal Data	77
5.3 Defect Detector Network	82
5.4 Experimental Results for Detector Network.....	91
5.5 Defect Depth Estimation Network.....	99
5.6 Experimental Results for Estimator Network.....	105
5.7 Conclusion	108
5.8 References.....	109

CHAPTER 6

Defect Characterization in TNDE Based on Neuro-Fuzzy Computation

Techniques	112
6.1 Introduction.....	112
6.2 Fuzzy Logic	113
6.2.1 Definitions.....	113
6.2.2 Fuzzy Reasoning Mechanism	121
6.3 Neuro-Fuzzy Defect Depth Estimation.....	131
6.4 Conclusion	140
6.5 References.....	141

CHAPTER 7

Conclusion143

 7.1 Summary143

 7.2 Contributions146

 7.3 Future work.....146

 7.4 References.....148

APPENDIX

The Analytical Solution of the Heat Conduction Problem Programming Code.....149

List of Figures

Figure 1.1	Typical TNDE configuration using the passive method.	4
Figure 1.2	Schematic diagram of a typical active infrared thermography set-up.	6
Figure 1.3	Typical surface temperature variation curve in active thermography.	6
Figure 1.4	Two possible architectures for flaw detector and estimator network in IT. .	11
Figure 2.1	Electromagnetic radiation spectrum (wavelength λ in \log_{10} m).	21
Figure 2.2	Three-dimensional model for planar geometry showing elementary volume...	22
Figure 2.3	Expanded view of control volume surrounding arbitrary surface node (k,m,0)	23
Figure 2.4	Expanded view of control volume surrounding arbitrary interior node (k, m, n).	25
Figure 2.5	Expanded view of control volume surrounding arbitrary adiabatic boundary node (k, m, n).	26
Figure 2.6	General conduction node.	27
Figure 2.7	A step-shape function as the time dependent boundary condition	30
Figure 2.8	(a) Model heating (b) shape of the heat pulse.	31
Figure 2.9	Temperature evolution curve on the heated surface of a CFRP sample (without defect), obtained from the analytical solution of the problem.	33

Figure 2.10	Schematic diagram of the modeled CFRP sample.	34
Figure 2.11	The computed temperature evolution over defect and sound areas on the CFRP sample surface	36
Figure 2.12	Surface temperature evolution of CFRP block computed using analytical and numerical solution methods.	37
Figure 3.1	MasPar System Diagram.	42
Figure 3.2	a) physical b) computational storage scheme.....	44
Figure 3.3	Partitioning of the processor-element array into different subset for taking into account the boundary conditions in the computational algorithm.	45
Figure 3.4	X-Net communication through 8 nearest neighbors on MasPar.	46
Figure 3.5	(a) shows the points (defect) in third layer having a value of 0.0042 (thermal conductivity of Teflon TM) and (b) shows the points (sound material) in third and 18th layer having a value of 0.008 (thermal conductivity of CFRP ()) both in	49
Figure 3.6	a) Temperature distribution on the surface (left array) and 18th layer (right array) of sample of Figure 2.10 which contains a delamination defect. (b) Time (s) of recording.	50
Figure 3.7	Temperature distribution images over 32 layers of modeled CFRP sample when the contrast is maximum on the surface. Notice the subtle differences that vanishes temperature deeper in the sample layer (8 and deeper).	51
Figure 3.8	Time dependence of (a) surface temperature and (b) the thermal contrast of CFRP modeled sample containing delamination defect in parallel simulation.	53
Figure 3.9	Time dependence of (a) surface temperature and (b) the thermal contrast of sequential version "TERMO.HEAT" for a similar CFRP modeled sample containing delamination defect.	54

Figure 4.1	A typical multiple-input neuron.	59
Figure 4.2	The most commonly used transfer functions in ANNs: (a)hard limit (b)linear (c) sigmoid transfer function.	60
Figure 4.3	A typical single neuron perceptron network.	62
Figure 4.4	A two-input single neuron perceptron.	64
Figure 4.5	Input vector and initial decision boundary for a two-input single neuron perceptron.	65
Figure 4.6	Final decision boundary for a two-input single neuron perceptron, NAND gate implementation problem.	65
Figure 4.7	A three-layer feed-forward neural network.	67
Figure 4.8	Estimated $\sin(x)/x$ function by a two layer feedforward neural network, 10 neuron with 'tansig' activation function in hidden layer and one output neuron with 'purelin' activation function. Bold dots, circle-dots, square-dots respectively correspond to training data, the network output for training data and the network output for test data.	71
Figure 4.9	The network's MSE, mean square error, during training procedure.	71
Figure 4.10	Estimated temperature evolution function and network performance: for two feedforward network with 18 neuron (top figures) and 30 neuron (bottom figures) in hidden layer.	72
Figure 5.1	An CFRP block sample, which contains five air delaminations of thickness 100 mm, defects at shown depth.	78
Figure 5.2	Temperature vs. time curves for simulated CFRP sample, (a) sample surface, (b) sound area, (c) defect areas, (d) central pixels of all five delamination-type defects (red) and one randomly chosen pixel of sound area (green) temperature curves.	79
Figure 5.3	Temperature contrast vs. time curves for one randomly chosen sound pixel and central pixels of five air defects which are located in the CFRP block at	

	depth 0.2, 0.6, 0.7, 1.0 and 1.4 mm (Figure 5.1). (a) ΔT -image, (b) contrast, (c) running-contrast and (d) normalized contrast.	82
Figure 5.4	A three layers defect detector network architecture	84
Figure 5.5	The maximal points of thermal contrast curves and corresponding desired outputs.	85
Figure 5.6	The simulated samples depth profile which were deployed to examine defect detector network performance.	86
Figure 5.7	Defect detector output images for nine different simulated data sets, white pixels represent defect areas.	87
Figure 5.8	Error images for the above defect detector output results. White pixels shows pixels incorrectly detected as defect or non-defect pixels.	87
Figure 5.9	Defect detector output images for the simulated data sets which are contaminated with a white Gaussian noise (a) $\sigma = 0.054$ and (b) $\sigma = 0.039$	89
Figure 5.10	A CFRP sample containing a T-shape air defect with shown depth profile.	90
Figure 5.11	The detector network output result: a) White area detected as defect; b) the error pixels (white) which are incorrectly classified as defect or sound pixels.	91
Figure 5.12	One of the simulated CFRP sample containing Teflon TM defects. It is used in the training procedure for experimental results: a) top-view of the sample; b) the sample depth profile.	92
Figure 5.13	The running contrast signal over Teflon TM defects A, B, C, D, E and sound area (dash-dotted curve) for the sample shown in Figure 5.11. The defects depth are respectively 0.9, 1.2, 0.5, 0.3, and 0.8 mm.	93
Figure 5.14	The running contrast signal curves for all defect E pixels which shows they can be classified in four categories.	94

- Figure 5.15 The CFRP sample layout which is used to test the experimental performance of the detector network. 95
- Figure 5.16 The detector network output results and maximum contrast images over defects #1 and #2. (a) maximum contrast image; (b) the network output image supposing average contrast as reference contrast; (c) the network output image supposing one of the upper-left pixels as sound pixel; (d) logical (AND) combination of images (b) and (c). 97
- Figure 5.17 The detector network output results and maximum contrast images for the CFRP sample containing two circular TeflonTM defects with 10mm diameter at depth 2 and 3 mm. (a) maximum contrast image; (b) the network output image supposing average contrast as reference contrast; (c) the network output image supposing one of the upper-left pixels as sound pixel..... 98
- Figure 5.18 The original and estimated defect depth profile for a sample which was used during training procedure: (a) original depth; (b) estimated depth for input data without noise; (c) estimated depth for contaminated input data with a Gaussian noise ($\sigma = 0.033$ and $\mu = 0$). 100
- Figure 5.19 The original and estimated depth images for a sample which was used during the training procedure: (a) original depth; (b) estimated depth for input data without noise; (c) estimated depth for contaminated input data with a Gaussian noise ($\sigma = 0.033$ and $\mu = 0$). 101
- Figure 5.20 The estimator network response to a data set which has not been used during training phase: (a) and; (b) original and; (c) estimated depth profile. 103
- Figure 5.21 Depth profiles of a CFRP sample which contains a T-shape air defect: (a) the modeled sample depth profile; (b) estimated depth profile; (c) the estimated depth profile with error pixels removed from the plot. 104
- Figure 5.22 The estimator neural network output for a CFRP sample containing TeflonTM defect: (a) 3D depth profile: (b) depth image (sample of Figure 5.14) 106

Figure 5.23	Filtered output of the estimator neural network for a CFRP sample containing Teflon TM defect: (a) 3D depth profile; (b) depth image (sample of Figure 5.14).	107
Figure 6.1	The characteristic functions for crisp sets A, B, and their union, intersection and complements.	115
Figure 6.2	The membership functions for fuzzy sets A (Child), B (Young), C (Adult).....	119
Figure 6.3	The membership functions for complement of fuzzy set A, union of fuzzy set A and its complement, intersection of fuzzy set A and its complement, and union of fuzzy sets A, B, and C.	120
Figure 6.4	Membership functions for the inputs variables x_1 and x_2 and the output variable y.	124
Figure 6.5	The reasoning process for a Mamdani fuzzy system with two inputs and one output variables four rules. Given inputs are $x = 30$ and $x = 35$. The output value is $y = 4.33$, black vertical bar on the right bottom. It is calculated by the centeriod method from the aggregated results of the rules.	125
Figure 6.6	The output surface of the system following the Mamdani reasoning method.	125
Figure 6.7	The reasoning process for a Sugeno fuzzy system with two input and one output variables and four rules where for given inputs $x_1 = 25$ and $x_2 = 40$. The output value is $y = 3.56$, thin bar on the right bottom. It is calculated by the centeriod method from the aggregated results of the rules.	128
Figure 6.8	The output surface of the system with Sugeno reasoning method	129
Figure 6.9	The reasoning process for a Sugeno fuzzy system with two inputs and one output variables and two rules. Given inputs are $x = 25$ and $x = 40$. The output value $y = 1.25$, as shown by the red thin bar on the right bottom.	130
Figure 6.10	The output surface of the Sugeno fuzzy system with two implication rules.....	131

- Figure 6.11 Normalized contrast curve on the surface of a CFRP sample over a TeflonTM subsurface defect at 0.7 mm depth. The circle, star and square points are respectively half-rise, half-decay and maximum contrast. Their occurrence time serves to define an input vector for the ANFIS depth estimator. The difference between half-rise and half-decay contrast amplitudes is due to their sampling time. 133
- Figure 6.12 Training set for ANFIS depth estimator. The vectors extracted from simulated data of CFRP samples containing TeflonTM defects at various depths. (a) half-rise contrast (b) maximum contrast (c) half-decay contrast (d) half-rise contrast time (e) maximum contrast time (f) half-decay contrast time (g) depth. 134
- Figure 6.13 Initial membership functions of input variables for ANFIS depth estimator: half-rise contrast (-hCmax), maximum contrast (Cmax), half-decay contrast (+hCmax), half-rise contrast time (-tCmax/2), maximum contrast time (tCmax), half-decay contrast time (+tCmax). 135
- Figure 6.14 Final membership functions of input variables for buried TeflonTM in CFRP samples ANFIS depth estimator: half-rise contrast (-hCmax), maximum contrast (Cmax), half-decay contrast (+hCmax), half-rise contrast time (-tCmax/2), maximum contrast time (tCmax), half-decay contrast time (+tCmax). 135
- Figure 6.15 RMSE (root mean squared error) curve for buried TeflonTM in CFRP samples ANFIS depth estimator. 136
- Figure 6.16 Depth profile for T-shape air defect buried in CFRP sample. (a) Original depth profile (b) estimated depth profile of air defect by ANFIS depth estimator (c) the estimated depth profile in which error defect pixels have been removed (d) the estimated depth profile error (f) the estimated depth profile error in which error defect pixels have been removed. 137
- Figure 6.17 3-D estimated depth profile of the subsurface air defect ANFIS depth estimator for T-shape air defect buried in CFRP sample. 138

- Figure 6.18 Estimated depth image of TeflonTM defect by ANFIS depth estimator for sample shown in Figure 5.15 (to be compared with Figure 5.16 (d), p. 97 and Figure 5.22, p. 106. 139
- Figure 6.19 TeflonTM defect ANFIS estimated depth image which has been filtered by a median filter. Two defect at depth between 0.25 mm and 0.35 are clearly seen. 140

List of Tables

Table 3.1	Simulation Parameters of CFRP block containing a Teflon TM gap as defect.	48
Table 5.1	Cincinnati Electronics IRC-160 noise standard deviation	88

List of Abbreviation and Symbols

NDE	Non-destructive Evaluation
TNDE	Thermal Non-destructive Evaluation
IT	Infrared Thermography
PT	Pulsed Thermography
PPT	Pulsed Phase Thermography
LT	Lock-in-Thermography
SNR	Signal-to-Noise Ratio
NN	Neural Network
ANN	Artificial Neural Network
NF	Neuro-Fuzzy
ANFIS	Adaptive-Network-Based Fuzzy Inference System
PVC	
CFRP	Carbon Fiber Reinforced Plastic
MasPar	Massively Parallel Computer
I/O	Input/Output

SIMD	Single Instruction, Multiple Data
PE	Processing Element
DPU	Data Parallel Unit
ACU	Array Control Unit
MPL	Massively Parallel Language
MPPE	MasPar Programing Environment
LMS	Least Mean Square
MSE	Mean Square Error
MT	Modulated Thermography
MLP	Multi-layer Perceptron
BK	Back-Propagation
TSK	Takagi-Sugeno-Kang
LSE	Least Squares Estimate
NN-MLP	Nearest-Neighbor-Based Multilayer Perceptron
<i>T</i>	Temperature
<i>t</i>	Time
<i>z</i>	Defect depth
α	Thermal diffusivity
<i>k</i>	Thermal conductivity
C_p	Specific heat capacity
ρ	Mass density

μ	Thermal diffusion length
ω	Angular frequency
q	Heat flow
h_{conv}	Convection coefficient
$ Fo$	Fourier number

CHAPTER 1

Introduction

1.1 Introduction

Modern nondestructive evaluation (NDE) methods are now playing an increasing role in all aspects of material productions and applications [1]. As it is well known, NDE uses various non-invasive measurement techniques to determine the integrity of a structure, component, or material without destruction of that item. During manufacturing NDE is used to produce defect-free components in a cost-effective manner. During service life of the component, assembly, or system, NDE is used to ensure that system fitness for service is maintained and, in some instances, to assess the remaining life effectiveness.

Nondestructive evaluation involves diverse fields of applied physics, expert systems, neural network, fuzzy logic, computer science, electronics and electrical engineering, materials science and engineering, mechanical engineering, and structural engineering. To meet the increased demand for robust and effectiveness inspection in

complex NDE tasks, neural networks and fuzzy logic have been recently deployed in many problems [2], [3], [4], [5], [6], [7], [8], [9].

Ultrasonic, X-rays, eddy current and magnetic flux leakage techniques are the most known among NDE techniques [10]. One of the new method, which has emerged recently, is infrared thermography. It is a totally non-contact, non-invasive imaging method which is able to inspect a large area in a matter of few seconds. Infrared thermography is used routinely in industrial applications such as process control, in-process inspection, acceptance inspection (e.g. to provide quantitative information about subsurface flaws in aircraft structures), monitoring thermal conditions of electric power lines, district heating networks, electric circuits and components, heat exchangers, pipes and its insulations, cooling towers, and various machines and motors. Using infrared thermography in conjunction with other NDE methods also provides a total perspective of operating conditions of equipments and processes. Recent advances in infrared imaging technology, specifically development of high-density imaging sensors have opened new levels of applications such as detection of subsurface delaminations and disbond defects in composites, sandwich panels and coated materials [11], [12].

The effectiveness of the TNDE (Thermal Non-destructive Evaluation) technique depends not only on the instrumentation, but also on techniques that are used in conjunction with inspection to efficiently and accurately extract relevant information from acquired data [8]. Many processing techniques have been developed to clearly reveal and provide quantitative information concerning subsurface defects in TNDE. One such approach employs artificial neural networks which have recently obtained considerable success in a variety of applications [13], [14], [15], [16], [17]. Neural networks are known for their high processing speed, high classification accuracy, low sensitivity to noise, and easy thresholding capability in order to provide binary images required for automated detection.

In the present research, various interconnected feed-forward multi-layered neural networks and neuro-fuzzy systems are designed and evaluated in order to reveal and estimate defect depth in the inspected component by TNDE. By using the entire temperature versus time curve or thermal contrast curve as inputs to the neural networks

and through suitable training, such networks can be made to respond in a desired way to various features of thermal curves. Comparisons are made between neural network and neuro-fuzzy system results, simulations from a dedicated thermal model and experimental results in terms of specimen parameters and output signal (thermal contrast) estimation.

1.2 Infrared Thermography

Recent years have seen a considerable development in infrared sensing and imaging instruments for terrestrial use, particularly for military, battlefield, airborne and non-destructive testing. Infrared system senses infrared radiant energy and produce useful electrical signals proportional to the temperature of the material surface to be inspected. Instruments using infrared detectors and optics to gather and focus energy from the material onto these detectors are capable of measuring material surface temperatures with sensitivities down to 20 *mK* (K is for Kelvin temperature) and with response time in the microsecond range [10]. These important features, which are due to traveling of the measured energy from the material surface to the sensor at the speed of light, allowed the field of infrared radiation thermometry to expand into real-time thermal scanning and thermal mapping.

Infrared thermography is generally classified in two methods, passive and active thermography.

1.2.1 Passive Thermography

In many applications mentioned above, patterns are naturally obtained either statically (“one shot”) or dynamically (recording of subsequent instantaneous values at the moment measurements are made). There are numerous instances where such thermal conditions are exploited by TNDE to reveal material or structural characteristics in the inspected parts. For example, the thermogram recorded from the outside surface of an insulated pipe carrying a hot fluid is relatively isothermal and warmer than ambient air. Insulation defects or voids will induce warm anomalies (often designated as hot spots) which will appear on the thermogram, allowing the thermographer to pinpoint areas of defective or damaged insulation. Because of the constant heat flow from the hot fluid through the insulation to the ambient air, a static distinctive thermal pattern on the sample

surface, is obtained [10]. Figure 1.1 illustrates a typical infrared TNDE configuration using the passive method.

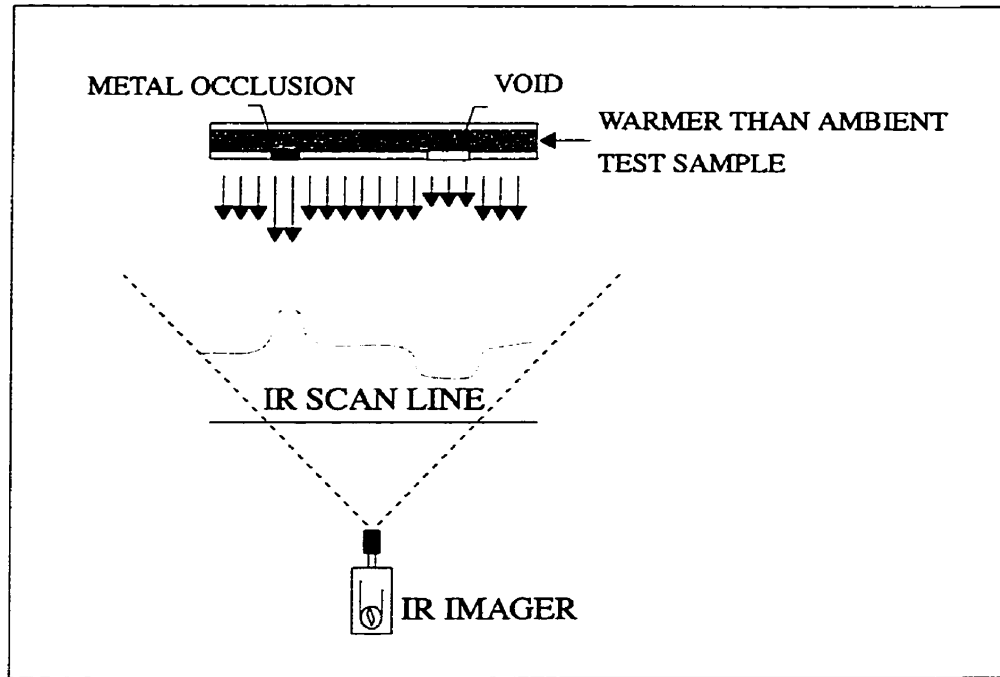


Figure 1.1 Typical TNDE configuration using the passive method.

1.2.2 Active Thermography

When there is no heat flow through the material or the structure to be inspected, an active approach is used to generate a transient heat flow. In active infrared thermography, the sample is heated by an external controlled heat source and its surface temperature is monitored as a function of time through changes of emitted infrared radiation. The specific thermal properties of the material under test influence transport of heat thus causing surface temperature to change with respect to areas with different thermal properties. This allows to image subsurface anomalies such as disbounds [1]. Active infrared thermography is an economical and reliable NDE inspection method for large complex structures. It has specific advantages over other NDE methods. It offers single side inspection while large areas can be measured on complex geometries without significant difficulties [10]. Depending on the heat source, active thermography is referred to pulsed thermography (PT) or lock-in-thermography (LT) [2], [18].

In PT, an heating pulse from a laser, flash lamp or microwave heating source deposits heat on the sample surface in a short time [2], [19]. Following this pulse, the surface temperature increases linearly as $t^{1/2}$ due to the combined effects of direct heating and thermal diffusion (t is the time variable). Consequently, thermal diffusion from the surface changes the temperature near the defect region after a thermal transit time approximately equal to z^2/α , where z is the defect depth and α is the thermal diffusivity ($\alpha=k/\rho C_p$ with k the thermal conductivity, C_p the specific heat, and ρ the mass density).

In LT, a sine-shaped periodical heat flux at a given frequency ω stimulates the sample surface. Following periodical heat injection, the surface temperature in stationary regime is recorded and time-delayed thermal waves due to defects can then be monitored. The phase image in LT is relatively independent of emitted thermal power and thus the SNR (signal-to-noise ratio) is improved with respect to PT while uniform heating sources are not mandatory. Using the phase image, LT allows to detect defects at depths up to about twice the thermal diffusion length (μ) given by [2], [18]:

$$\mu = \sqrt{2k/\omega\rho C_p}. \quad (1.1)$$

In this thesis PT active thermography will be of interest. A typical PT active infrared thermography set-up configuration is shown in Figure 1.2. Here a flash-lamp heating source is used to inject the initial thermal perturbation heating pulse. After a quick heating of the sample, the temperature evolutions both over a surface point of the part and over a subsurface anomaly such as a delamination (e.g. presence of a subsurface air layer) are plotted in Figure 1.3 [20].

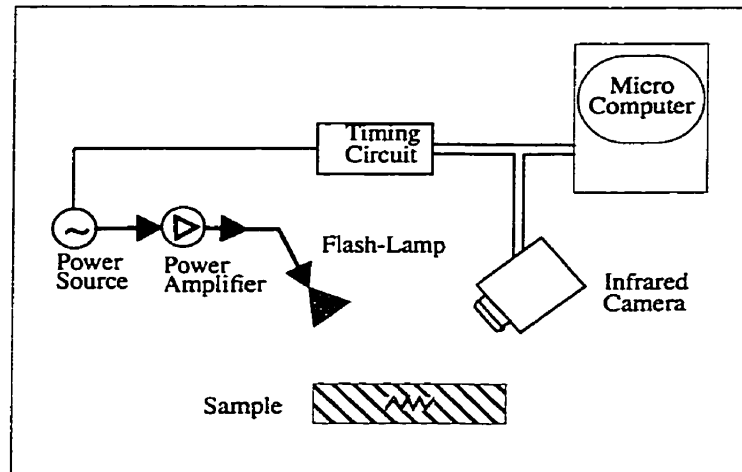


Figure 1.2 Schematic diagram of a typical active infrared thermography set-up.

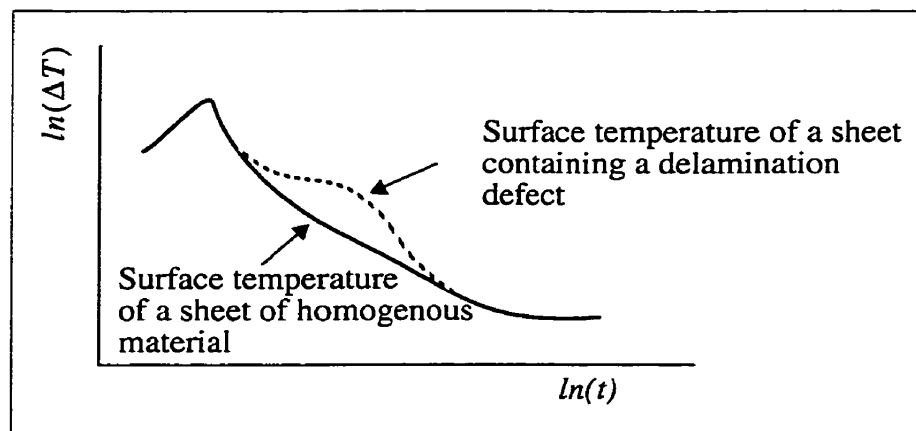


Figure 1.3 Typical surface temperature variation curves in active thermography.

1.3 Artificial Neural Networks

Nowadays, sequential digital computers allow to deal with many tasks such as electronic communication, database (creation, manipulation, and maintenance), scientific and mathematical problem solving, word processing, graphics, desktop publication, etc. Moreover, most of the simple control functions that simplify our household tools and

appliances and are now managed by digital electronics. In contrast, there are many problems that we are not able to solve due to their inherently parallel or complex structures not well fitted for sequential computer systems. For example, how can we recognize a man in a crowd from a mere glimpse of his face? A computer cannot perform such a recognition task with ease [21].

The human brain consists of a large number (approximately 10^{11}) of highly connected neurons which have many desirable characteristics not present in modern sequential computers [22]. Some of these characteristics are:

- massive parallelism,
- distributed representation and computation,
- learning ability,
- generalization ability,
- fault-tolerance, and
- low-energy consumption.

Our brain is able to organize neurons so as to perform highly complex, nonlinear, and distributed computations (e.g., perception, classification, prediction, and control of a process) much faster than the most powerful digital computer in existence today [21].

Inspired by biological neural networks, artificial neural networks (NN) consist of a large number of simple, highly interconnected nonlinear processing units (neurons) that operate in parallel. The neuron itself can be defined as a non-linear thresholding unit, which receives inputs and produces an output which is a function of the sum of these inputs. Each interconnection between neurons has an associated connection weight that can be adjusted to achieve the desired network behavior through a training process. A typical NN architecture is shown on Figure 1.4.

Although it is difficult to predict the future success of NN recently, different NN algorithms have been applied fruitfully to many problem areas. Advantages of NN include firstly, learning ability, and secondly versatile mapping capabilities from input to output. Moreover, NN can be deployed in applications for which it is not particularly easy to establish a direct input/output mathematical relationship. These information processing

capabilities make it possible for NN to solve complex problems which are decomposed into a number of relatively simple tasks [21]. Most interesting problems for computer scientists and engineers such as pattern classification, clustering, function approximation, prediction, optimization, content addressable memory, and control can be solved using NN [22].

1.4 Related works

Due to non-linear nature of IR thermography, its inverse problem has been studied for many years by research groups. Although, various analytical, numerical or empirical models were established for simple cases, defect classification and quantitative solution of problems such as defect depth and thermal properties still remain important research areas in this field [23], [24]. NNs have recently been applied to solve inverse problems in TNDE by many research groups because they can solve non-linear problems with noisy or partially missing data.

D. R. Prabhu and W. P. Winfree proposed two backpropagation NNs to detect and estimate corrosion in aircraft lap joints. The networks were trained using entire temperature versus time curves as input vectors and flaw/ no flaw or corrosion percentage as desired output. The combined result of these two networks shows both high classification and estimation accuracies [8].

Another research work was carried out on plastic material (PVC) by P. G. Bison, C. Bressan, R. Disarno, E. Grinzato, S. Marinetti and G. Manduchi. They also proposed two multi-layer perceptron NNs as detector and estimator of delamination defect depth in PVC. Maximum contrast and corresponding time of occurrence were considered as network inputs. The outputs were defect/nondefect status or defect depth. The authors mentioned the networks allow to identify delaminations inside an opaque body and estimate the depth quite well [25].

In an other attempt, H. Trétout, D. David, J. Y. Marin and M. Dessendre used different temporal thermal data signatures to examine NN ability as classifier on composite aerospace structures. They provided 500 simulated thermal curves as training set, one half corresponding to sound area and the other half correspond to defect areas. The results show

that the proposed NN can detect TeflonTM defects up to 1.5 mm under the surface of a CFRP sample [9].

Recently, Xavier Maldague, Yves Lergouët and Jean-Pierre Couturier [2] and Steve Vallerand, Akbar Darabi, X. Maldague [3] and Yves Lergouët, Akbar Darabi and Xavier Maldague [4] employed pulsed phase thermography (PPT) to detect and extract quantitative information based on NN. In these studies, the network input is the phase vector for each pixel and the output is its corresponding depth. The results show that a high sampling frequency is required to achieve quantitative analysis based on PPT [2], [4]. With respect to NN architectures and learning algorithms, published results demonstrated that the multi-layer perceptron using backpropagation learning algorithm provides better detection as compared to a Kohonen network [3].

1.5 Research Objectives

The main objectives of this research is to detect subsurface defects, characterize defect depth and size in non-homogeneous materials such as CFRP using classical transient heat conduction modeling and artificial neural network approaches.

Theoretically, solving the transient heat conduction equation with appropriate boundary conditions allows describing subsurface defects and anomalies of materials and complex structures [26]. The solution of the direct problem in infrared thermography provides useful information to interpret experimental data, optimize the active heat stimulation and scanning configuration, determine the limits of applicability of the thermographic approach and, especially in this study, train desired NN or neuro-fuzzy systems. As it is known, the direct problem allows the temperature distribution to be computed for known defect geometry and thermal properties. In the present study a numerical solution of the three dimensional heat conduction equation applied to TNDE is first given. This modeling allows us to take into account the lateral defect effects which are very crucial for non-homogeneous material in practice. The comparison of numerical solution results with analytical solution results of similar problems is also discussed.

In the present study, two interconnected feedforward multilayer NNs are proposed and evaluated in order to reveal and estimate depth of defect in the inspected component. We also propose a neuro-fuzzy depth estimator. The proposed network inputs are the entire temperature versus time curve or thermal contrast curve. The training is only done with theoretical data. Theoretical data is interesting for two major reasons. Firstly a large training set is required which is difficult to obtain with real experiments. Secondly laboratory samples are not enough representative [9].

For example an architecture as shown in Figure 1.4 will be defined to classify in a first step (flaw detector network) the thermal curves corresponding to each pixel of a sequence of infrared images and, in second step (estimator network) to proceed to the spatial analysis.

Comparisons will be made between the NN and neuro-fuzzy system results, simulations from the model and actual experimental results.

The proposed method is believed to offer advantages in term of speed and efficiency as compared to current inversion techniques (analytical, or based on empirical relationships) [2] [3] [8].

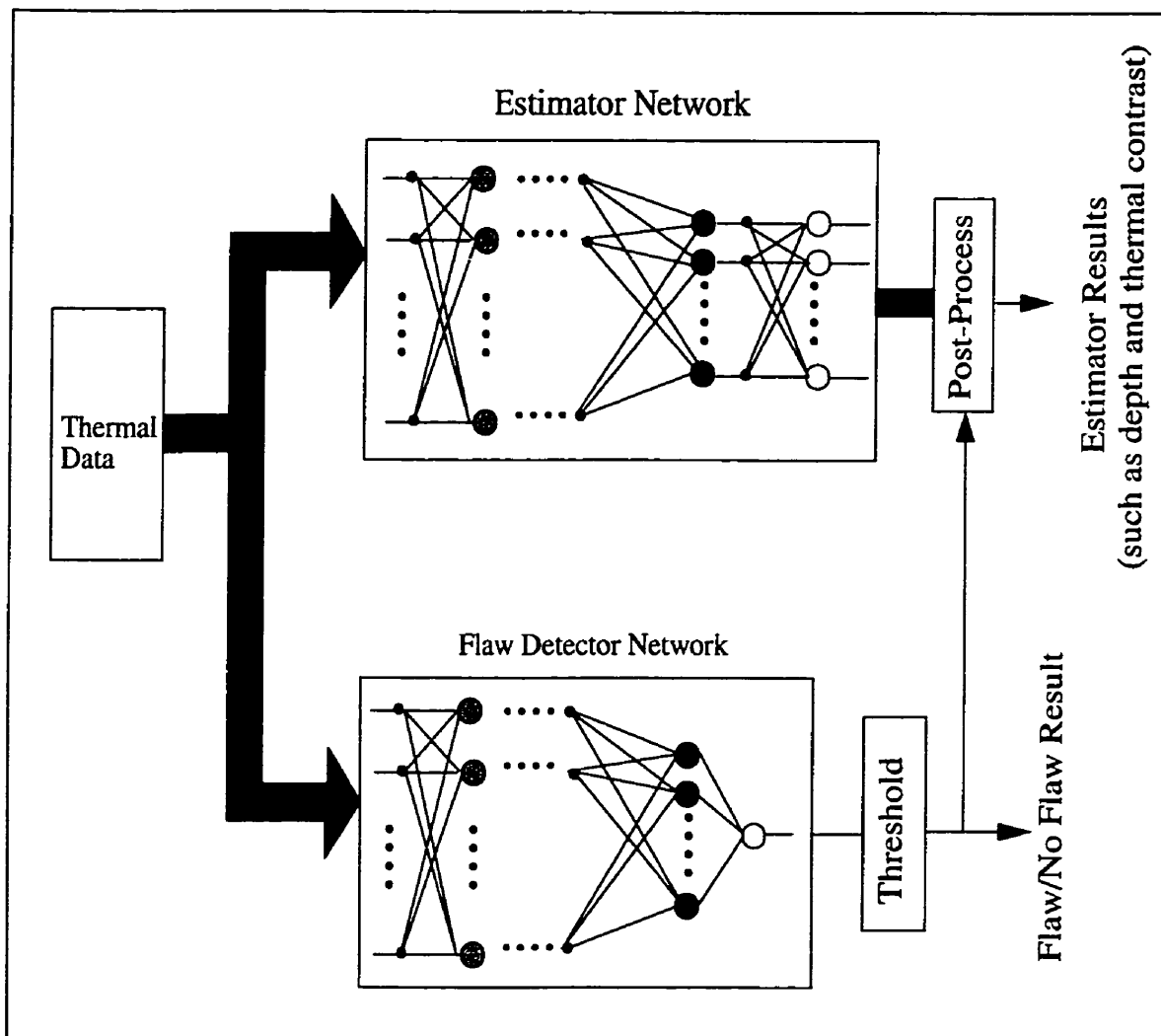


Figure 1.4 Two possible architectures for flaw detector and estimator network in TNDE.

1.6 Thesis outline

Chapter one has presented an introduction to TNDE field, current works and thesis objectives.

Chapter two is dedicated to analysis of the 3-D transient heat conduction problem applied to TNDE. The numerical solution is developed and equations for different boundaries and interior nodes are given. Then an analytical solution for 1-D heat

conduction is derived, based on Duhamel's theorem. Finally, the numerical solution results obtained for a defect-free CFRP block are compared with the analytical solution for a similar heat conduction problem in TNDE.

The implementation of the numerical modeling of heat conduction problem on a massively parallel machine (Maspar MP-1) is presented in chapter three. The modeling results are also compared with results from a commercial software available for modeling 2-D heat conduction problems.

NN basic theory for perceptron and multilayer feed-forward architecture is studied in chapter four. The ability of the multilayer backpropagation NN to solve nonlinear problem is examined with two examples. The first concerns the approximation of sinc function ($\sin(x)/x$) and the second, the approximation of thermal contrast function for a CFRP sample containing TeflonTM defects.

Chapter five is first concerned with a detailed analysis of thermal data. Then two NNs are proposed as flaw detector and defect depth estimator with training based on the backpropagation algorithm. These networks are trained to characterize both air and TeflonTM defects contained in CFRP samples. The network performance is tested using simulated data, contaminated simulated data with white noise and finally experimental data.

A brief fuzzy theory and neuro-fuzzy system fundamentals are given in chapter six. The neuro-fuzzy defect depth estimator is then proposed. The estimator performance is studied using simulated data, contaminated simulated data with white noise and experimental data. Finally, neuro-fuzzy depth estimator results are compared with NN depth estimator results obtained in chapter five.

Chapter seven concludes the thesis and proposes future research works in this field.

1.7 References

- [1] X. Maldague, "Advances in Signal Processing for Nondestructive Evaluation of Materials," NATO ASI Series, Vol. 262, 1994.
- [2] X. Maldague, Y. Largouët, J. P. Couturier, "A study of defect depth using neural networks in pulsed phase thermography: modeling, noise, experiments," *Rev. Gén. Therm.* 37, 704-717 Elsevier, paris, 1998.
- [3] S. Vallerand, A. Darabi, X. Maldague, "Defect Detection in Pulsed Thermography: A Comparison of Kohonen and Perceptron Neural Networks," *SPIE: Thermosense XXI*, R. N. Wurzbach, D. D. Burleigh eds., 3700: 20-25, Orlando, Fl, April 1999.
- [4] Y. Largouët, A. Darabi, X. Maldague, "Depth Evaluation in Pulsed Phase Thermography with Neural Network," *Review of Progress in Quantitative NDE*, D. O. Thompson et D. E. Chimenti eds, Plenum 18A: 611-617, 1998.
- [5] G. Manduchi, S. Marintti, P. Bison and E. Grinzato, "Application of neural Network Computing to Thermal Non-destructive Evaluation," *Neural Computing & Application* 6:148-157 Springer-Verlag London Limited 1997.
- [6] M. B. Saintey and D. P. Almond, "An Artificial Neural Network Interpretation for Transient Thermography Image Data," *NDT & E International*, Vol. 30. No. 5 pp. 291 -295, 1997.
- [7] R. J. Ball, D. P. Almond, "The Detection and Measurement of Impact Damage in Thick Carbon Fibre Reinforced Laminates by Transient Thermography," *NDT & E International*, Vol. 31. No. 3 pp. 165 -173, 1998.
- [8] D. R. Prabhu and W. P. Winfree, "Neural Network Based Processing of Thermal NDE Data for Corrosion Detection," *Review of Progress in Quantitative Nondestructive Evaluation*, vol. 12, 1993.

- [9] H. Trétout, D. David, J. Y. Marin and M. Dessendre, "An Evaluation of Artificial Neural Networks Applied to Infrared Thermography Inspection of Composite Aerospace Structures," *Review of Progress in Quantitative Nondestructive Evaluation*, Vol. 14, pp. 827-834, D. O. Thompson and D. E. Chimenti, Plenum Press, New York, 1995.
- [10] X. Maldague, "Nondestructive Evaluation of Materials by Infrared Thermography," Springer-Verlag London Limited, 1993.
- [11] R. A. Buchanan, P. Condon and L. Klynn, "Recent Advances in Digital Thermography for Nondestructive Evaluation," *SPIE: Thermosense XII*, S. A. Semanovich, March 1990.
- [12] T. Sakagami, K. Ogura and S. Kubo, "Damage Inspection of CFRP Using Resistive Heating Thermographic NDT," *SPIE: Thermosense XVIII*, D. D. Burleigh, J. W. Spicer eds., pp. 178-184, March 1996.
- [13] S. Setayeshi, "Underwater Signal Modeling for Subsurface Classification Using Computation Intelligence," Ph. D. Thesis, Technical University of Nova Scotia, Halifax, Nova Scotia, 1995.
- [14] T. P. Philippidis, V. N. Nikolaidis, A. A. Anastassopoulos, "Damage Characterization of Carbon/Carbon Laminates Using Neural Network Techniques on AE Signals," *NDT & E International*, Vol. 31. No. 5 pp. 329-340, 1998.
- [15] D. M. Tsai, "Boundary-Based Corner Detection Using Neural Networks," *Pattern Recognition*, Vol. 30, No. 1, pp. 85-97, 1997.
- [16] M. R. Azimi-Sadjadi and S. A. Stricker, "Detection and classification of Buried Dielectric Anomalies Using Neural Networks-Further Results", *IEEE Transaction on Instrumentation and Measurement*, Vol. 4. 3, No. 1, pp. 34-39, February 1994.

- [17] X. Miao, M. R. Azimi-Sadjadi and B. Tian, "Detection of Mine and Minelike Targets Using Principal Component and Neural-Network Methods", *IEEE Transaction on Neural Networks* Vol. 9, No. 3, pp. 454-463, May 1998
- [18] D. Wu, A. Salemo, J. Sembach, X. Maldague, J. Rantala, G. Busse, "Lock in Thermographic Inspection of Wood Particle Boards," *SPIE: Thermosense XIX*, R. N> Wurzbach, D. D. Burleigh, April 1997.
- [19] X. Maldague, "Évaluation Non Destructive par thermographie infrarouge," *IEEE Canadian Review*, no. 8, pp. 11-15, June 1990.
- [20] R. Osiander, J. W. M. Spicer and J. C. Murphy, "Thermal Imaging of Subsurface Microwave Absorber in Dielectric Materials," *SPIE* Vol. 2245, *Thermosense XVI*, 1994
- [21] S. Haykin, "Neural Networks: A Comprehensive Foundation" Mcmillan College Publishing Company, Inc. 1994.
- [22] A. K. Jain, J. Mao, and K. M. Mohiuddin, "Artificial Neural Networks: A Tutorial" *IEEE Transactions on Computer*, March 1996.
- [23] J. C. Krapez and P. Cielo, "Thermographic NonDestructive Evaluation: Data Inversion Procedures, Part I: 1-D Analysis and experimental results, *Res. Nondestruct Eval* 3(2): 81-100, 1991.
- [24] . C. Krapez, X. Maldague, P. Cielo, "Thermographic NonDestructive Evaluation: Data Inversion Procedures, Part II: 2-D Analysis and experimental results, *Res. Nondestruct Eval* 3: 101-124, 1991.
- [25] P. G. Bison, C. Bressan, R. Disarno, E. Grinzato, S. Marinetti and G. Manduchi, "Thermal NDE of delamination in plastic materials by neural network processing", *QIRT 94-Eurotherm Series 42, Édition Européennes Thermique et Industrie*, pp. 214-219, Paris 1995

- [26] A. Darabi "Massively Parallel Modeling of the Direct Problem in Infrared Thermography Applied to the Nondestructive Evaluation of Material"
Master thesis, Université Laval, October 1995.

CHAPTER 2

A Review of Transient Heat Transfer Modeling Applied to Infrared Thermography

2.1 Introduction

Thermographic nondestructive evaluation (TNDE) is attractive because of its non-contact nature, parallel imaging capabilities and rapid visualization of shallow subsurface defects, in particular within bonded structures [1] [2].

Generally, if the stimulating heat flux or surface temperature histories at the surface of an inspected component with known subsurface properties are known, then the temperature distribution can be found. This is termed the direct problem. In transient thermography, an heat flux is applied to the surface of the inspected material and then, subsequent surface temperature profiles are recorded by an infrared camera [3]. Subsurface defects cause perturbation of the heat flow. The reconstruction of subsurface defect

geometries from recorded surface temperature profiles is called the inverse problem in TNDE and it suffers from widely known difficulties such as ambiguity and instability due to noise [4]. The solutions of the direct problem, whereby the surface temperature distribution is computed for known defect geometries and thermal stimulation, provide useful information to interpret the experimental data, optimize the heat perturbation and scanning configuration, and determine the limits of applicability of the thermographic approach. Moreover in this study, it provides the desired training sets to neural networks.

2.2 Fundamentals of Heat Transfer

2.2.1 Conduction heat transfer

When a temperature gradient exists in a body, experience shows there is an energy transfer from the high-temperature region to the low-temperature region. This energy is transferred by conduction. The French mathematical physicist Joseph Fourier (1768-1830) gave the relationship between heat flow and temperature gradient for the first time in his analytic theory of heat. The Fourier law of conduction can be expressed for a homogeneous and isotropic solid as:

$$q(\mathbf{r}, t) = -k\nabla T(\mathbf{r}, t) \quad [W/m^2]. \quad (2.1)$$

where $q(\mathbf{r}, t)$ is the heat flux vector in the direction of the decreasing temperature, k is thermal conductivity of the material and $\nabla T(\mathbf{r}, t)$ is the time-dependent temperature gradient which is a normal vector to the isothermal surface. Here, \mathbf{r} is a spatial vector and t is the time variable. The units of the heat flux are W/m^2 , the units of the thermal conductivity are $W/(m \cdot ^\circ C)$ and those of the temperature gradient are $^\circ C/m$.

For a medium with constant thermal conductivity k (i.e., independent of position and temperature), as well as constant specific heat C_p , density ρ and no heat generation, the heat conduction equation can be formulated from Eq. (2.1) as:

$$\nabla^2 T(\mathbf{r}, t) = \frac{1}{\alpha} \frac{\partial T(\mathbf{r}, t)}{\partial t} \quad (2.2)$$

where:

$$\alpha = \frac{k}{\rho C_p} \quad (2.3)$$

is the thermal diffusivity of the medium with units in m^2/s . The Eq. (2.2) is called the diffusion or Fourier equation [5]. It follows that the heat conduction equation for an isotropic body in absence of volumic power density and expressed in a rectangular coordinate system (x, y, z) is [6]:

$$\frac{\partial}{\partial x} \left(k_x \frac{\partial T}{\partial x} \right) + \frac{\partial}{\partial y} \left(k_y \frac{\partial T}{\partial y} \right) + \frac{\partial}{\partial z} \left(k_z \frac{\partial T}{\partial z} \right) = \rho c_p \frac{\partial T}{\partial t}. \quad (2.4)$$

The differential Eq. (2.3) has numerous solutions. To obtain a solution, the differential equation of heat conduction requires to specify both boundary conditions and initial conditions (for time-dependent problem). The initial condition sets the temperature distribution at the initial time $(t = 0)$ and the boundary conditions of the medium set the temperature or the heat flow at the boundaries of the region (e.g. a known temperature, an insulated boundary or heat dissipation by convection or radiation from the boundary surface).

2.2.2 Convection Heat Transfer

The convection heat transfer mechanism occurs in fluids or gas. The heat transfer is due to the net movement of macroscopic volumes of fluid or gas along a solid wall while temperature of both the fluid or gas and the solid surface are different. To express the overall effect of convection, the Newton's law of cooling is used [7]:

$$q_{conv} = h(T_s - T_\infty) \quad [W/m^2] \quad (2.5)$$

Where q_{conv} is the heat flux (loss) from the solid surface at temperature T_s , T_∞ is the temperature of the fluid at a distance far from the boundary, and $h(Wm^{-2} \circ C^{-1})$ is the convection coefficient.

Although h can be calculated analytically for laminar flow over bodies having simple geometries, an experimental approach is the only practical approach to determine it for flow over bodies having complex configuration. It is generally available in tabular form.

2.2.3 Radiation Heat Transfer

All substances above the absolute temperature (0 K) continuously emit electromagnetic energy due to the molecular and atomic agitations associated with internal energy of the material. From the viewpoint of electromagnetic theory or alternatively from a quantum point of view, the waves or photons travel at the speed of light. The types of electromagnetic radiation can be classified according to their wavelength in vacuum. A portion of the electromagnetic radiation spectrum is shown in Figure 2.1. Thermal radiation lies in the range from about 0.1 to $100\ \mu\text{m}$. Practically, infrared NDE applications discussed here lie in the $3\text{-}5\ \mu\text{m}$ and $8\text{-}12\ \mu\text{m}$ corresponding to the two “transparent windows” of the atmosphere [8].

Radiation, which is the other mode of heat exchange, occurs at the surface of a solid, it is the electromagnetic radiation emitted in all directions. This quantity q_{rad} is given by the Stefan-Boltzmann law:

$$q_{rad} = \epsilon\sigma(T_{\infty}^4 - T_s^4) \quad [W/m^2] \quad (2.6)$$

where $\sigma = 5.6697 \times 10^{-8}\text{ W}/(\text{m}^2 \cdot \text{K}^4)$ is the Stefan-Boltzmann constant and ϵ is the surface emissivity of the solid: “ ϵ expresses the ability of a given surface to absorb or release energy, it varies from 0 for a perfect reflector (such as mirror) to 1 for a perfect emitter/absorber (such as a black body)”. Here, both T_{∞} and T_s are respectively absolute temperature of ambient and of solid surface [9].

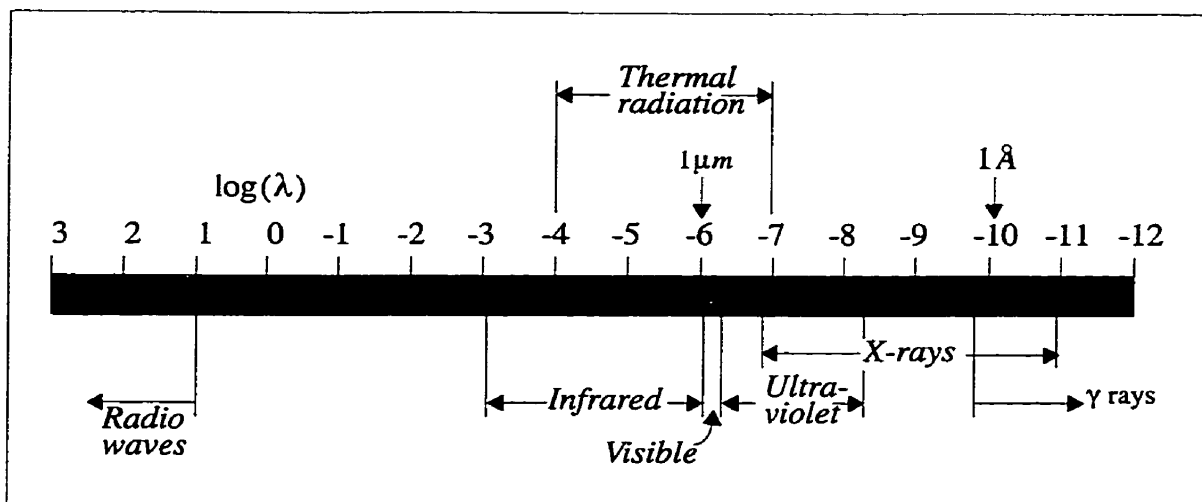


Figure 2.1 Electromagnetic radiation spectrum (wavelength λ in $\log_{10} m$).

2.3 Finite Difference Modeling

Obtaining an analytical solution from Eq. (2.4) is extremely difficult, except for certain simple geometries. Numerical computation techniques, based on discretization of space and time, such as the finite difference method and finite element method are often preferred for most practical problems.

A common technique for solving boundary-value heat conduction problems is the finite-difference method in which the initial statement of the problem in differential form is changed to a finite difference statement by substituting difference relations for partial temperature derivatives of the time and space. The accuracy of a lattice function, i.e. numerical solution obtained at the lattice points, depends on the parameters of the finite difference lattice (mainly its steps) and on the thermal characteristics of the material of interest. Therefore, when large temperature gradients arise in a body under the effect of high thermal effects and when there is difference between the geometry and thermal properties of contacting bodies, it is required to use a close-spaced nonuniform computational lattice which necessitates the use of great computational resources (large size of working memory and processor time).

2.3.1 Mathematical Approach

Let us restrict our attention to a three-dimensional planar problem and divide the body of interest into increments of equal size (called elements) as shown in Figure 2.2. Each element has its own thermal properties and an element boundary can also correspond to a material interface. The finite difference procedure is also called lumped capacitance because all of the control volume thermal capacitance is lumped at the central node point for all interior control volumes. The control volume boundaries are chosen to lie at the mid-plane of each element. This selection of control volume boundaries is somewhat arbitrary. The choice for control volume boundaries permits different materials to be present within a single control volume [7].

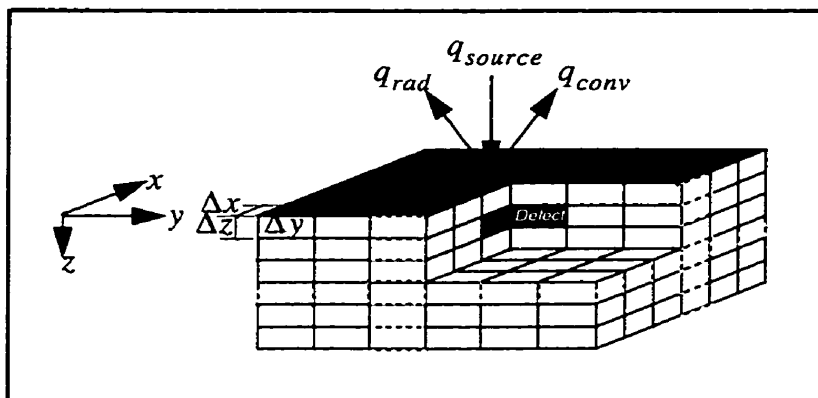


Figure 2.2 Three-dimensional model for planar geometry showing elementary volume.

Assuming that the time of observation is small with respect to the heat front propagation, all surfaces can be supposed to be thermally well isolated, except the external face of the sample on which heat exchanges occur (nodes located at $(x, y, z = 0)$). In active pulsed thermography, the surface heat exchanges consist generally into convective losses, radiative losses and perturbation from the heating source for a short time.

To easily solve the direct problem in TNDE, we can consider that the initial temperature at all of the nodes is equal to the environment temperature which is (T_∞) .

2.3.2 Nodes on the Surface

First, the general energy conservation is applied to the elementary volume of the nodes on the surface subjected to heat exchange by convection and radiation with an environment at temperature T_∞ . Figure 2.3 provides an expanded view of these elementary volumes. Assuming that the volumetric parameters ρ , C_p , k_x , k_y , and k_z are constant for each element, we make a transient energy balance on the node $(k, m, 0)$ by setting the energy conducted, convected and radiated into the node equal to the increase in the internal energy of the node. The result is:

$$\begin{aligned}
 & k_x \Delta y \frac{\Delta z}{2} \left(\frac{T_{(k+1, m, 0)}^p - T_{(k, m, 0)}^p}{\Delta x} + \frac{T_{(k-1, m, 0)}^p - T_{(k, m, 0)}^p}{\Delta x} \right) \\
 & + k_y \Delta x \frac{\Delta z}{2} \left(\frac{T_{(k, m+1, 0)}^p - T_{(k, m, 0)}^p}{\Delta y} + \frac{T_{(k, m-1, 0)}^p - T_{(k, m, 0)}^p}{\Delta y} \right) \\
 & + k_z \Delta y \Delta x \left(\frac{T_{(k, m, 1)}^p - T_{(k, m, 0)}^p}{\Delta z} \right) + h_c \Delta y \Delta x (T_\infty - T_{(k, m, 0)}^p) \\
 & + h_r \Delta y \Delta x ((T_\infty + 273)^4 - (T_{(k, m, 0)}^p + 273)^4) + q_{source} \\
 & = \rho c_p \Delta x \Delta y \frac{\Delta z}{2} \frac{(T_{(k, m, 0)}^{p+1} - T_{(k, m, 0)}^p)}{\Delta t}
 \end{aligned} \tag{2.7}$$

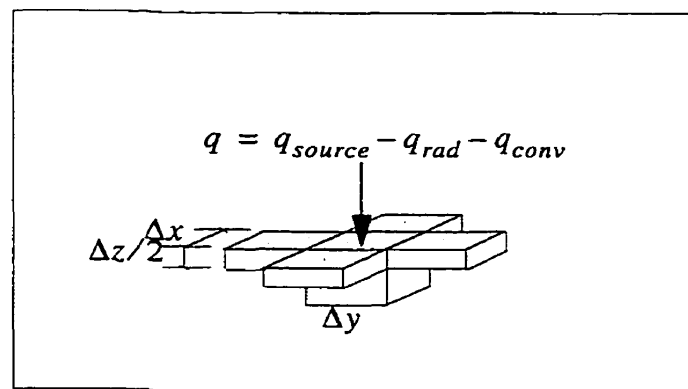


Figure 2.3 Expanded view of control volume surrounding arbitrary surface node $(k, m, 0)$

Where, h_{conv} and h_{rad} are respectively the convection heat-transfer coefficient and the radiation heat-transfer coefficient. In this relation the superscripts designate the time incre-

ment and superscripts p and $p+1$ are respectively present and next iteration times. The Eq. 2.7 for $T_{(k,m,0)}^{p+1}$ (next surface temperature on the position (k, m)) becomes:

$$\begin{aligned}
T_{(k,m,0)}^{p+1} = & \frac{k_x}{\rho c_p (\Delta x)^2} (T_{(k+1,m,0)}^p + T_{(k-1,m,0)}^p - 2T_{(k,m,0)}^p) \\
& + \frac{k_y}{\rho c_p (\Delta y)^2} (T_{(k,m+1,0)}^p + T_{(k,m-1,0)}^p - 2T_{(k,m,0)}^p) \\
& + 2 \frac{k_y}{\rho c_p (\Delta z)^2} (T_{(k,m,1)}^p - T_{(k,m,0)}^p) + 2 \frac{h_c}{\rho c_p \Delta z} (T_\infty - T_{(k,m,0)}^p) \\
& + 2 \frac{h_r}{\rho c_p \Delta z} ((T_\infty)^4 - (T_{(k,m,0)}^p)^4) + T_{(k,m,0)}^p + \frac{2\Delta t}{\rho c_p (\Delta x \Delta y \Delta z)} (q_{source}) .
\end{aligned} \tag{2.8}$$

2.3.3 Nodes Inside the Sample

For an arbitrary interior node (k, m, n) , Figure 2-4, the differential equation which governs the heat flow is:

$$k_x \frac{\partial^2 T}{\partial x^2} + k_y \frac{\partial^2 T}{\partial y^2} + k_z \frac{\partial^2 T}{\partial z^2} = \frac{1}{\rho c_p} \frac{\partial T}{\partial t} . \tag{2.9}$$

We can now approximate the second partial derivatives with:

$$\frac{\partial^2 T}{\partial x^2} \approx \frac{1}{(\Delta x)^2} (T_{(k+1,m,n)} + T_{(k-1,m,n)} - 2T_{(k,m,n)}) \tag{2.10}$$

$$\frac{\partial^2 T}{\partial y^2} \approx \frac{1}{(\Delta y)^2} (T_{(k,m+1,n)} + T_{(k,m-1,n)} - 2T_{(k,m,n)}) \tag{2.11}$$

$$\frac{\partial^2 T}{\partial z^2} \approx \frac{1}{(\Delta z)^2} (T_{(k,m,n+1)} + T_{(k,m,n-1)} - 2T_{(k,m,n)}) \tag{2.12}$$

and the time derivative in Eq. (2.9) by:

$$\frac{\partial T}{\partial t} \approx \frac{T_{m,n}^{p+1} - T_{m,n}^p}{\Delta t} . \tag{2.13}$$

Substituting Eq. (2.10), (2.11), (2.12) and (2.13) in the Eq. (2.9) yields to:

$$\begin{aligned}
 T_{(k,m,n)}^{p+1} = & \frac{k_x}{\rho c_p (\Delta x)^2} (T_{(k+1,m,n)}^p + T_{(k-1,m,n)}^p - 2T_{(k,m,n)}^p) \\
 & + \frac{k_y}{\rho c_p (\Delta y)^2} (T_{(k,m+1,n)}^p + T_{(k,m-1,n)}^p - 2T_{(k,m,n)}^p) \\
 & + \frac{k_z}{\rho c_p (\Delta z)^2} (T_{(k,m,n+1)}^p + T_{(k,m,n-1)}^p - 2T_{(k,m,n)}^p) \\
 & + T_{(k,m,n)}
 \end{aligned} \tag{2.14}$$

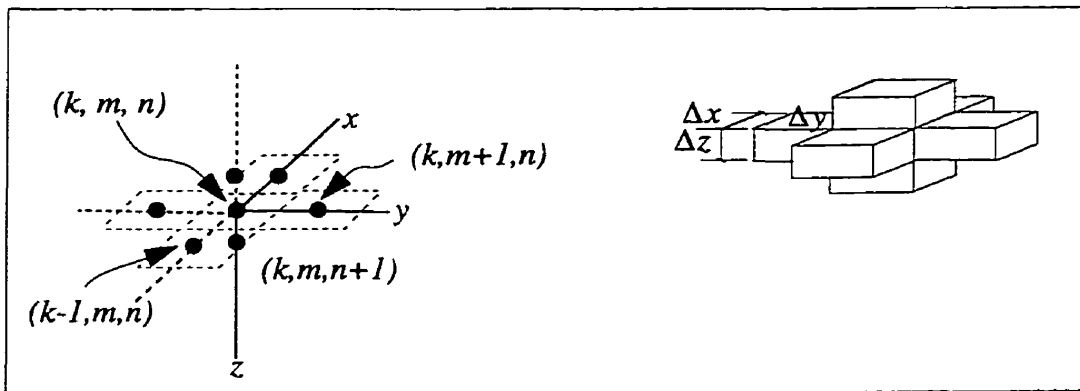


Figure 2.4 Expanded view of control volume surrounding arbitrary interior node (k, m, n) .

2.3.4 Nodes on an Adiabatic(insulated) Boundary

Consider a node (k, m, n) on an adiabatic (or insulated) boundary surface which is parallel to the X-Z plane, as shown in Figure 2.5. Let $T_{(k,m,n)}$ be the temperature at the node (k, m, n) and $T_{(k-1,m,n)}$, $T_{(k+1,m,n)}$ and $T_{(k,m,n-1)}$, $T_{(k,m,n+1)}$ and $T_{(k,m-1,n)}$ be the temperature at the five neighboring nodes, as illustrated in Figure 2-5. The adiabatic boundary for which $\partial T/\partial y = 0$ is equivalent to a symmetry condition for this boundary. Then, we consider the existence of a mirror-image point $(k, m+1, n)$ of the node $(k, m-1, n)$ with respect to this boundary. If the temperature at this image node is $T_{(k,m+1,n)}$, then by symmetry we have $T_{(k,m+1,n)} = T_{(k,m-1,n)}$. When the region and its mirror image with respect to the boundary are considered as a single region, the node (k, m, n) becomes an

interior point and finite-difference Eq. (2.14) is applicable with $T_{(k, m+1, n)} = T_{(k, m-1, n)}$. Then, the finite-difference equation for the node (k, m, n) on an adiabatic boundary surface parallel to the X-Z plane, as shown in Fig. 2.5 becomes:

$$\begin{aligned}
 T_{(k, m, n)}^{p+1} = & \frac{k_x}{\rho c_p (\Delta x)^2} (T_{(k+1, m, n)}^p + T_{(k-1, m, n)}^p - 2T_{(k, m, n)}^p) \\
 & + \frac{k_y}{\rho c_p (\Delta y)^2} (2T_{(k, m-1, n)}^p - 2T_{(k, m, n)}^p) \\
 & + \frac{k_y}{\rho c_p (\Delta z)^2} (T_{(k, m, n+1)}^p + T_{(k, m, n-1)}^p - 2T_{(k, m, n)}^p) \\
 & + T_{(k, m, n)}
 \end{aligned} \tag{2.15}$$

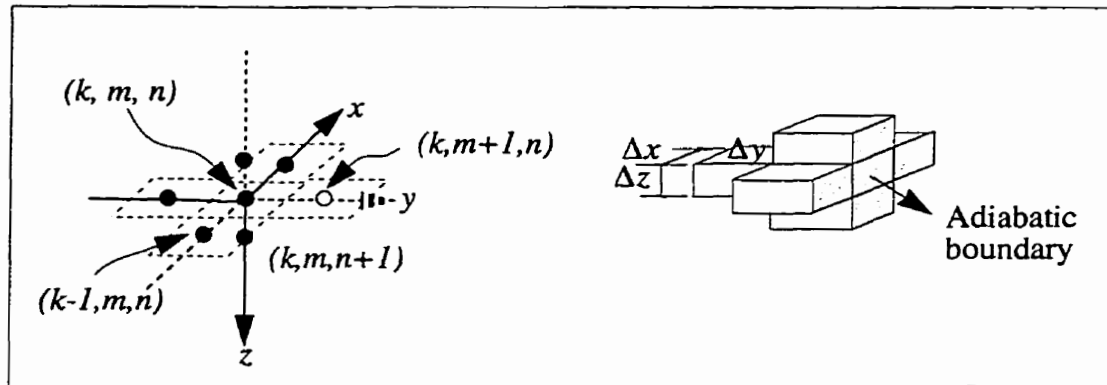


Figure 2.5 Expanded view of control volume surrounding arbitrary adiabatic boundary node (k, m, n) .

2.3.5 Stability Criteria

As it was mentioned, in finite-difference method each volume element behaves as a small “lumped capacity” and the interaction of all elements determines the behavior of the solid during a transient process. We can also express the energy balance on node i (Fig 2.6) by using the concept of thermal resistance and capacity in analogy with the electric resistance and capacity as:

$$q_i + \sum_j \frac{T_j^p - T_i^p}{R_{ij}} = C_i \frac{(T_i^{p+1} - T_i^p)}{\Delta t} \tag{2.16}$$

where

$$R_{ij} = \frac{\delta_{ij}}{k_{ij}A_{kij}} \text{ for conduction,} \quad (2.17)$$

$$R_{ij} = \frac{\delta_{ij}}{k_{ij}A_{cij}} \text{ for convection,} \quad (2.18)$$

$$C_i = V_i \rho c_p. \quad (2.19)$$

The term q_i is the heat generated in or added to the volume lump at i and j denotes all neighboring nodes connected to node i . In Eq.(2.18), R_{ij} is the total thermal resistance and δ_{ij} is the conduction distance between nodes i and j , k_{ij} is the heat conductivity along δ_{ij} and A_{kij} is the cross-sectional area for heat conduction normal to δ_{ij} . Also, A_{cij} is the cross-sectional area for heat convection normal to δ_{ij} , and the terms C_i and V_i respectively denote thermal capacity and volume element at the node i .

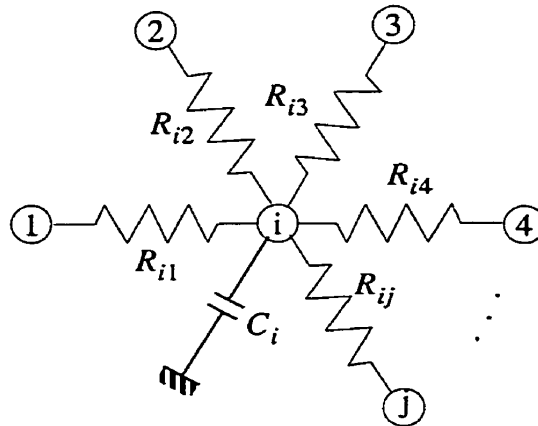


Figure 2.6 General conduction node.

The Eq. (2.19) for $T_{(k,m,0)}^{p+1}$ becomes:

$$T_i^{p+1} = \left(q_i + \sum_j \frac{T_j^p}{R_{ij}} \right) \frac{\Delta t}{C_i} + \left(1 - \frac{\Delta t}{C_i} \sum_j \frac{1}{R_{ij}} \right) T_i^p. \quad (2.20)$$

Considering Eq. (2.20), we again have the convenience of solving for the temperature at time $(p+1)$ and this requires only information at time (p) . However, we also have a problem of stability. The value of q_i influences the stability, we can thus choose a safe limit by observing the behavior of the equation for $q_i=0$, then we can say Eq. (2.20) is stable only if:

$$1 - \frac{\Delta t}{C_i} \sum \frac{1}{R_{ij}} \geq 0. \quad (2.21)$$

After solving Eq. (2.20) for different nodes and boundary conditions, we have the task of choosing the time increment Δt required for the calculations. To ensure stability we must keep Δt equal to or less than a value obtained from the most severe nodal relation given in Eq. (2.21) [7]. In this case we have:

$$\Delta t \leq \left(\frac{C_i}{\sum \frac{1}{R_{ij}}} \right)_{min}. \quad (2.22)$$

For example, for an interior node such as shown in Fig 2.4 in an isotropic medium ($k_x=k_y=k_z=k$), if we choose $\Delta x=\Delta y=\Delta z=\delta$, then the stability relation is given by:

$$\Delta t \leq \frac{\Delta x \Delta y \Delta z \rho c_p}{2 \left(\frac{k \Delta y \Delta z}{\Delta x} \right) + 2 \left(\frac{k \Delta x \Delta z}{\Delta y} \right) + 2 \left(\frac{k \Delta x \Delta y}{\Delta z} \right)} = \frac{\delta^2}{6\alpha} \quad (2.23)$$

or

$$\Delta t \leq \frac{\delta^2}{6\alpha}. \quad (2.24)$$

2.4 Analytical Solution of the Heat Conduction Problem in Active IR Thermography

In previous sections, we have considered the solution of three-dimensional non-homogeneous heat-conduction with time-independent boundary conditions. However, in active infrared thermography, one of the boundary condition functions, for example at boundary surface S_j , is time dependent so that the related heat transfer equation and its boundary conditions can be expressed in the form [5]:

$$\nabla^2 T(\mathbf{r}, t) = \frac{1}{\alpha} \frac{\partial T(\mathbf{r}, t)}{\partial t} \text{ in the sample, } t > 0 \quad (2.25)$$

$$k_i \frac{\partial T}{\partial n_i} + h_i T = \delta_{1i} f_i(t) \text{ on boundary } S_i \quad (2.26)$$

$$i = 1, 2, \dots, N, t > 0$$

$$T(\mathbf{r}, t) = 0 \text{ for } t = 0, \text{ in the sample} \quad (2.27)$$

where $\frac{\partial T}{\partial n_i}$ is the temperature derivation in the direction normal to the boundary surface S_i and δ_{1i} is defined as:

$$\delta_{1i} \begin{cases} 0 & i \neq 1 \\ 1 & i = 1. \end{cases} \quad (2.28)$$

To solve this problem, we define an auxiliary problem as:

$$\nabla^2 \Phi(\mathbf{r}, t) = \frac{1}{\alpha} \frac{\partial \Phi(\mathbf{r}, t)}{\partial t} \text{ in the sample, } t > 0 \quad (2.29)$$

$$k_i \frac{\partial \Phi}{\partial n_i} + h_i \Phi = \delta_{1i} \text{ on boundary } S_i \quad (2.30)$$

$$i = 1, 2, \dots, N, t > 0$$

$$\Phi(\mathbf{r}, t) = 0 \text{ for } t = 0, \text{ in the sample} \quad (2.31)$$

in which the boundary conditions, Eq. (2.30) do not depend on time. It can then be solved

with the convenience of heat transfer techniques. Next, we can relate the solution of $T(\mathbf{r}, t)$ to the problem expressed by Eq. (2.25)-(2.27) to the solution of the auxiliary problem $\Phi(\mathbf{r}, t)$ using Duhamel's theorem as [5]:

$$T(\mathbf{r}, t) = \int_{\tau=0}^t f(\tau) \frac{\partial \Phi(\mathbf{r}, t-\tau)}{\partial t} d\tau. \quad (2.32)$$

Now, suppose the boundary condition function $f_I(t)$, on surface S_I , has discontinuities due to heat source or changes in the ambient temperature as shown in Figure 2.7. The solution given in Eq. (2.33) for this specific step shape boundary condition in the time interval $(N-1)\Delta t < t < N\Delta t$ becomes:

$$T(\mathbf{r}, t) = \sum_{j=0}^{N-1} \Phi(\mathbf{r}, t-j\Delta t) \Delta f_j \quad (2.33)$$

where:

$$\Delta f_j = f^+(\tau_j) - f^-(\tau_j) \quad (2.34)$$

is the step change of $f_I(t)$ at the time $\tau_j = j\Delta t$ and Δt is time step [5].

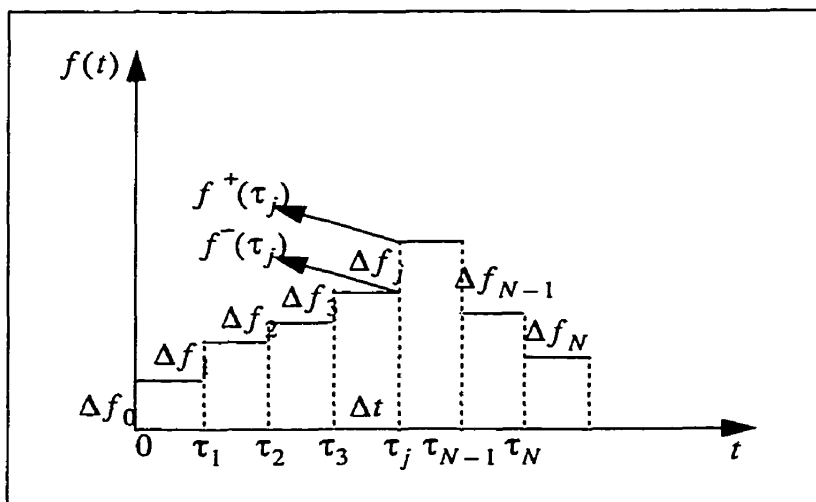


Figure 2.7 A step-shape function as the time dependent boundary condition

The following step is to consider the pulse-transient IR thermography, in which the sample is heated by a heat pulse source and then a time sequence of images is recorded to

process the temperature decay on the surface of inspected sample [1]. In non-flaw areas far from defects, we can suppose that the sample behaves as an adiabatic plate heated by a square pulse [10]. This simple configuration is illustrated in Fig 2.8.

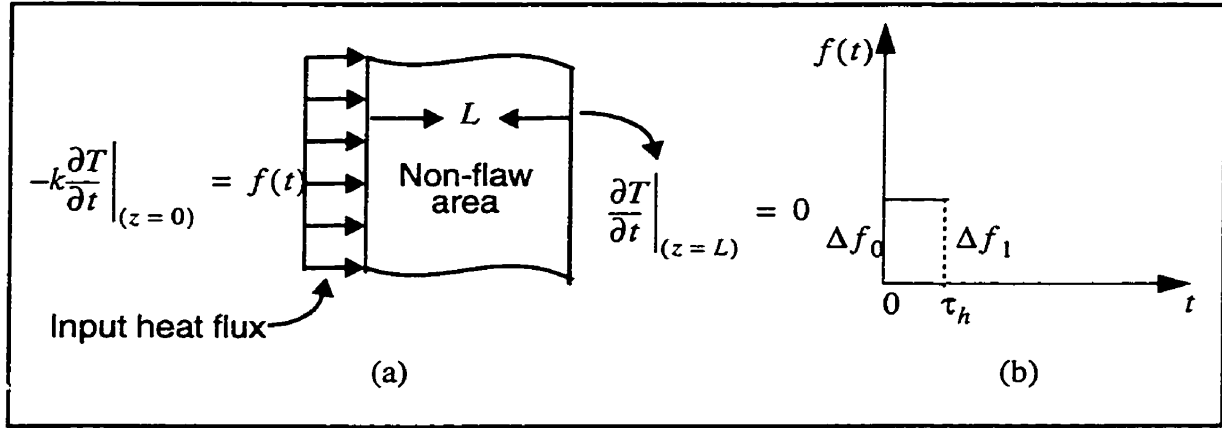


Figure 2.8 (a) Model heating (b) shape of the heat pulse.

The plate with thickness L is initially at zero temperature differential i.e. 0°C with respect to ambient temperature. For times $t > 0$ the boundary surface at $z = L$ is kept insulated while the surface at $z = 0$ is subjected to a heat pulse flux as:

$$-k \frac{\partial T}{\partial z} = f(t) = \begin{cases} Q & \text{for } 0 < t < \tau_h \\ 0 & \text{for } t > \tau_h \end{cases} \quad (2.35)$$

Mathematically, this heat conduction problem can be expressed by:

$$\frac{\partial^2 T(z, t)}{\partial z^2} = \frac{1}{\alpha} \frac{\partial T(z, t)}{\partial t} \text{ in } 0 < z < L, t > 0 \quad (2.36)$$

$$-k \frac{\partial T}{\partial z} = f(t) \text{ at } z = 0, t > 0 \quad (2.37)$$

$$-k \frac{\partial T}{\partial z} = 0 \text{ at } z = L, t > 0 \quad (2.38)$$

$$T(z, t) = 0 \text{ for } t = 0 \quad (2.39)$$

and corresponding auxiliary problem is given as:

$$\frac{\partial^2}{\partial z^2} \Phi(z, t) = \frac{1}{\alpha} \frac{\partial \Phi(z, t)}{\partial t} \quad \text{in } 0 < z < L, t > 0 \quad (2.40)$$

$$-k \frac{\partial \Phi}{\partial z} = f(t) \quad \text{at } z = 0, t > 0 \quad (2.41)$$

$$-k \frac{\partial \Phi}{\partial z} = 0 \quad \text{at } z = L, t > 0 \quad (2.42)$$

$$\Phi(z, t) = 0 \quad \text{for } t = 0. \quad (2.43)$$

The solution of this auxiliary problem is [5]:

$$\Phi(z, t) = \frac{\alpha}{Lk_z} t + \frac{2}{Lk_z} \sum_{m=1}^{\infty} \frac{\cos \beta_m z}{\beta_m^2} \left(1 - e^{(-\alpha \beta_m^2 t)} \right) \quad (2.44)$$

where $\beta_m = m\pi / L$. Now, if we apply Duhamel's theorem given by Eq. (2.34) with the considered boundary conditions on the surface, $f(t)$, the temperature at the surface sample is obtained with:

$$T(0, t) = \frac{QL}{k_z} \left(Fo + \frac{2}{\pi^2} \sum_{m=1}^{\infty} \frac{1}{m^2} (1 - e^{-m^2 \pi^2 Fo}) \right) \quad \text{for } 0 < t < \tau_h \quad (2.45)$$

$$T(0, t) = \frac{QL}{k_z} \left(Fo_h + \frac{2}{\pi^2} \sum_{m=1}^{\infty} \frac{1}{m^2} \left(e^{-m^2 \pi^2 (Fo - Fo_h)} - e^{-m^2 \pi^2 Fo} \right) \right) \quad \text{for } t > \tau_h \quad (2.46)$$

where $Fo = \alpha t / L^2$ is the Fourier number and $Fo_h = \alpha \tau_h / L^2$ is the Fourier number of time of maximum excess temperature. Figure 2.9 shows the temperature curve obtained from Eqs. (2.46) and (2.47) for a carbon fiber reinforced plastic (CFRP) sample with thickness $L = 2 \text{ mm}$, thermal properties $\alpha_z = 0.42 \times 10^{-6} \text{ m}^2 \text{ s}^{-1}$, $k_z = 0.8 \text{ W m}^{-1} \text{ }^\circ\text{C}^{-1}$ and a heat pulse with $Q = 100 \text{ kW m}^{-2}$ and $\tau_h = 0.5 \text{ s}$ as shown in Figure 2.8-b.

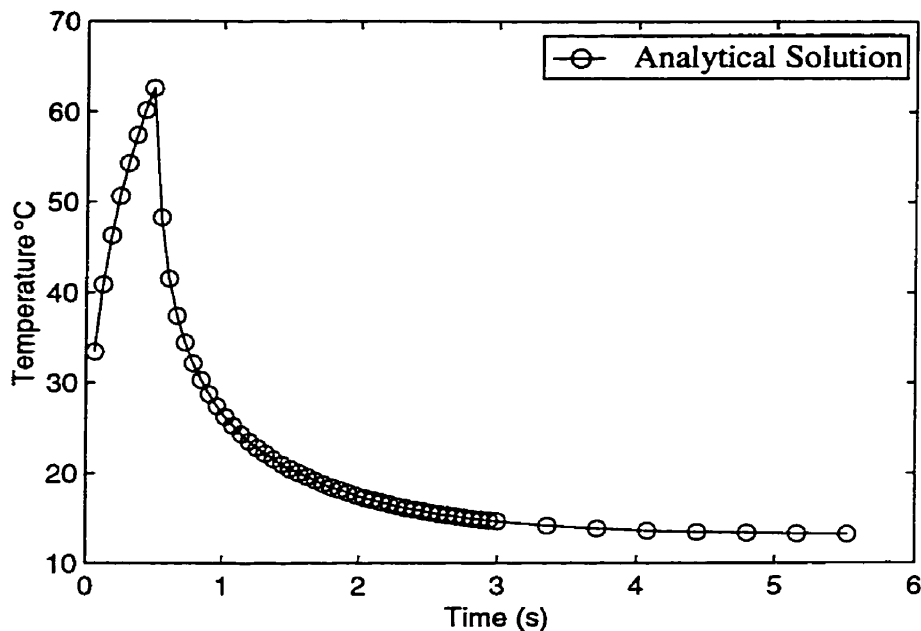


Figure 2.9 Temperature evolution curve on the heated surface of a CFRP sample (without defect), obtained from the analytical solution of the problem.

2.5 Delamination Model Description

Delamination defects are characterized by air gaps between two plies in composite laminate materials such as CFRP. These structural discontinuities produce an interface thermal resistance that causes heat flux perturbation during the transient thermographic procedure.

The specimen studied is shown schematically in Figure 2.10. It is a CFRP block which contains an air gap as simulated defect. It is assumed that the sample surface is uniformly heated by a heating source (such as flash lamps, laser or electrical heaters) for a time τ . Here, we specify a finite-size delaminated defect involved into the solution of 3-D heat conduction equation (Eq. (2-4)) with boundary and initial conditions as follow [6]:

$$0 \leq x \leq L_1; 0 \leq y \leq L_2; 0 \leq z \leq L_3 \quad (2.47)$$

$$T_{(x, y, z, \tau = 0)} = 0 \quad (2.48)$$

$$\frac{\partial T}{\partial z}(x, y, z=0) = -\frac{q}{k_z} + \frac{h_c}{k_z} T(x, y, z=0) + \frac{h_r}{k_z} ((T(x, y, z=0) + 273)^4 - 273^4) \quad (2.49)$$

$$\frac{\partial T}{\partial x}(x=0, y, z) = 0 \quad (2.50)$$

$$\frac{\partial T}{\partial y}(x, y=0, z) = 0 \quad (2.51)$$

$$\frac{\partial T}{\partial x}(x=L_1, y, z) = 0 \quad (2.52)$$

$$\frac{\partial T}{\partial y}(x, y=L_2, z) = 0 \quad (2.53)$$

$$\frac{\partial T}{\partial z}(x, y, z=L_3) = 0 \quad (2.54)$$

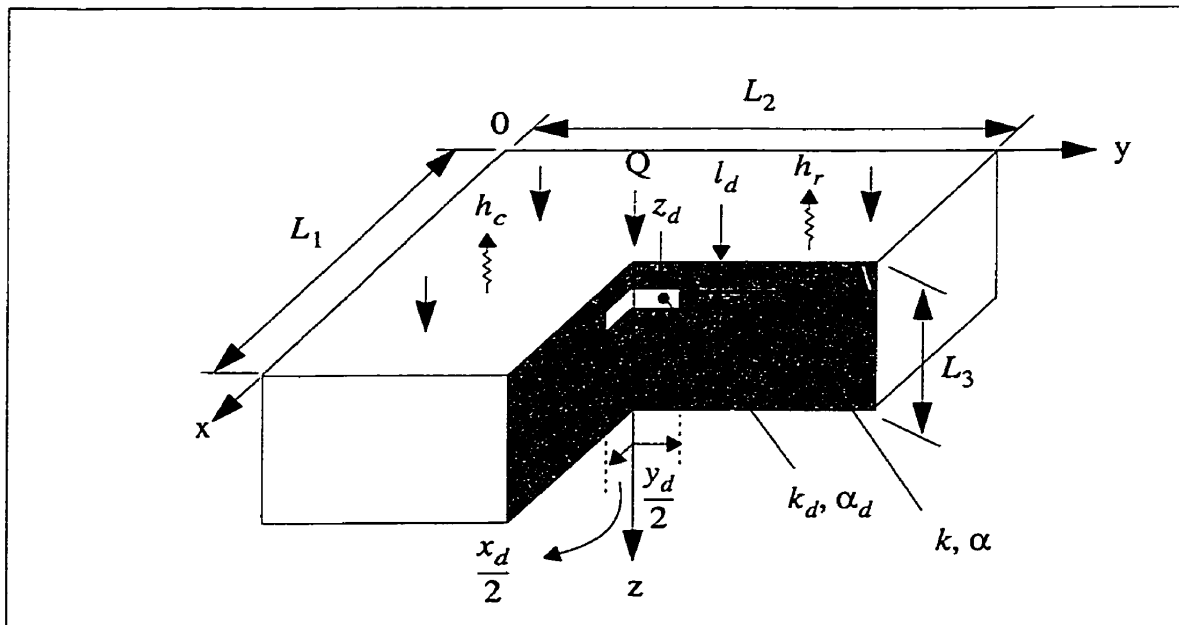


Figure 2.10 Schematic diagram of the modeled CFRP sample.

Here the initial ambient temperature is set to 0°C (273 K) for sake of simplicity, where L_1 ,

L_2 and L_3 are the CFRP block dimensions, Q is the input heat flux, h_c and h_r are respectively convection and radiation heat exchange coefficients.

In order to study the behavior of defect signals, we choose a sample which contains an air gap. The dimensions of the CFRP block are $L_1 = 96 \text{ mm}$, $L_2 = 96 \text{ mm}$ and $L_3 = 2 \text{ mm}$. The defect is a $1.5 \text{ cm} \times 1.5 \text{ cm}$ square with thickness of $100 \text{ }\mu\text{m}$ at depth $700 \text{ }\mu\text{m}$. The thermal properties and heating-cooling parameters are respectively as follow:

- thermal properties:

for CFRP

$$\alpha_x = \alpha_y = 3.7 \times 10^{-6} \text{ m}^2\text{s}^{-1}$$

$$\alpha_z = 0.42 \times 10^{-6} \text{ m}^2\text{s}^{-1}$$

$$k_x = k_y = 7 \text{ Wm}^{-1}\text{ }^\circ\text{C}^{-1} \text{ (parallel to the fibers)}$$

$$k_z = 0.8 \text{ Wm}^{-1}\text{ }^\circ\text{C}^{-1} \text{ (perpendicular to the fibers)}$$

for air defect

$$\alpha = 33 \times 10^{-6} \text{ m}^2\text{s}^{-1}$$

$$k = 0.024 \text{ Wm}^{-1}\text{ }^\circ\text{C}^{-1}$$

- heating-cooling parameters:

$$q = 10 \text{ kWm}^{-2}, h_c = 10 \text{ Wm}^{-2}, h_r = 5.67 \times 10^{-8} \text{ Wm}^{-2}$$

The computed temperature profiles over defect (*-dotted curve) and sound (x-dotted curve) areas on the sample surface are illustrated in Figure 2.11. As seen, the thermal perturbation due to defect is well distinguishable. In the next chapters, we will explain how it is possible to enhance the thermal contrast between these two curves and use it to reveal and estimate defects parameters. An example of such an enhancement is the defect-sound difference shown on Figure 2.11-b.

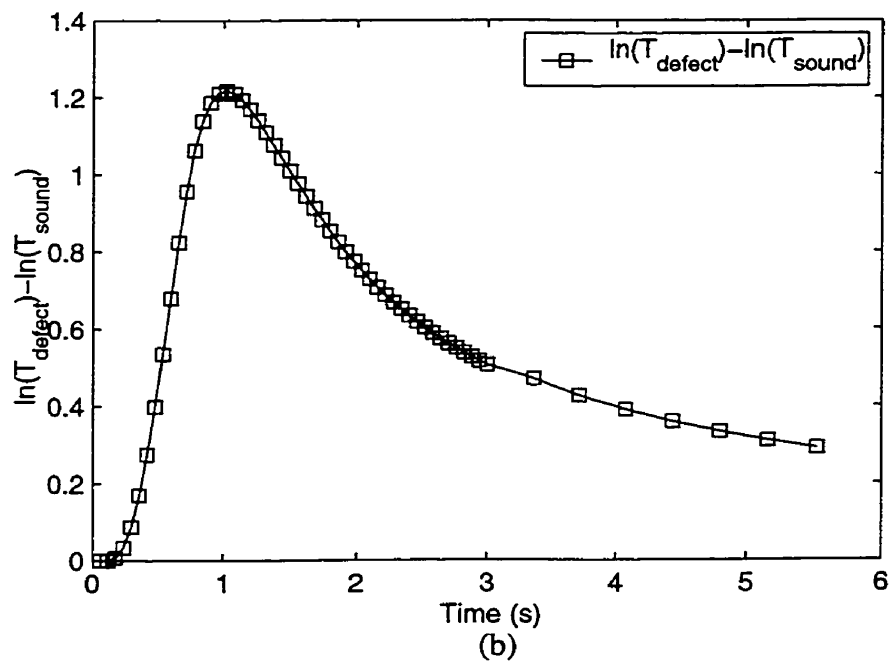
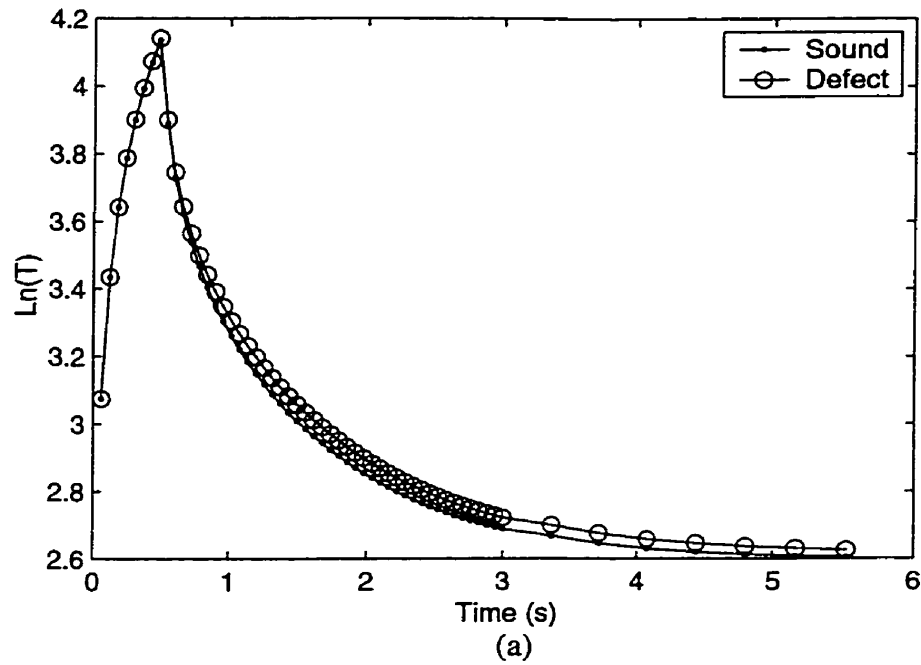


Figure 2.11 The computed temperature evolution over: (a) defect and sound areas (b) their difference on the CFRP sample surface

As mentioned previously, it is extremely difficult to find an analytical solution for this problem. To evaluate the performance of our 3-D simulation, we first suppose the

sample shown in Figure 2-10 contains no defects. In this case, the problem can be analyzed as 1-D heat conduction problem as discussed in previous sections. We can thus compare the computed temperature profile with the one obtained from the analytic solution of the problem described in section 2.5. In Figure 2.12, the “.”doted curve corresponds to our numerical solution and the “o” dotted curve corresponds to the analytic solution of the 1-D heat conduction problem. These two curves match well (maximum discrepancy is less than 1.6 °C after heating pulse), therefore our numerical solution is accurate enough to be used for TNDE applications.

Later in section 3.5, we will further assess the validity of our thermal modeling in presence of subsurface defects.

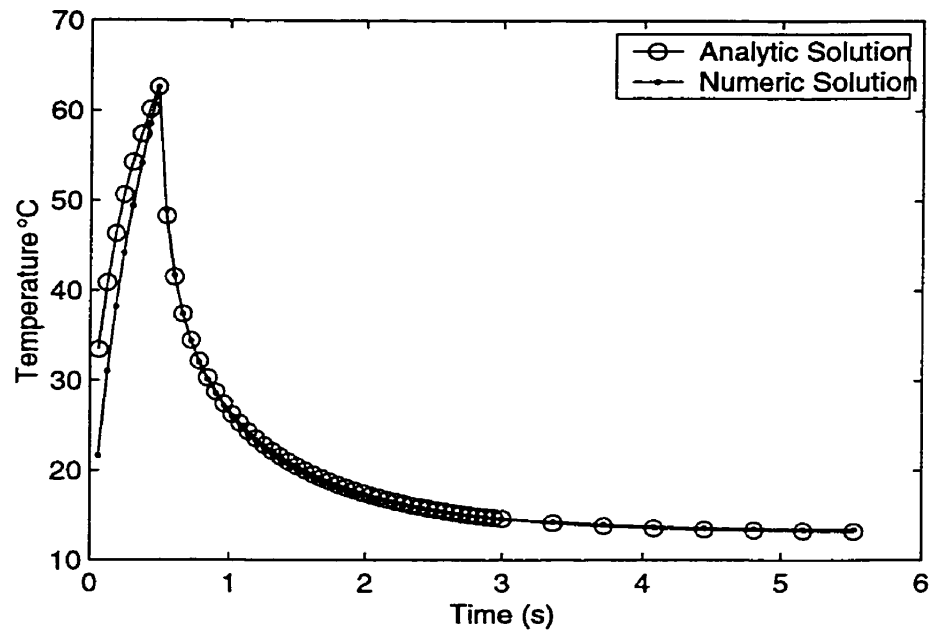


Figure 2.12 Surface temperature evolution of CFRP block computed using analytical and numerical solution methods.

2.6 Conclusion and Contribution

In this chapter, we first discussed the fundamentals of heat transfer such as conduction, convection and radiation heat transfer in section 2.2. The heat conduction equations for both homogeneous and non-homogeneous materials were given. Then, in

section 2.3, finite difference modeling of 3-D heat conduction was briefly overviewed and we gave all the required equations for different nodes and boundary conditions. The stability criteria for explicit finite difference modeling was also considered. The analytical solution of the 1-D heat conduction problem was described in section 2.5. The analytical solution for pulse-heated TNDE problem is obtained using Duhamel's theorem. Finally, the delamination model description is given in section 2.6. A numerical and analytical solutions of computed temperature curves for an CFRP sample was obtained. Results showed our numerical simulation is adequately accurate and applicable for active TNDE tasks.

The modeling presented in this chapter which provides a numerical simulation for understanding and modifying experimental setup parameters in active TNDE is a precious tool especially for NN training with various input data as we will see in next chapters.

2.7 References

- [1] X. Maldague, "Nondestructive Evaluation of Materials by Infrared Thermography", Springer-Verlag London Limited, 1993.
- [2] J. C. Krapez and P. Cielo, "Thermographic NonDestructive Evaluation: Data Inversion Procedures, Part I: 1-D Analysis and experimental results, Res. Nondestruct Eval 3(2): 81-100 1991.
- [3] W. P. Winfree and K. Elliott Cramer, "Computational pulse shaping for thermographic inspections" Proc. SPIE, Vol. 2766, 228-235, 1996.
- [4] U. Seidel, H. G. Walther, "Estimation of depth, width and magnitude of material inhomogeneity from photothermal measurements" Proc. SPIE, Vol. 2766, 240-248, 1996.
- [5] M. Necati Ozisik, "Heat Conduction" Second Edition, John Wiley & Sons Inc., 1993.
- [6] A. Darabi "Massively Parallel Modeling of the Direct Problem in Infrared Thermography Applied to the Nondestructive Evaluation of Material" Master thesis, Universite Laval, October 1995.
- [7] J. P. Holman, "Heat Transfer", 1981, McGraw Hill, Inc.
- [8] D. P. Dewitt Gend. D. Nutter, "Theory and Practice of Radiation Thermometry", 1988, John Wiley & Sons Inc.
- [9] R. Siegel & J. R. Howell, "Thermal Radiation Heat Transfer", 1972, McGraw Hill Inc.
- [10] V. Vavilov, X. Maldague, B. Dufort, F. Robitaille and J. Picard, "Thermal nondestructive testing of carbon epoxy composites: detailed analysis and data processing", NDT&E International Volume 26 number 2, 85-95, 1993.

CHAPTER 3

Massively Parallel Implementation of the Heat Transfer Problem in IR Thermography

3.1 Introduction

As mentioned in the last chapter, a common technique for solving boundary-values of heat conduction problems applied to TNDE is the finite-difference method in which one starts from the initial statement of the problem in differential form and translates it to a finite difference statement by substituting difference relations for partial temperature derivatives of the time and space variables. The accuracy of a lattice function, i.e. numerical solutions obtained at the lattice points, depends on the parameters of the finite-difference lattice (its steps) and on the thermal characteristics of the samples [1]. Therefore, when large temperature gradients arise in a body under the effect of high thermal effects and when there is a contrast between the geometry and thermal properties of contacting bodies, it is required to use close-spaced nonuniform computational lattice necessitating great computational resources. Problems with such computational constraints can be solved

successfully using a massively parallel algorithm ran on a parallel computer such as the MasPar (Massively Parallel Computer) available at Université Laval.

In this chapter, we first introduce SIMD (Single Instruction, Multiple Data) processing and the MasPar system. In section 3-4, we present implementation of direct problem in infrared thermography on the MasPar MP-1. Advantages of such massively parallel modeling are explained in section 3-5. Implementation of the direct problem on parallel architecture was studied during accomplishment of my master degree [2]. Since then however, I had to bring some modifications to simulate samples including with multiple defects and lateral interaction between defects. These kind of samples will be used in the next chapters to extract training and test sets for neural networks or fuzzy systems applied to characterize defects.

3.2 SIMD Processing

Several computational models have been proposed for the so-called massively parallel computation, in which thousands or more PEs (Processing Elements) run in parallel. The SIMD model seems one of the most promising models, although its application area is restricted as compared with other models. In fact, some commercial SIMD machines are now available and are being used for complex applications such as in meteorology.

In general, a SIMD machine consists of a huge number of PEs and a front-end processor which controls the execution of PEs. Each PE has its own local memory. By operating on data in the local memory, each PE runs concurrent stream but in synchronism with other PEs. PEs do not have their own instruction streams but they simply execute instructions supplied by the front-end. Except for this last point, each PE can be regarded as an ordinary uni-processor. The front-end includes a workstation that runs an implementation of a UNIX operating system with standard I/O.

3.3 MasPar Parallel Processor

The MasPar MP-1 is a SIMD with at least 1024 (1K) PEs, the machine available at Université Laval has 2048 PEs. This machine consists of two parts: the front-end UNIX workstation and the back-end called the data parallel unit (DPU). The back-end consists of an array control unit (ACU) which broadcasts instructions to PEs, and of the PE array,

where PEs are aligned in a two-dimensional array. Figure 3.1 shows a diagram of this system [3].

A program on the MasPar consists of front-end functions and ACU functions. Parallel computation begins by invoking an ACU function from a front-end function. The memory size in each component is relatively small. The size of data memory in the ACU is 128 K bytes and the size of the memory in each PE is 16 K bytes. Virtual memory is not supported in these memories.

The program instructions are executed serially on each processor as on a conventional machine, the parallel nature lies in the fact that the instructions and variables are broadcasted throughout the parallel array. Such variables are declared *plural* variables and are allocated on the parallel processor array. Other variables which behave in the conventional way are called *singular* variables.

Available programming languages are based on C and FORTRAN. However their extensions are provided allowing to use the parallel array. Our programs are written on MPL which is the parallel version of C.

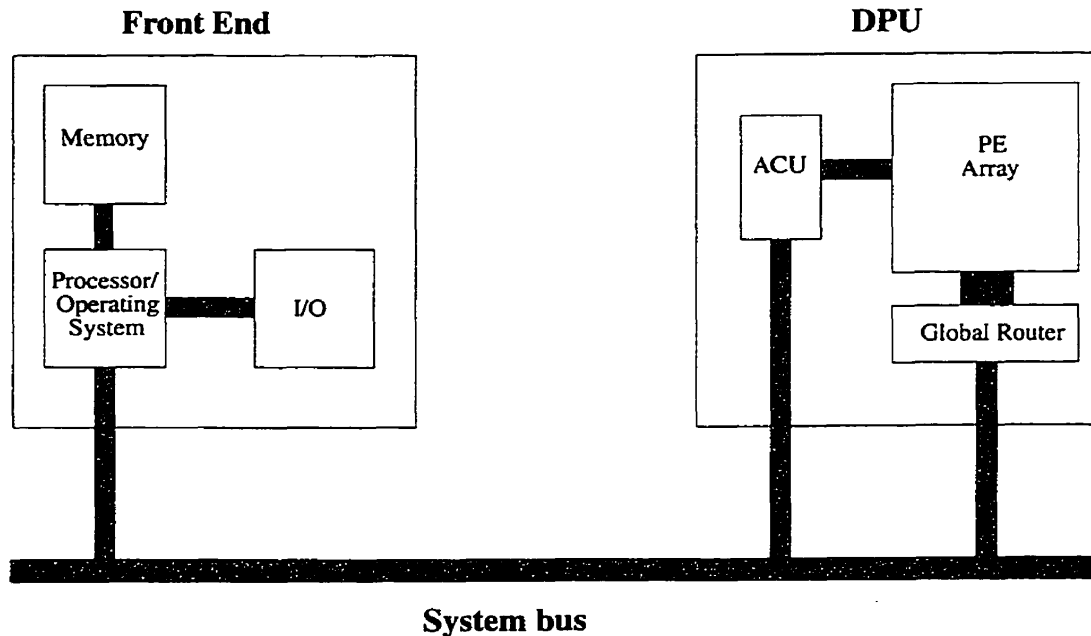


Figure 3.1 MasPar System Diagram.

3.4 Implementation of the Direct problem on MasPar

The first example that we will study in this chapter is a common task in TNDE. It concerns in the inspection of a carbon fiber reinforced plastic (CFRP) block containing an air gap as defect. Its governing heat conduction equations are given as Eq. (2.4) and Eq. (2.47) through (2.54). Boundary and initial conditions are shown in Figure 2.10. they are solved by the finite difference method (explicit) on a uniform lattice.

The sample contains 32 layers. In order to implement the program efficiently on the MasPar system, each layer is divided in a 32x32 matrix of small regions, since this matches the hardware configuration of PEs in the MasPar MP-1. Hence, a sample consists of 32x32x32 nodes. Considering equations 2.8, 2.14 and 2.15, in each iteration, future temperature of these nodes are computed in parallel from their present temperature and the temperature of their neighbors. Since the MasPar system consists of only 2048 PEs (32x64), the following parallelization is then chosen to program the above computational task:

- divide the block in the Z (vertical) direction into two partitions,
- store the layers of X-Y planes one above the other. Figure 3.2 shows both physical schematic and allocation of the plural variables on the MasPar PEs array.

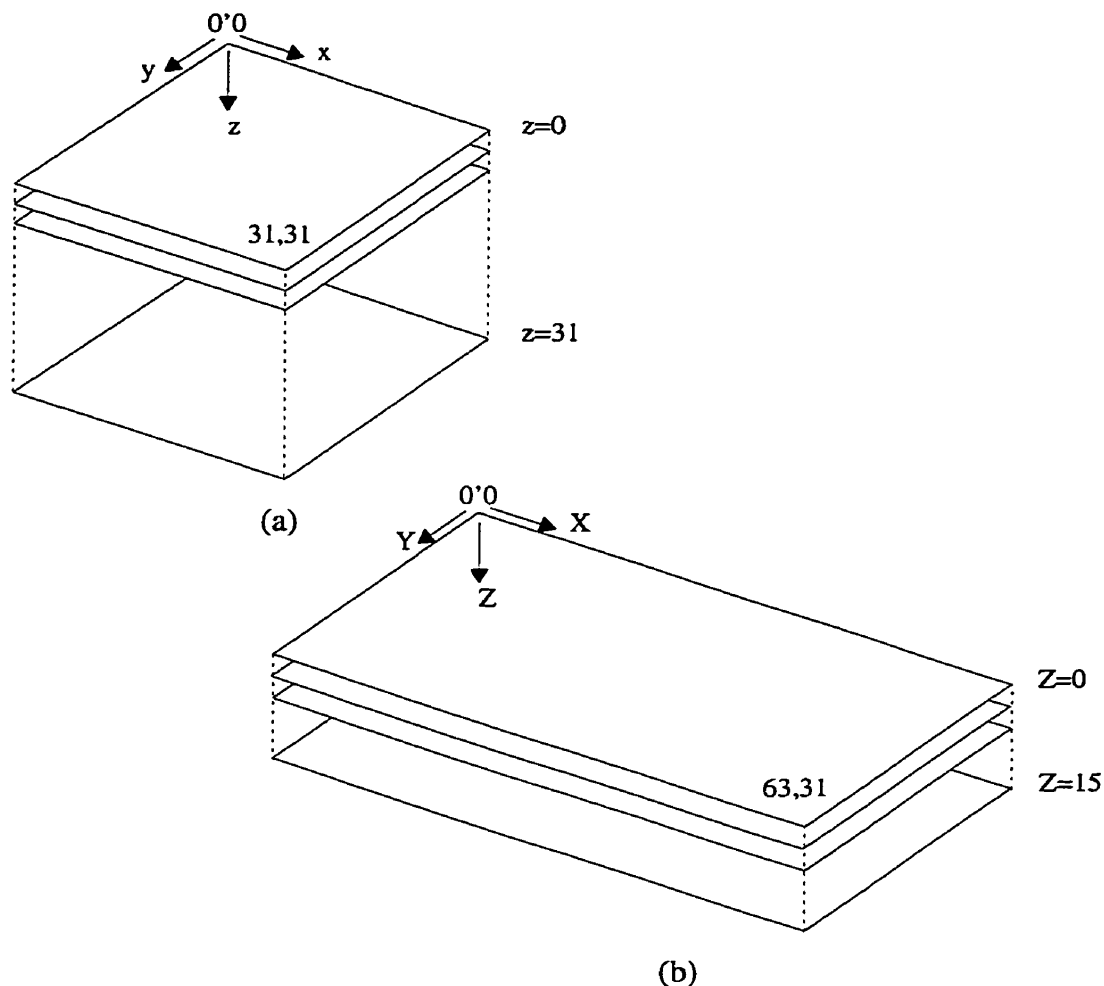


Figure 3.2 a) Physical b) computational storage scheme.

In Figure 3.2-b, each layer represents two layers of the CFRP sample block. The first layer is allocated the 1st and 17th, the second is allocated the 2nd and 18th up to the last layer which is allocated the 16th and 32nd layers of a sample.

3.4.1 Initialization (k_x , k_y , k_z , C_p , ρ , Δx , Δy and Δz)

In our program, thermal properties (k_x , k_y , k_z , C_p and ρ which are respectively thermal conductivity in x, y, and z direction, specific heat and density) and spatial increments (Δx , Δy and Δz in x, y, and z direction) are defined as plural variables and are allocated identically on each PE. Therefore any part of the model can be initialized non-homogeneously depending on the different materials the sample is made of. So, if the

sample has to use close-spaced nonuniform computational lattices, the plural variable option gives us the opportunity to nonuniformly initialize Δx , Δy and Δz in space.

3.4.2 Restriction of Boundary Conditions to Parallel Algorithm

The boundary conditions, which are defined by Eq. 2.49 through 2.54, cause restrictions to our parallel algorithm. To consider these conditions we can partition the processor-element array into different subsets as illustrated in Figure 3.3.

1	8	4	1	8	4
5	9	7	5	9	7
2	6	3	2	6	3

Figure 3.3 Partitioning of the processor-element array into different subset for taking into account the boundary conditions in the computational algorithm.

In subset 1, 2, 3, or 4, two PEs are active at same time and in subset 5, 6, 7, or 8 we have just 30 active PEs but subset 9 contains 1800 active PEs. Now we can consider how the boundary conditions perturb the parallelism. For surface boundary condition Eq. 2.49, we have first to divide the processor-element array into two parts then to apply the above partitioning format for both layer 0 and 16 (Figure 3.2-b). This means that the execution does not happen at the same time for both layers although for a given layer, it happens at the same time.

3.4.3 Communication

X-Net and Global Router are two mechanisms to transfer information between different PEs in the processor-element array. X-Net allows communication between any PE

with any other PE in the array that lies in a straight line from the sending PE in one of 8 possible directions marked N, NE, E, SE, S, SW, W, and NW which can be in communication with the central PE. Hence, those PEs not shaded in Figure 3.4 cannot communicate with the central PE via X-Net [3].

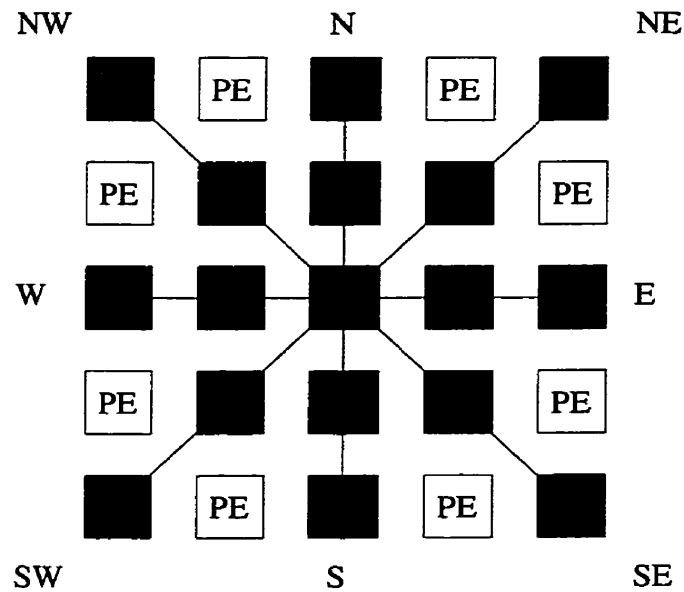


Figure 3.4 X-Net communication through 8 nearest neighbors on MasPar.

Simultaneous communication between any particular PE and the members of an arbitrary subset of PEs is managed by the Global Router. In general, X-Net communication are significantly faster than Global Router communication, but Global Router communication does not impose restrictions on which PEs can be addressed. The bandwidth of X-Net is 16 times faster that of the Global Router.

As shown in Figure 3.2 through Figure 3.4, future temperature of each element depends on eastern, western, northern, southern, up and down neighbors and its present temperature. Communications between central element and four E, W, N, and S neighbors

are performed via X-Net. Furthermore, if we define the temperature variable as a plural vector, both up and down neighbors will be allocated on the same PE. There is no necessity of communication then between PEs except for the nodes on 16th and 17th layer (Figure 3.2-a) which communicate via Global Router to respectively obtain down or up neighbor temperatures.

3.5 Delamination Model Implementation on MasPar

Let's again consider the delamination model which was discussed in section 2.5. In this example we replace the air gap with a TeflonTM block, with thermal properties $k_x = k_y = k_z = k_{def} = 0.0042 \text{ w(cm)}^{-1} \text{ } ^\circ\text{C}^{-1}$ and $\alpha = 1.59 \times 10^{-2} \text{ m}^2\text{s}^{-1}$ as a simulated defect, this is commonly done [4], [5]. It is also assumed that the sample surface is uniformly heated by the input heat flux $Q = 1 \text{ W/cm}^2$ during time $\tau = 2$ second. The initial and boundary conditions are defined as well through Eq. 2.48 to 2.54. For this example the CFRP block dimensions are $L1 = 64 \text{ mm}$, $L2 = 64 \text{ mm}$ and $L3 = 12.8 \text{ mm}$ and the defect dimensions are $x_d = 12 \text{ mm}$, $y_d = 12 \text{ mm}$ and $z_d = 0.4 \text{ mm}$. Taking into account these parameters and the stability criteria given in Eq. (2.22), the simulation parameters are defined as follow:

Table 3.1 Simulation Parameters of CFRP block containing a TeflonTM gap as defect.

Parameters	Values
* h_c	$1 \times 10^{-3} \text{ wcm}^{-2}$
* h_r	$5.67 \times 10^{-12} \text{ wcm}^{-2}$
T_0	0°C
Δt	30 ms
Δx	2 mm
Δy	2 mm
Δz	0.4 mm
nx	32
ny	32
nz	32
τ	2 s
q	1 w

* common values [4], [5]

The model presented in this section, is programmed in MPL (Maspar Programming Language) and executed on the MasPar computer. This gives us the opportunity to use the MPPE (Maspar Programming Environment). MPPE is an integrated graphical environment for developing and debugging programs. It helps to visualize massively parallel data instead of dealing with numbers. Pattern matching is easier when done visually, especially with the huge data sets involved in massively parallel programs (more detailed descriptions of the system are given in the Maspar System Overview and MPPE Manuals) [3].

Figure 3.55-a and Figure 3.5-b show the position of the artificial delamination in the modeled CFRP sample. As mentioned in Table 3.1 nz equals 32 which means we have 32 layers in the sample mesh. In Figure 3.5-a the square contains all the points in the third layer for which the black dots with value of 0.0042 correspond to the thermal conductivity of TeflonTM (defect). Defect size and position are shown as well. Figure 3.5-b shows all the points with a value of 0.008 corresponding to the thermal conductivity of CFRP (sound

material). The left array (all of the points in the big square) indicates the third layer and the right array indicates 19th layer in the sample mesh. The index of $kz[2]$ corresponds to parallel data layer number which is 0 through 15.

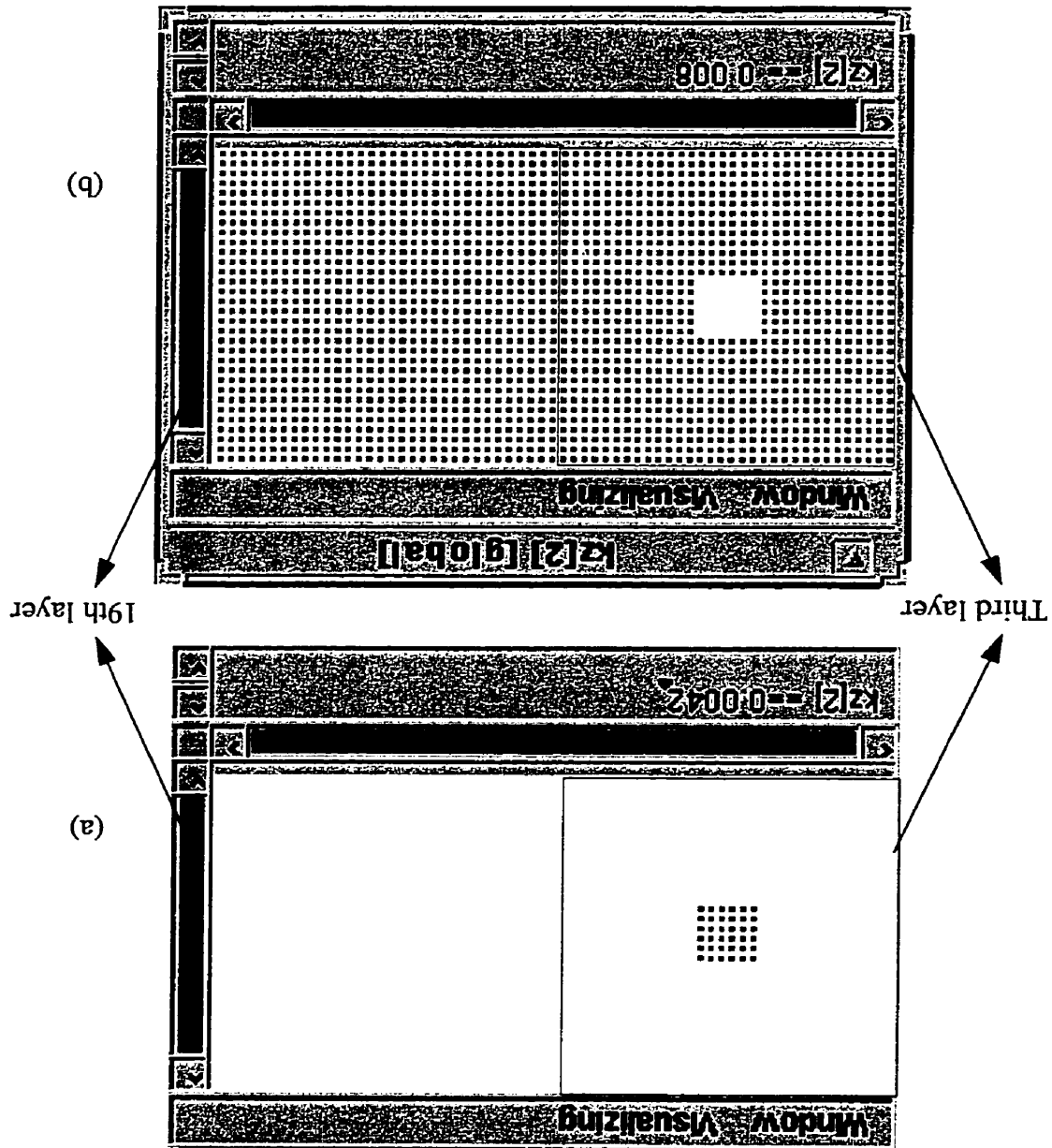
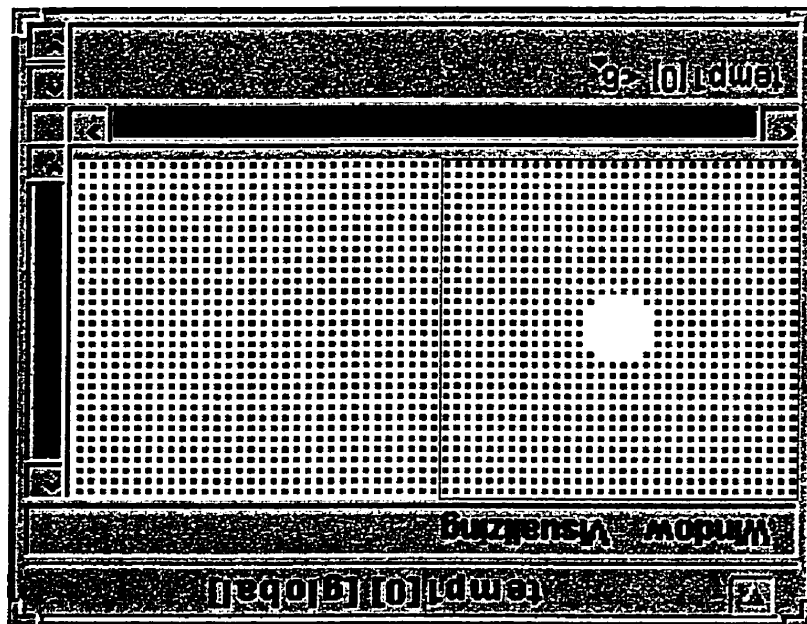
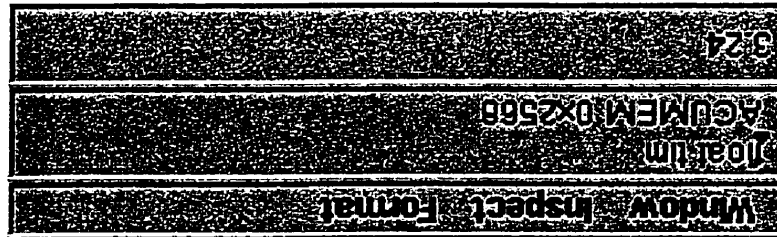


Figure 3.5 (a) shows the points (defect) in third layer having a value of 0.0042 (thermal conductivity of Teflon™) and (b) shows the points (sound material) in third and 18th layer having a value of 0.008 (thermal conductivity of CFRP (Fibers)) both in $W/(cm \times ^\circ C)$.

Figure 3.6-a shows temperature distribution on the surface of the modeled CFRP sample which is shown in Figure 2.10. This temperature difference map is recorded 3.24 s after the beginning of the process. The white region corresponds to the points with temperature difference (with respect to T_{∞} , ambient temperature), greater than 6°C . The anomalous temperature distribution is due to the delamination-type defect in the model (TeflonTM).



(a)



(b)

Figure 3.6 (a) Temperature distribution on the surface (left array) and 18th layer (right array) of sample of Figure 2.10 which contains a delamination defect. (b) Time (s) of recording.

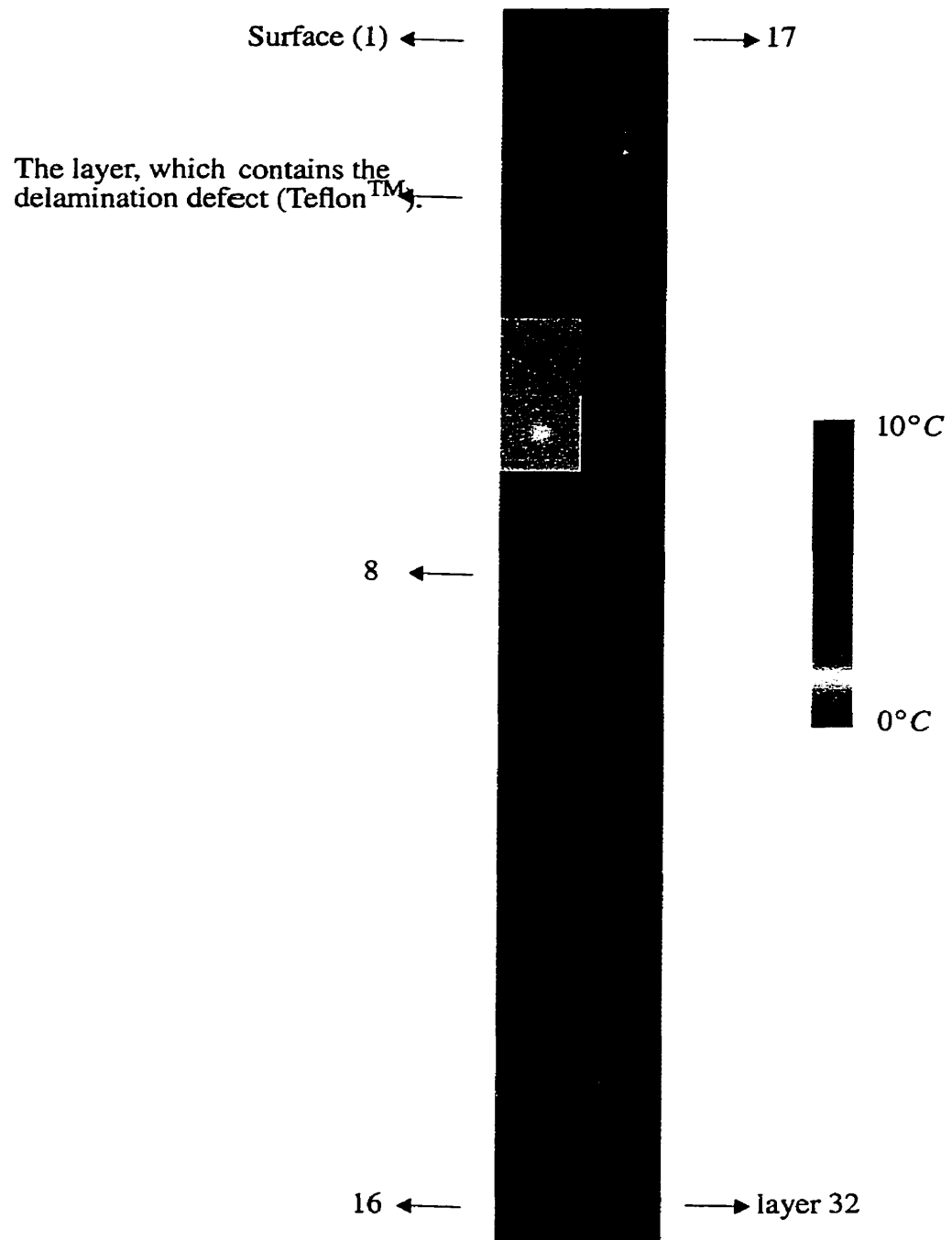


Figure 3.7 Temperature distribution images over 32 layers of modeled CFRP sample when the contrast is maximum on the surface. Notice the subtle differences that vanishes temperature deeper in the sample layer (8 and deeper).

The image, which is presented in Figure 3.7, shows the temperature distribution over 32 layers in the modeled specimen. This image has been obtained at the time thermal contrast is maximum on the surface of the sample. The third square (blue) concerns the third layer of the sample which contains the delamination-type defect. The defect effect is also revealed on the other layers (above or below the real defect position) but it is seen more clearly at defect interface.

In chapter 2 we compared the numerical solution with its analytical solution for an homogenous CFRP sample in order to check the accuracy of our numerical solution. To compare the simulation results on MasPar computer with a sequential program, we have modeled a similar direct problem with “TERMO.HEAT,” a commercial software which is available in our laboratory. The temperature evolution and contrast on the sample surface for both parallel and sequential versions are respectively shown in Figure 3.8 and Figure 3.9. Differences between two programs are small (less than 5 °C at maximum) which brings us confidence in our model and implementation that will be used thereafter.

3.6 Advantages of the Direct Problem Implementation on MasPar System

Firstly, the comparison with known dedicated programming systems for high-accuracy computations on sequential computers shows that the MasPar system ensures similar accuracy of results. Moreover, it provides very high performance due to effective use of massive parallelism. For example, in the sequential version of the direct heat conduction problem applied on infrared thermography, the region temperature values are represented by 32x64 arrays, and thus the loop body consists of two inner loops, one for the y axis and the other for the x axis. In the parallel version, the matrix of regions is directly mapped onto the physical matrix of PEs. Thus the loop body contains no inner loops. Instead, each PE obtains values from its neighbors to compute the next temperature values for the element that the PE is responsible for. Compared with the interpreted execution of the sequential version, it is clear that the parallel version runs quite faster.

Secondly, the MasPar system comes with the MasPar Programming Environment (MPPE) which is an interactive set of tools for debugging and optimizing our MasPar-compiled program. MPPE simplifies our development effort by providing a graphical and intuitive environment for our work. It is used to:

- step through our program,

- inspect parallel data values,
- graphically display usage of the data processing elements in the DPU (Data Parallel Unit),
- and finally allows the processing time to be reduced.

Among disadvantages of the MasPar are the limited number of PEs available and also the limited availability of such a machine worldwide.

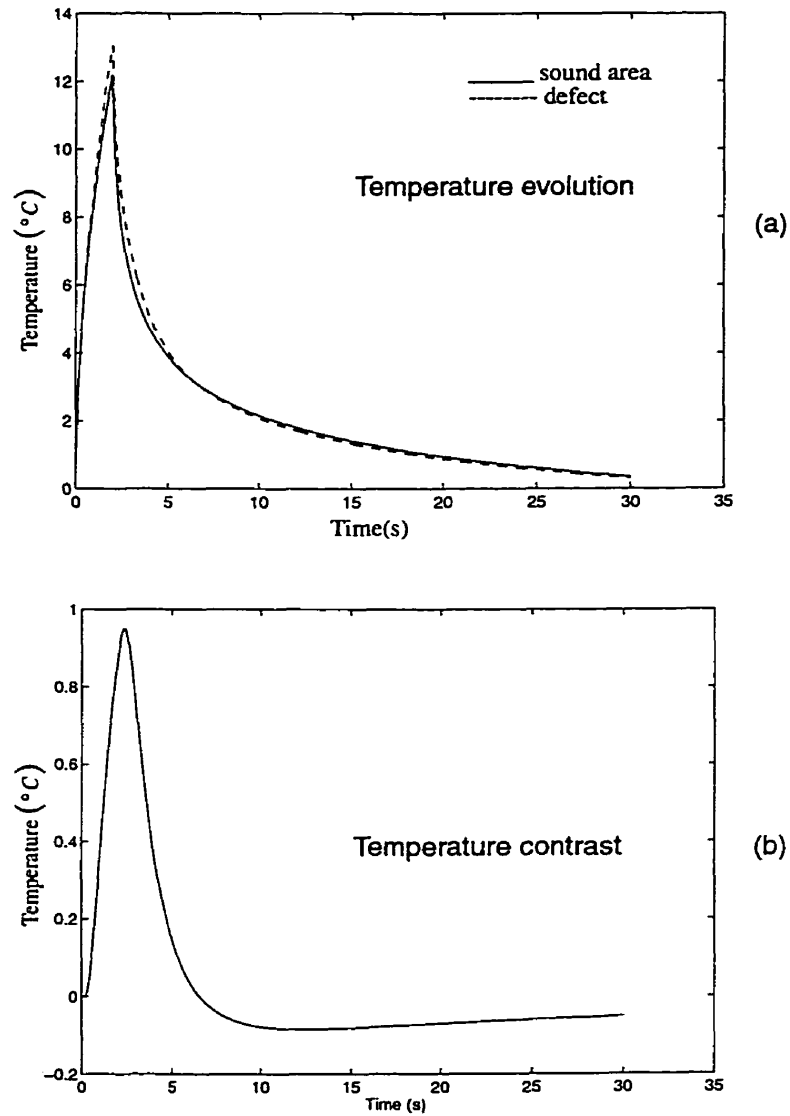
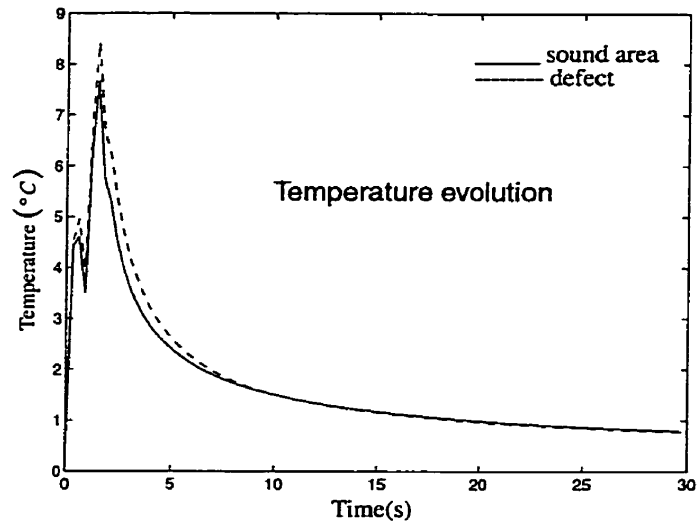
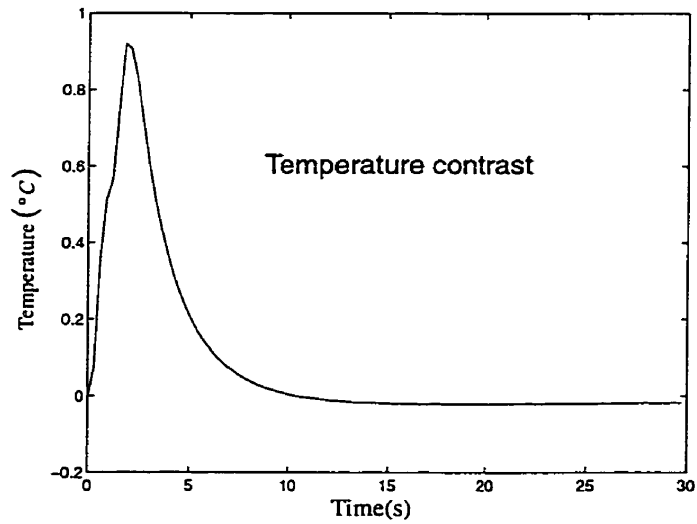


Figure 3.8 Time dependence of (a) surface temperature and (b) the thermal contrast of CFRP modeled sample containing delamination defect in parallel simulation.



(a)



(b)

Figure 3.9 Time dependence of (a) surface temperature and (b) the thermal contrast of sequential version "TERMO.HEAT" for a similar CFRP modeled sample containing delamination defect.

3.7 Conclusion

Modeling of delamination-type defects in CFRP and parallel implementation results on MasPar MP-1 were explained in this chapter. Here, the MPPE (MasPar Programming Environment) allows us to investigate what is happening in our program at crucial points by providing different ways to examine the variables, expressions, and routines. Visualization of defect effects in different regions of the sample at different times is very simple using MPPE which makes easy to modify the modeling of direct problem. Although we demonstrated the clear superiority of a parallel approach with respect to a sequential approach in term of execution speed, recent developments of high speed sequential machines bring now sufficient performance to implement the 3-D direct problem on them. This is why the MasPar computer available at Université Laval has been out of service since 1998.

3.8 References

- [1] Yu. M. Matsevityi and V. P. Sheryshev, "Modeling of Heat-conducting Bodies; Lumped Capacitance Concept. I. Hierarchical Models", *Electron. Modeling*, Vol. 9(4), 1992, pp. 634-644, 1992, Gordon & Breach Science Publishers, S. A., printed in the United Kingdom.
- [2] A. Darabi "Massively Parallel Modeling of the Direct Problem in Infrared Thermography Applied to the Nondestructive Evaluation of Material" Master thesis, Universite Laval, October 1995.
- [3] *MPL (MasPar Programming Language) Manuals*, MasPar Computer Corporation, Sunnyvale, California, 1992.
- [4] X. Maldague, "Nondestructive Evaluation of Materials by Infrared Thermography", Springer-Verlag London Limited, 1993.
- [5] V. Vavilov, X. Maldague, B. Dufort, F. Robitaille and J. Picard, "Thermal nondestructive testing of carbon epoxy composites: detailed analysis and data processing", *NDT&E International* Volume 26 number 2, 85-95, 1993.

CHAPTER 4

Artificial Neural Networks

4.1 Introduction

The theoretical work on artificial neural networks (NN) began in 1943 with the classical paper of Mcculloch and Pitts in which the authors introduced the brain as a computer, consisting of well-defined computing elements, the neurons [1]. As compared to silicon logic gates, neurons are five or six orders of magnitude slower. In a current silicon chip events happen in the nanosecond (10^{-9} s) range, whereas neural events happen in millisecond (10^{-3} s) range. The human cortex contains about 10 billion neurons and 60 trillion synapse or connections [2]. However, perceptual decisions such as face recognition are typically made by humans within a few hundred millisecond. This implies that the brain runs parallel programs of about 100 steps long to perform such perceptual tasks.

A general NN comprises two main sets of components-neurons and interconnected weights, whose functionality is roughly based on biological neurons. It resembles the brain

in two aspects. The first, knowledge, is gained by the network through a learning process, and the second, inter-neuron connection strength known as synaptic weights are used to store the knowledge.

In this chapter we present a simplified description of neural networks (NN) and explain how these artificial neurons can be interconnected to form a variety of network architectures. We will also study perceptron training algorithms in feed forward networks, so that they can learn to solve classification problems. Finally, the chapter continues with a detailed study of the back propagation algorithm. This generalized LMS (Least Mean Square) algorithm can be used to train multilayer networks.

4.2 Artificial Neurons

A typical multiple-input neuron is shown in Figure 4.1. The information processing performed in this way can be summarized as follows: The individual inputs x_1, x_2, \dots, x_R are multiplied by corresponding weights $w_{1,1}, w_{1,2}, \dots, w_{1,R}$. The weighted signals and neuron bias b are summed to produce an overall neuron activation signal n [3]:

$$n = w_{1,1} \times x_1 + w_{1,2} \times x_2 + \dots + w_{1,R} \times x_R + b = \left(\sum_{i=1}^R w_{1,i} \times x_i + b \right). \quad (4.1)$$

This may be represented in matrix form:

$$n = \mathbf{WX} + b \quad (4.2)$$

where for single neuron, matrix \mathbf{W} has just one row. The output y is then given as:

$$y = f(\mathbf{WX} + b) \quad (4.3)$$

where y is the output of the unit, f is a linear or nonlinear transfer function, \mathbf{X} is input vector, \mathbf{W} is weight matrix and b is bias or a threshold value for the artificial neuron.

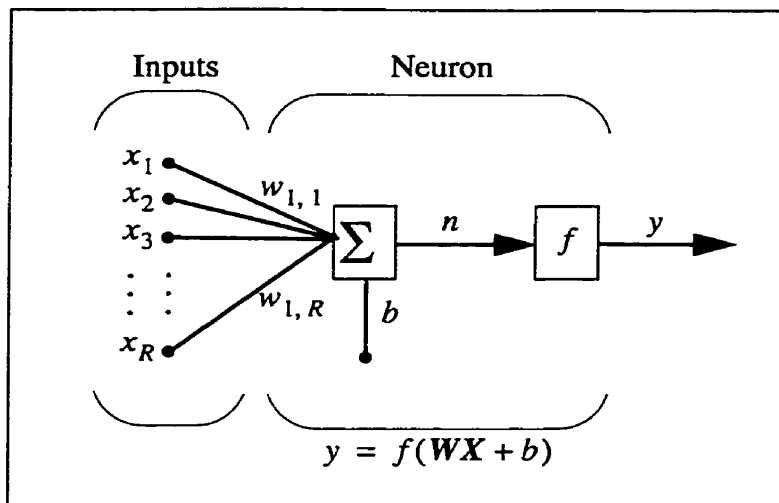


Figure 4.1 A typical multiple-input neuron.

The actual output y depends on the transfer function f that is chosen. Three of the most commonly used transfer functions are illustrated in Figure 4.2. The first function (Figure 4.2(a)) is a threshold function which is sometimes called step or hard-limit transfer function. Therefore, the output y given in Eq. 4.3 is “0” if the function argument (neuron activation signal) is less than “0” or “1” if its argument is greater than or equal “0”. Figure 4.2(b) shows a linear transfer function. The output of such a function is equal to its input:

$$y = f(WX + b) = f(n) = n \quad (4.4)$$

The third transfer function is a sigmoid function which is represented in Figure 4.2(c). Its output can be written as:

$$y = f(n) = \frac{1}{1 + e^{-n}} = \frac{1}{1 + e^{-(WX + b)}} \quad (4.5)$$

The Eq. (4.5) implies that the sigmoid transfer function takes input n with any values between plus and minus infinity and translates the output y into the range “0” to “1”.

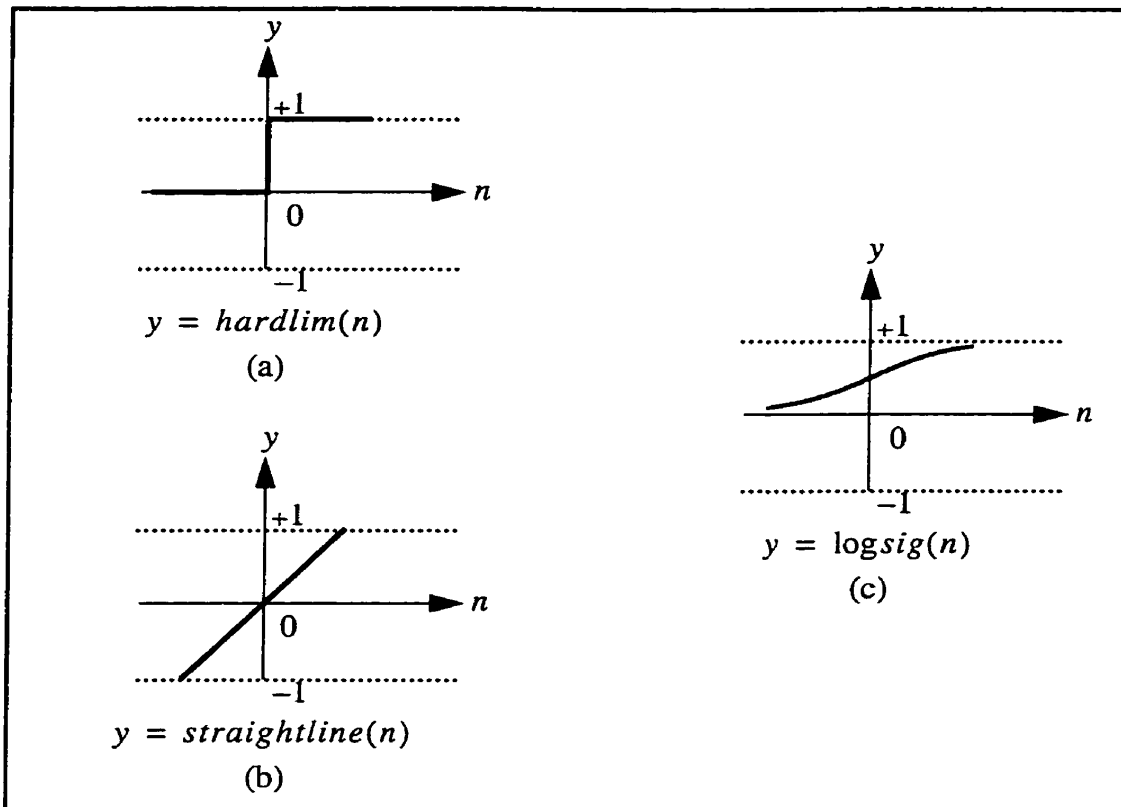


Figure 4.2 The most commonly used transfer functions in ANNs: (a)hard limit (b)linear (c) sigmoid transfer function.

4.3 Network Architectures

The architecture or connection pattern of neurons in artificial NN (ANN) specifies its physical layout. Based on the connection pattern, two different classes of networks are identified [4]:

- feed-forward networks, in which architectures have no loops and,
- recurrent networks, in which architectures have at least one feedback loop.

The feed-forward networks are made up of sets of neurons arranged in layers that have unidirectional connections between them. The outputs of feed-forward networks are made of only one set of values for a given input vector and is independent of the previous network state. They are also called memory-less or static networks.

The recurrent networks consist of a single layer of neuron with each neuron feeding its output to the inputs of all other neurons. It can include self-feedback loops (feeding its output to its own inputs) or contains hidden neurons. Their output values depend of previous network state and they can modify the inputs of the neurons when a new input vector is presented to the network. Therefore they are called dynamic networks [5], [6], [7].

4.4 Learning

One of the interesting properties of neural networks is their ability to learn from their environment in order to improve their performance [8]. Suppose, we have a set of P input-output pairs, $(x_1, y_1), (x_2, y_2), \dots, (x_p, y_p)$ which are samples from function $f: R^n \rightarrow R^m$. In other words, the function f maps n -dimensional vectors x to m -dimensional vectors y . The network has learned the function f if its response is:

$$y = f(x) \text{ for all } x \quad (4.6)$$

and it has partially learned the function f if it responds with y' close to y given in Eq. (4.6).

In NN, learning means any change in any synaptic parameters (weights and biases) when the networks are stimulated by their environment. Learning paradigms fall into three main classes: supervised, unsupervised, and hybrid. Supervised learning rules use pattern class information (output target vectors) and determine weights and biases to allow the network to produce answers as close as possible to the target vectors. In contrast, unsupervised learning rules use only critics on the network correction not target vectors themselves. Unsupervised learning networks adaptively regroup patterns into clusters or decision classes. In hybrid learning, part of synaptic-values are often determined through supervised learning, and the others are adjusted through unsupervised learning.

4.5 Perceptron Learning Rule

The perceptron, LMS, and back-propagation are the most known supervised learning algorithms. The perceptron is a feed-forward network with one output neuron that

separates linearly separable sets of input patterns. It is based on an error-correction rule. The error-correction rules use the error signal [3]:

$$e = t - y \quad (4.7)$$

to modify the connection weights and biases to gradually reduce this error.

Now, let us consider a single neuron perceptron network with adjustable weights and bias as shown in Figure 4.3. The output of the network is given by:

$$y = \text{hardlim}(wx + b) \quad (4.8)$$

and its value is:

$$y = \text{hardlim}(n) = \begin{cases} 1 & \text{if } n \geq 0 \\ 0 & \text{if otherwise} \end{cases} \quad (4.9)$$

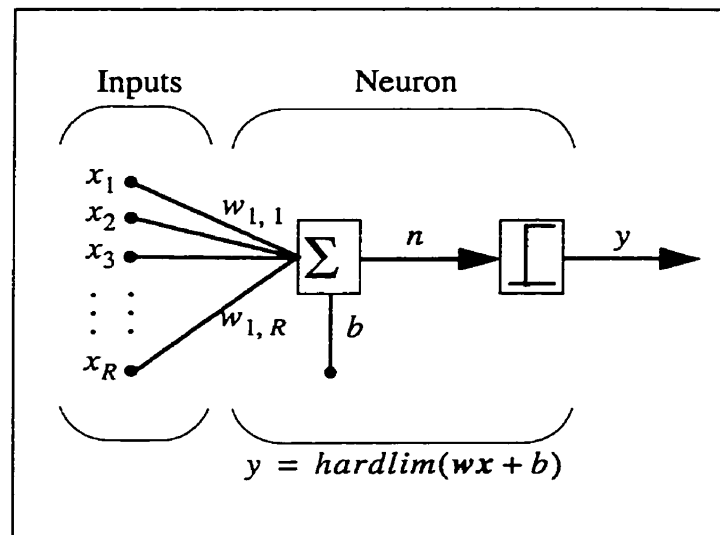


Figure 4.3 A typical single neuron perceptron network.

Therefore the linear equation

$$wx + b = 0 \quad (4.10)$$

defines the decision boundary (a hyperplane in the n -dimensional input space) that halves the space. The perceptron learning rule is provided with a set of examples of proper net-

work behavior:

$$\{\mathbf{x}_1, t_1\}, \{\mathbf{x}_2, t_2\}, \dots, \{\mathbf{x}_p, t_p\} \quad (4.11)$$

where \mathbf{x}_p is an input vector to the network and t_p is the corresponding output target.

After initializing the network, the input vectors are applied to it. The network error for the j th iteration is defined as:

$$e(j) = t(j) - y(j). \quad (4.12)$$

Consequently, the synaptic weights and bias will be updated according to:

$$\mathbf{w}(j+1) = \mathbf{w}(j) + ae(j)\mathbf{x}(j) \quad (4.13)$$

$$b(j+1) = b(j) + ae(j) \quad (4.14)$$

Where $\mathbf{w}(j)$ is the synaptic weight vector, $\mathbf{x}(j)$ is the input vector, and $b(j)$ is the bias at j th iteration, a is a constant learning rate, and $\mathbf{w}(j+1)$ and $b(j+1)$ are respectively synaptic weight vector and bias for the $(j+1)$ th iteration.

Both Eq (4.13) and Eq.(4.14) are rules for updating the network connection parameters until all pattern vectors are correctly classified. The proportionality factor $ae(j)$ is zero or vanishingly small if the given pattern $\mathbf{x}(j)$ is correctly classified. In most cases, it is impossible to satisfy all the equations:

$$y(j) = t(j) = \text{hardlim}(\mathbf{w}(j)\mathbf{x}(j) + b(j)) \quad (4.15)$$

$$j = 1, 2, \dots, p$$

This means the network corrections never stop. To ensure the convergence, learning rate a should decrease as iteration proceeds. However, when the network has converged it does not necessarily yield valid synaptic parameters that will classify all patterns correctly.

To give an example, we consider a two-input perceptron with one neuron as shown in Figure 4.4. It is sufficient to solve a problem such as the NAND gate implementation which is linearly separable into two classes. This network is provided with a set of examples corresponding to the NAND gate truth table as [9]:

$$\{\mathbf{x}, t\} = \{(0, 0), 1\}, \{(0, 1), 1\}, \{(1, 0), 1\}, \{(1, 1), 0\} \quad (4.16)$$

The input vectors can be divided into two classes. Three of them associated with the output target 1 and the last one associated to output target 0. We initialize the synaptic weights and bias to random values. Figure 4.5 shows how this initial network (dash-dotted line) halves the input space. As shown the o and $+$'s (the two input patterns) are not correctly positioned.

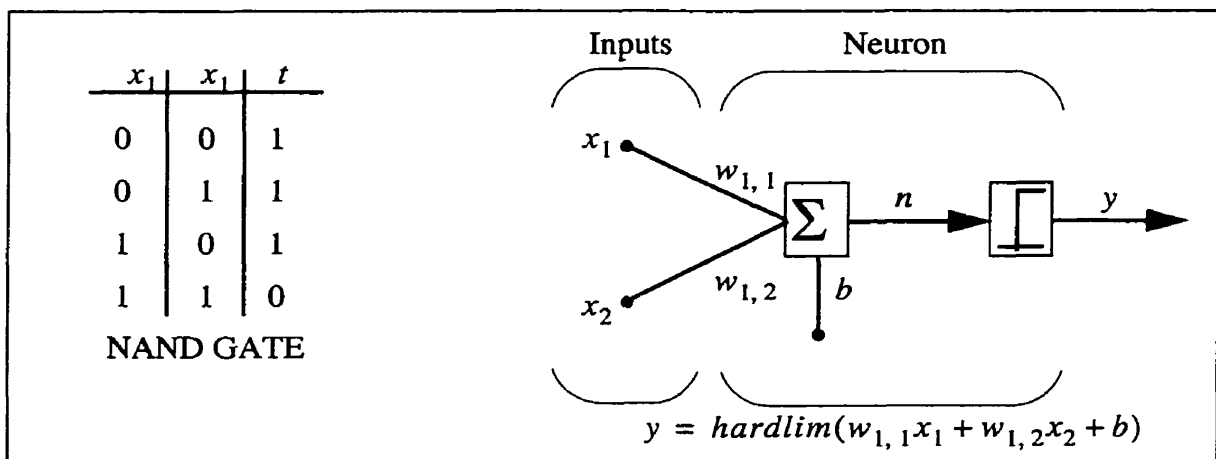


Figure 4.4 A two-input single neuron perceptron.

Next the network is ready to be trained. The Figure 4.6 shows how the network gradually adjusts its synaptic weights and bias to divide the input space until all of the vectors are classified properly. Dash-dotted and dotted lines show respectively initial and intermediate states of the network, while the solid line shows the final solution.

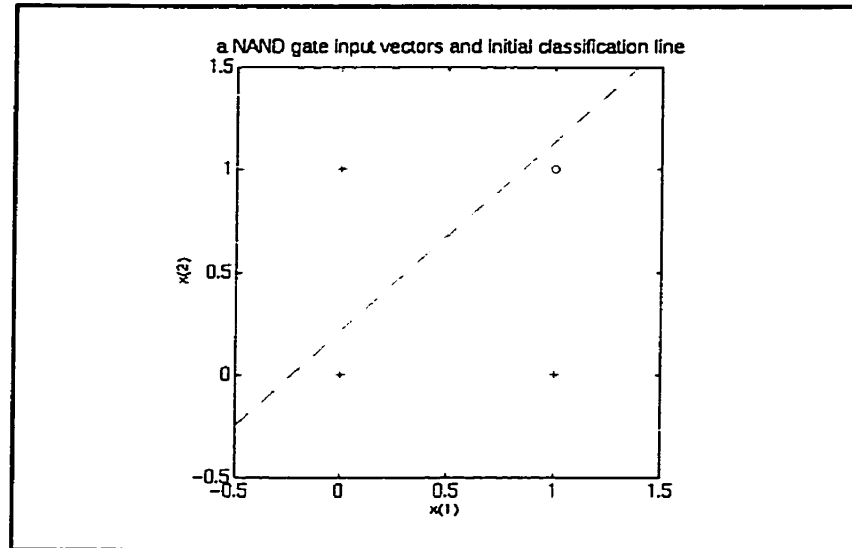


Figure 4.5 Input vector and initial decision boundary for a two-input single neuron perceptron.

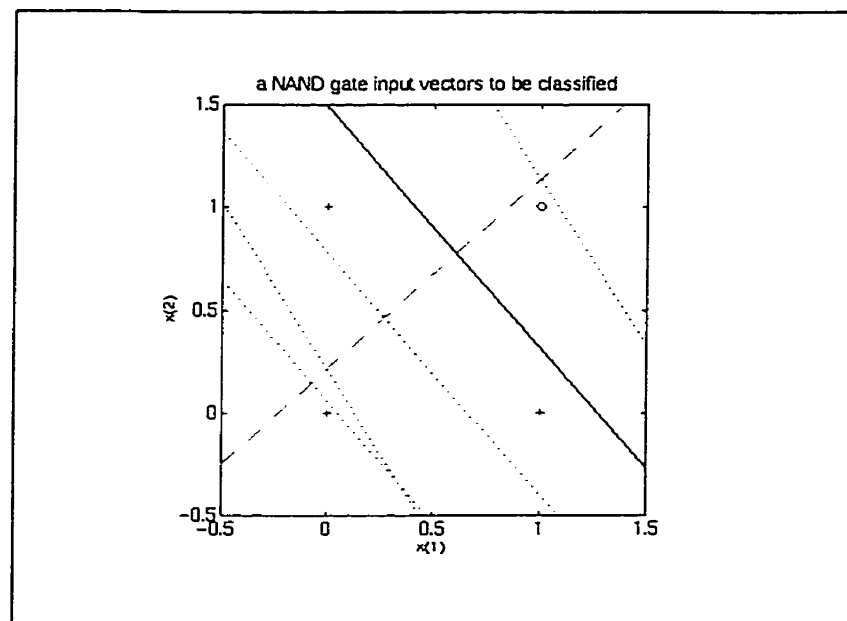


Figure 4.6 Final decision boundary for a two-input single neuron perceptron, NAND gate implementation problem.

The Exclusive OR function “XOR” is the best known case of a non-linearly separable logic gate, the truth table is given by [9]:

XOR GATE

x_1	x_2	<i>output</i>
0	0	0
0	1	1
1	0	1
1	1	0

Lets use a perceptron with two input cells and one output cell. This perceptron has also two weights W_1 and W_2 which connect the inputs to the output. If the threshold $b = 0$, then association of the input values (1,0) to the output ‘1’ implies $W_{1,1} > 0$ and the fact of associating the input values (0,1) to the output ‘1’ implies $W_{1,2} > 0$. Next, if we enter (1,1) as inputs, the perceptron output’s is ‘1’ based on the equation:

$$y = \text{hardlim}(w_{1,1}x_1 + w_{1,2}x_2 + b). \quad (4.17)$$

This is the opposite of how we want to train the proposed perceptron. So, it is thus impossible to find the correct $W_{1,i}$ values in this case. To solve non-linearly separable problems such as the “XOR” problem, we need hidden neurons or layers. This is discussed in next section as in the case of multi-layer perceptron or back-propagation neural networks.

4.6 Back-Propagation Learning Rule

In contrast to the sequential nature of the Von Neuman machine, the back-propagation neural network is a processing system that can examine all the pixels in the image in parallel. While the perceptron and LMS (Least Mean Square algorithm) are single layer networks used to solve classification problems which can be linearly classified, the back-propagation network consists of hidden layers to enable solving complex and non-linear classification problems. It can adapt itself to “learn” the relationship between a set of

example patterns and apply the same relationship to a new input pattern. It can focus on specific features when an arbitrary input resemble other patterns seen previously, such as those pixels in a noisy image that “look” like a known object or character submerged in the noise. Rumelhart et al. popularized the back-propagation algorithm in 1986 [2], [5]. Since, then, it has been used to solve efficiently different and various problems.

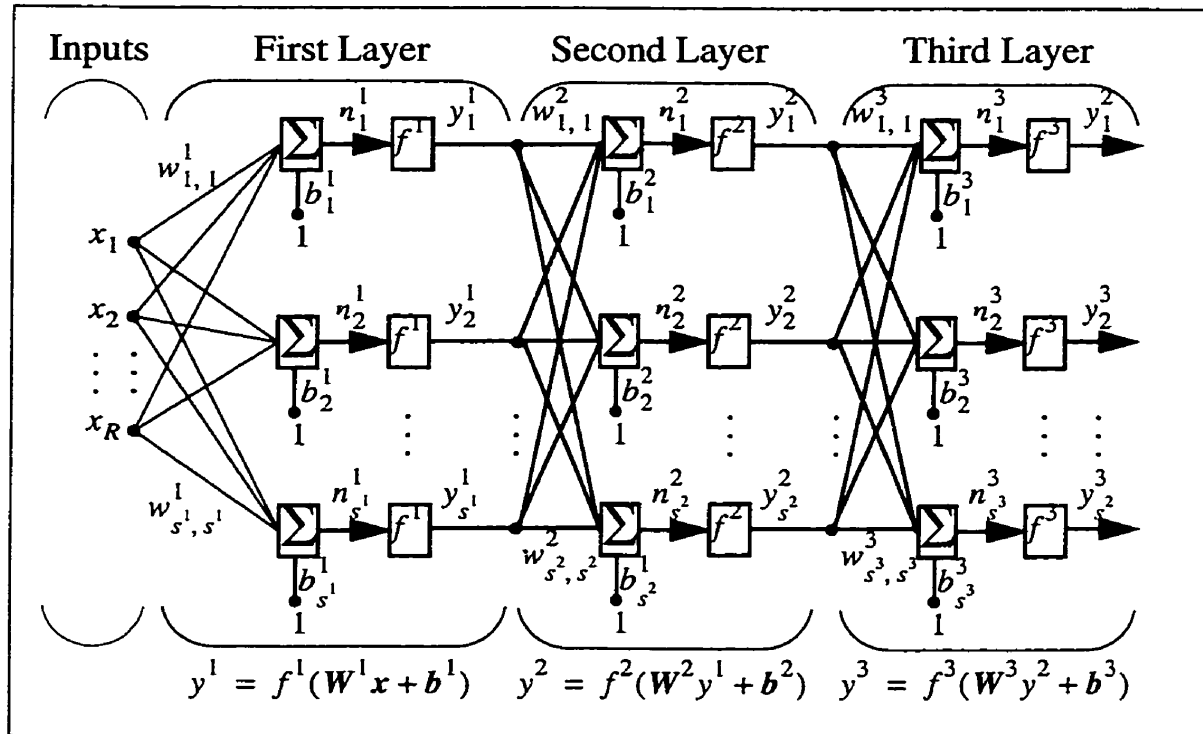


Figure 4.7 A three-layer feed-forward neural network.

To describe the back-propagation algorithm, let us consider a three-layer perceptron as the one shown in Figure 4.7. Each layer has its own connection weight matrix W^l , its own bias vector b^l , a net input vector n^l , and an output vector y^l ; s^l is the number of neurons in each layer. Superscript l identifies the layer number. The output vectors can be described as [3]:

$$y^{l+1} = f^{l+1}(W^{l+1} y^l + b^{l+1}) \quad \text{for} \quad l = 0, 1, \dots, L-1 \quad (4.18)$$

The external input vector is:

$$\mathbf{y}^0 = \mathbf{x} \quad (4.19)$$

and the network output vector is:

$$\mathbf{y} = \mathbf{y}^L \quad (4.20)$$

where L is the network layer's number.

Suppose, the back-propagation algorithm is provided with a set of input/output vector pairs as training set:

$$\{\mathbf{x}_1, \mathbf{t}_1\}, \{\mathbf{x}_2, \mathbf{t}_2\}, \dots, \{\mathbf{x}_p, \mathbf{t}_p\}. \quad (4.21)$$

Now, we want to train the network. As each input vector is presented to the network, its actual output \mathbf{y} is compared to corresponding target vector. The back-propagation algorithm (a generalization of the LMS algorithm) should adjust the synaptic parameters in order to minimize the mean square error [3]:

$$F(\mathbf{z}) = E[\mathbf{e}^T \mathbf{e}] = E[(\mathbf{t} - \mathbf{y})^T (\mathbf{t} - \mathbf{y})]. \quad (4.22)$$

Where \mathbf{z} is the synaptic parameters vector and E is the expectation taken over all of the training set.

To approximate the mean square error, we replace the expectation of squared error by the squared error itself at iteration k :

$$\hat{F}(\mathbf{z}) = \mathbf{e}^T(k) \mathbf{e}(k) = (\mathbf{t}(k) - \mathbf{y}(k))^T (\mathbf{t}(k) - \mathbf{y}(k)). \quad (4.23)$$

From Eq. 4.22, we can drive the approximate steepest descent algorithm for multi-layer network in matrix form as:

$$\mathbf{W}^l(k+1) = \mathbf{W}^l(k) - a s^l (\mathbf{y}^{l-1})^T, \quad (4.24)$$

$$\mathbf{b}^l(k+1) = \mathbf{b}^l(k) - a s^l, \quad (4.25)$$

where a is the learning rate s^l is the sensitivity of \hat{F} to the accumulate input vector at layer l that can be given by [3]:

$$s^l = \dot{F}^l(\mathbf{n}^l)(W^{l+1})^T s^{l+1} \quad (4.26)$$

where:

$$\dot{F}^l(\mathbf{n}^l) = \begin{bmatrix} \frac{\partial f^l(\mathbf{n}^l_1)}{\partial \mathbf{n}^l_1} & 0 & \dots & 0 \\ 0 & \frac{\partial f^l(\mathbf{n}^l_2)}{\partial \mathbf{n}^l_2} & \dots & 0 \\ \vdots & \vdots & & \vdots \\ 0 & 0 & \dots & \frac{\partial f^l(\mathbf{n}^l_{s^l})}{\partial \mathbf{n}^l_{s^l}} \end{bmatrix} \quad (4.27)$$

Here, f^l is the transfer function of the neurons in layer l .

Now, we can see in Eq. 4.26 how the sensitivities are propagated backward through the network. If we know the sensitivity of the last layer we can then compute other sensitivities with Eq. 4.26 as:

$$s^L \rightarrow s^{L-1} \rightarrow \dots \rightarrow s^2 \rightarrow s^1. \quad (4.28)$$

The last layer sensitivity vector s^L can be derived as:

$$s^L = 2\dot{F}^L(\mathbf{n}^L)(t - \mathbf{y}). \quad (4.29)$$

Within a more general framework, the learning procedure consists to present the inputs to the network and then ask it to modify its weights so that the corresponding output is found. After initializing the network, the algorithm propagates the inputs forward until a computed output is obtained it then compares the computed output with the desired output to get the error. If this error does not satisfy the error constraint it will be propagated backward through the network to modify the weights so that in the next iteration, the error made between the calculated and known outputs is minimized. This process is repeated until a negligible error is obtained.

Multi-layer feed-forward NN have been successfully applied to pattern recognition and function approximation during the past decade [2], [5], [3]. For example, consider a $\text{sinc}(x)$ ($\sin(x)/x$, $x \in [-4\pi, 4\pi]$) function shown in Figure 4.8. Now, in order to approximate the $\text{sinc}(x)$ function we propose a two layer feed-forward NN, 10 neuron with the ‘tansig’ (Figure 4.2) activation function in hidden layer and one output neuron with the ‘straightline’ (Figure 4.2) activation function. First, the network is trained with input/target data pairs which are represented by bold dots on the figure. Performance, MSE, of the network for 100 epochs during the training procedure is depicted in Figure 4.9. The network performance is tested by both training data and test data. The network outputs are respectively defined by circle-dots and square dots on the figure. The star-dot point corresponds to network output at $x = 0$ where $\sin(x)/x$ can not be defined mathematically.

The next example employs multi-layers feedforward neural network to approximate temperature evolution function given in section 2.4. For this purpose two architectures are tested. It should be noted that the network output precision depends on the number of the neurons in the hidden layer. On the other hand, if the number of the hidden neurons is increased then the training procedure time will augment. Figure 4.10 shows the results obtained for two cases. The top figures illustrate respectively the approximated function and network performance for a network with 18 neuron in hidden layer and the bottom figures are related to the estimated function and network performance for a network with 30 neuron in hidden layer.

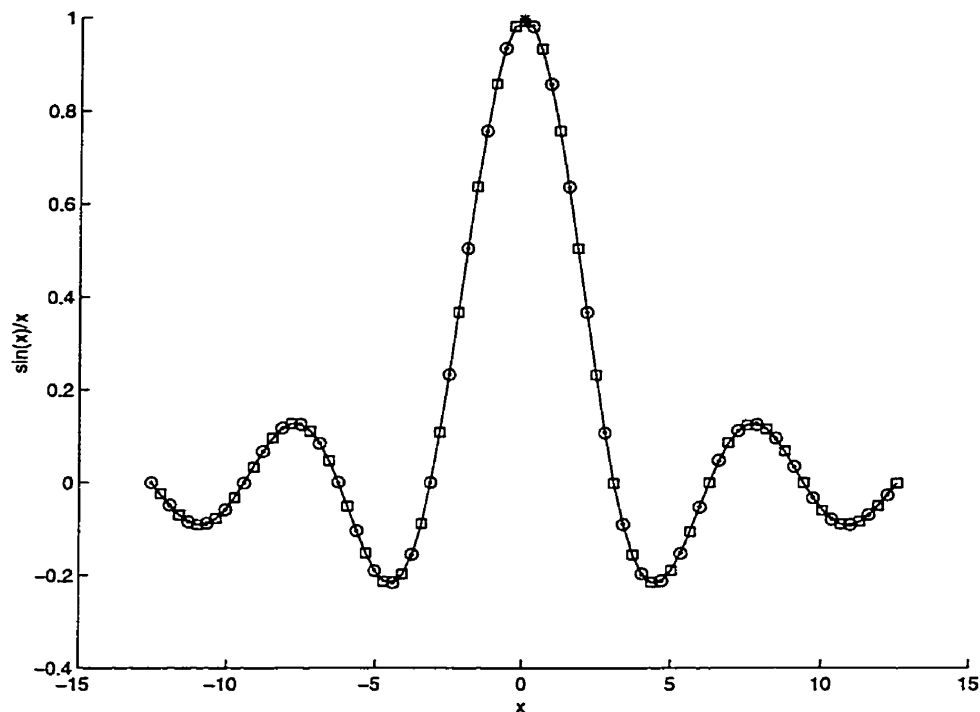


Figure 4.8 Estimated $\sin(x)/x$ function by a two layer feedforward neural network, 10 neuron with 'tansig' activation function in hidden layer and one output neuron with 'purelin' activation function. Bold dots, circle-dots, square-dots respectively correspond to training data, the network output for training data and the network output for test data.

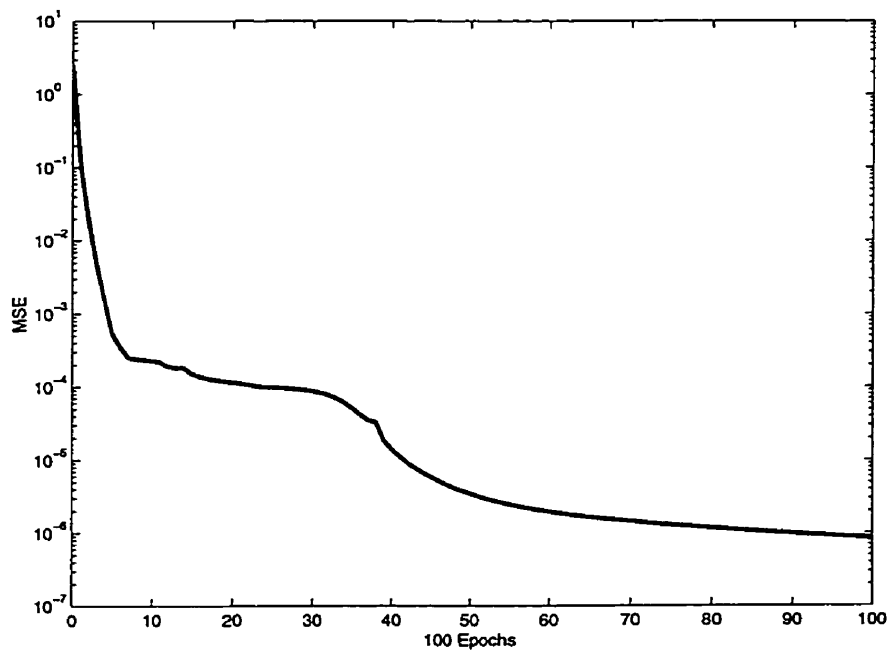


Figure 4.9 The network's MSE, mean square error, during training procedure

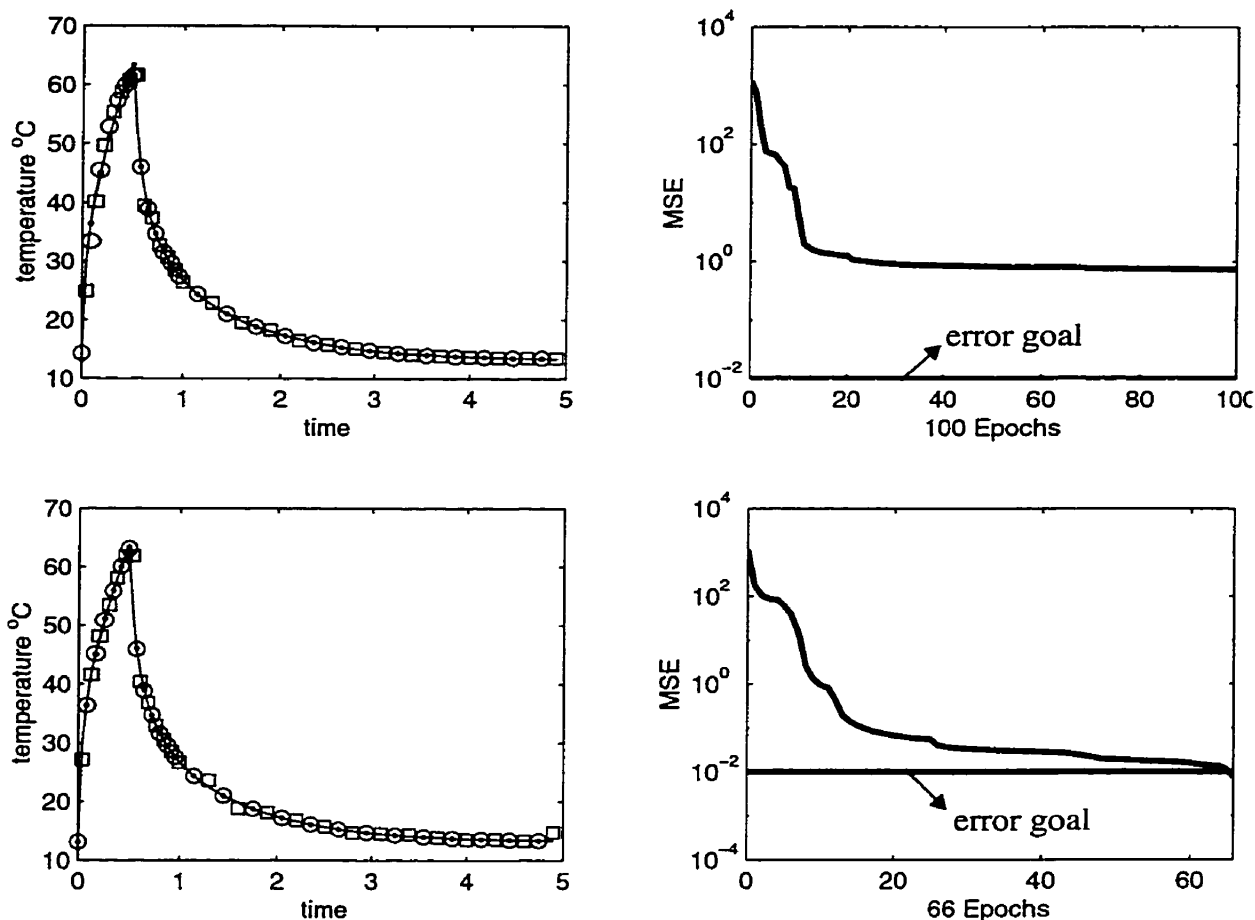


Figure 4.10 Estimated temperature evolution function and network performance: for two feedforward network with 18 neuron (top figures) and 30 neuron (bottom figures) in hidden layer.

4.7 Conclusion

In this chapter perceptron and multi-layers feedforward NN were studied. The given example shows that the perceptron networks can be applied to the simple linear classification problems. However it can not treat the nonlinear classification problems such as the thermal evolution function approximation problem applied to TNDE. For this case, multi-layer feedforward NNs are well suited to achieve pattern recognition and nonlinear function approximation problems. It is assumed that the multi-layer feedforward NN with enough neurons in the hidden layer can achieve any complex nonlinear function and classification applications. The major disadvantages of feedforward neural networks are

their supervised nature and tendency to converge to local minima. Faster convergence should be provided by using some algorithms such as the Levenberg-Marquardt optimization algorithm although these algorithms require much more memory during the training procedure.

4.8 References

- [1] T. Kohonen, "Self-Organization and Associative Memory", Second Edition, Springer-Verlag 1988.
- [2] S. Haykin, "Neural Networks: A Comprehensive Foundation" Mcmillan College Publishing Company, Inc. 1994.
- [3] M. T. Hagan, H. B. Demuth, "Neural Network Design," PWS Publishing Company, 1996.
- [4] A. K. Jain, J. Mao and K. M. Mouiuddin, "Artificial Neural networks: Tutorial", IEEE, Computer, Volume 29, Number 3, March 1996.
- [5] B. Kosko, "Neural Networks and Fuzzy Systems", Prentice-Hall, Inc. 1992.
- [6] J. A. Freemans, D. M. Skapura, "Neural Networks", Addison-Wesley Publishing Company, Inc. 1991.
- [7] Y. H. Pao, 'Adaptive Pattern Recognition and Neural Networks', Addison_wesey Publishing Company, Inc. 1989.
- [8] S. Grossberg, "Neural Networks And Natural Intelligence," The Massachusetts Institute of Technology, 1988.
- [9] M. Morris, "Digital Design," 2nd edition, 1991.

CHAPTER 5

Neural Networks Based Defect Detection in TNDE

5.1 Introduction

For several years, infrared measurement and inspection techniques have been used to inspect and evaluate subsurface defects, thermophysical non-homogeneities of material, coating thickness and hidden structures. Based on thermal wave propagation and attenuation analysis, each thermal non-homogeneity perturbs the propagation of the thermal waves and changes the temperature response on the specimen surface compared to the surrounding sound region. This thermal perturbation is recorded by an infrared detector to provide information for further processing [1], [2], [3].

In active TNDE, thermal stimulation can be done by a pulse (Pulsed Thermography, “PT”) or sinusoidal (Modulated Thermography, “MT”) heating source. In the PT approach, the sample under investigation is heated for a time period varying from μs to s . The duration of the heating pulse depends on thickness and thermophysical properties of the sample.

Usually, the analysis of the transient temperature is done in the time domain. Recently, a frequency analysis of PT based on the Fourier transform has been employed to detect and characterize subsurface defects. This approach is called PPT (Pulsed Phase Thermography) with advantages of both PT and MT approaches [4].

In recent years many researchers have used neural networks to solve complex non-linear real world problems. Neural networks (NN) are potentially powerful, robust and adaptive tools for detecting and classifying targets under changing signature or environmental conditions. They can learn from provided training set and generalize these examples to similar data which are not contained in the training set [5], [6].

Artificial neural networks (ANN) as a TNDE defect detector and classifier have been proposed in the past few years [7], [8], [9], [10], [11], [12]. Multilayer perceptron were employed to detect and characterize defects using phase data extracted from the PPT method [7], [9]. These studies revealed that phase data has limited sensitivity to noise and requires sufficiently high sampling rate with respect to thermal properties of specimens to achieve its complete potential. A comparison of Kohonen and perceptron NNs performances applied to TNDE was made in [8]. This study showed the perceptron NN achieves much better detection result. In [10], two multi-layer neural networks were used to reveal and estimate corrosion severity in aluminum. The networks inputs are temperature vs. time curves and their outputs show defect or non-defect alarm and corresponding estimated depth for processed pixel. The other attempt involves the use of experimental and simulated data combined together to train multi-layer networks with input vectors containing only the maximum contrast and its occurrence time for each pixel, while the output indicates estimated depth and defect or non-defect alarm for each pixel [11], [12].

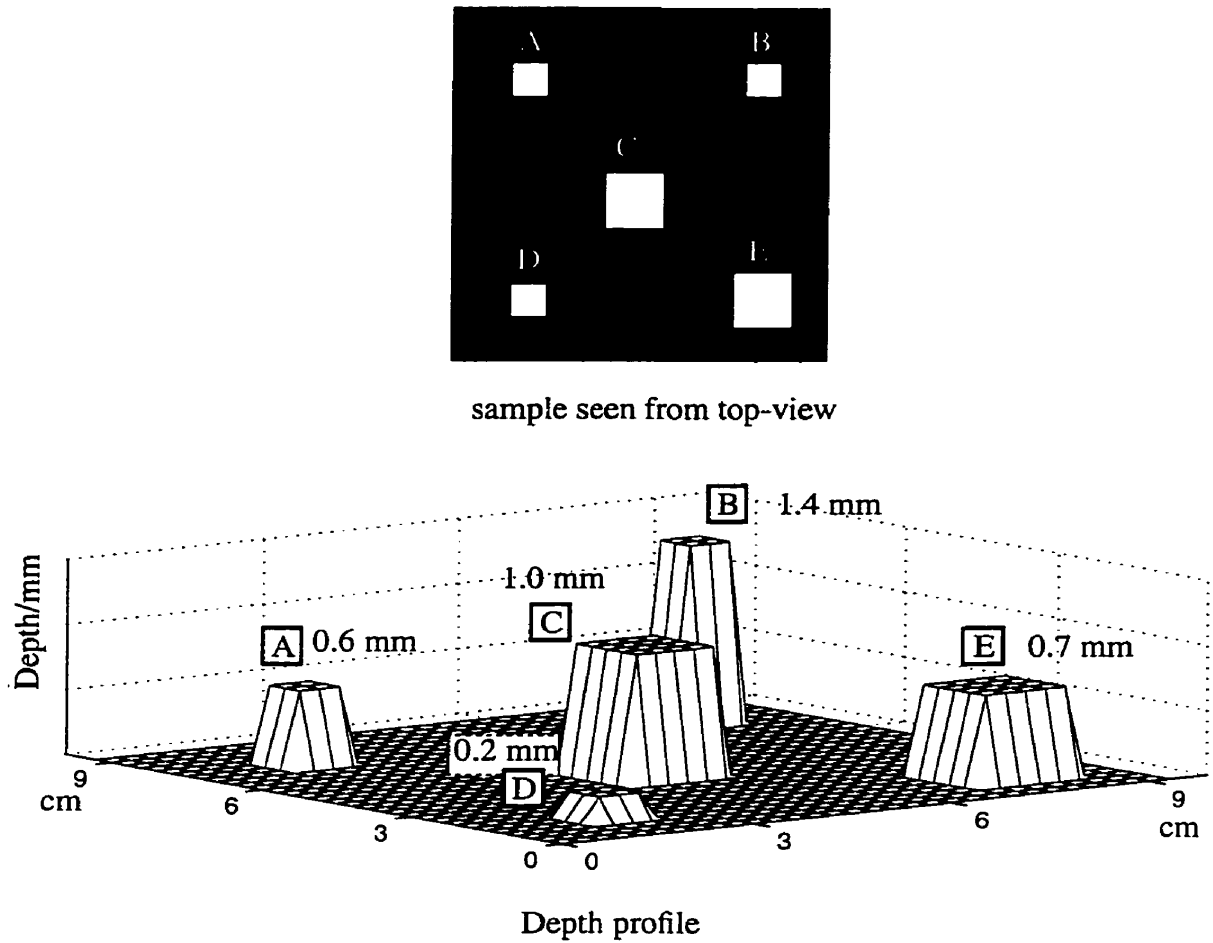
In this chapter, we will investigate the development and use of various NN architectures for defect feature extraction and detection for non-homogeneous material such as CFRP in TNDE. We intend to use only simulated data during the training phase. This allows to train NNs with non-redundant and representative data on one hand and study noise effect on NN performances on the other hand.

5.2 Thermal Data

In chapter 2, we discussed the fundamentals of heat transfer, numerical and analytical solution of direct problem in TNDE, with and without subsurface delamination defects. Massively parallel implementation of numerical modeling on a MasPar was given in chapter 3. Now, in this chapter, our numerical modeling is used to produce the necessary synthetic thermal data containing different output signatures of defects buried in the samples. The features of the generated data is also studied.

Let us consider a CFRP sample block with dimension of $2\text{ mm} \times 9.6\text{ mm} \times 9.6\text{ mm}$ (Figure 2.10). This sample contains five air delaminations of different sizes positioned at depths 0.2, 0.6, 0.7, 1.0 and 1.4 mm as shown in Figure 5.1.

The surface temperature of sample in Figure 5.1 is computed with a heat pulse of half a second duration, following which the temperature is computed for five seconds. The temperature vs. time curves corresponding to all sample surface pixels (32×32), sound area, defect area and central pixels for all five delamination-type defects along with one randomly chosen pixel located in the sound area are respectively shown in Figure 5.2(a), (b), (c), and (d).



Five air delamination defects
(A, B, C, D, E)

Depth and Size as:

A: depth 0.6 mm, size 0.9 cm x 0.9 cm

B: depth 1.4 mm, size 0.9 cm x 0.9 cm

C: depth 1.0 mm, size 1.5 cm x 1.5 cm

D: depth 0.2 mm, size 0.9 cm x 0.9 cm

E: depth 0.7 mm, size 1.5 cm x 1.5 cm

Figure 5.1 An CFRP block sample, which contains five air delaminations of thickness 100 μm , defects at shown depth.

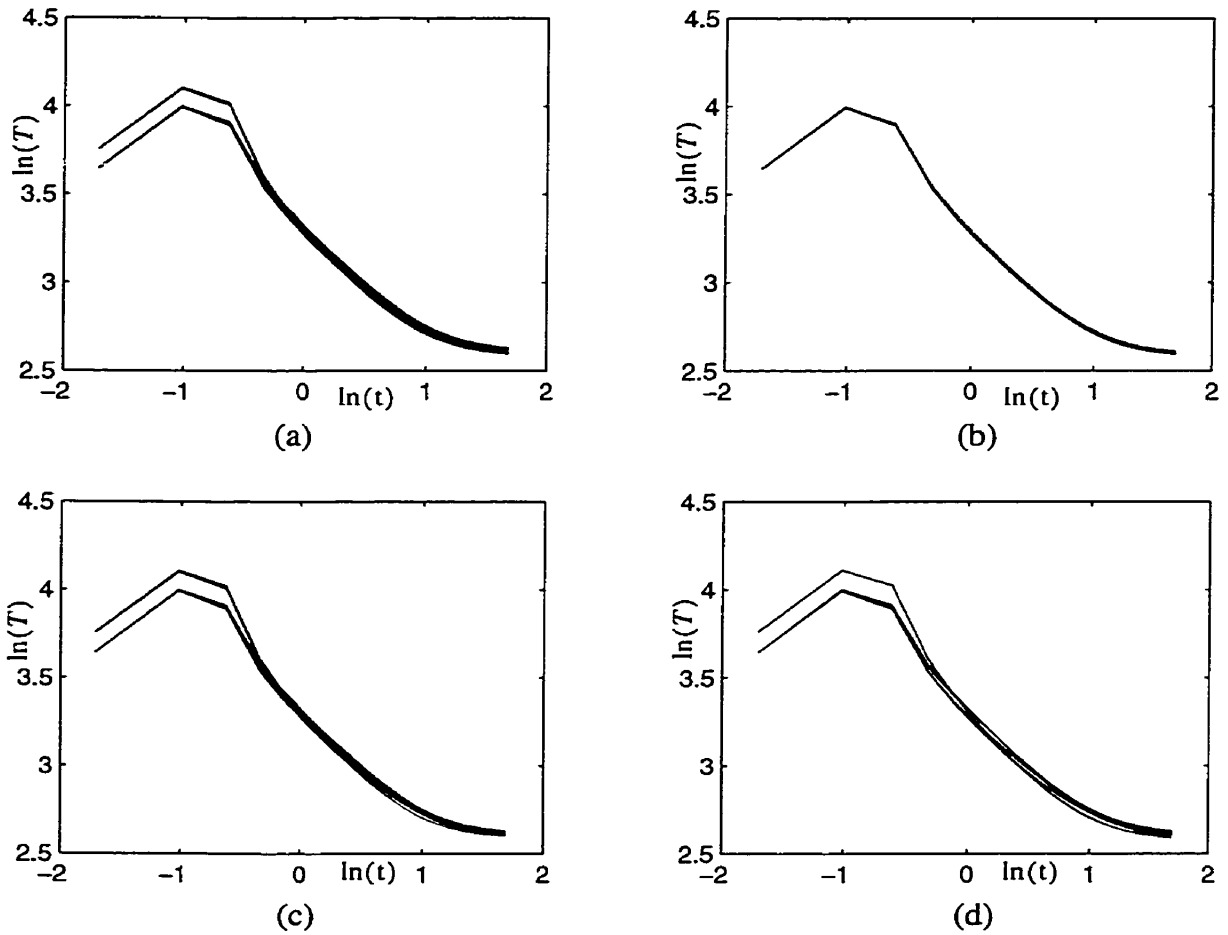


Figure 5.2 Temperature vs. time curves for simulated CFRP sample, (a) all sample surface pixels, (b) sound area, (c) defect areas, (d) central pixels of all five delamination-type defects (red) along with one randomly chosen pixel of sound area (green) temperature curves. Differences are due to different defect depths.

As seen in Figure 5.2(a) to 5.2(d), classifying sound and defect areas in two different classes is not evident in most cases if we consider temperature evolution on the sample surface as input data to the neural network. Figure 5.2 (b) reveals that all pixels corresponding to sound area have approximately equivalent temperature evolution curves. Also, Figure 5.2(c) shows that it is very difficult to classify temperature evolution data to five different classes to define five different depths of inserted defects in sample.

To enhance thermal data difference between sound and defect areas, we can use thermal contrast curve as input. There are four informative parameters which are mostly employed in transient TNDE [1], [13]. The first is the temperature difference over defect which is given by:

$$\Delta T(t) = T_{defect}(t) - T_{sound}(t). \quad (5.1)$$

The “ ΔT -image” obtained from this equation looks like a raw IR image and depends linearly to the absorbed energy. The second contrast parameter can be defined by:

$$C(t) = \frac{T_{defect}(t) - T_{defect}(t=0)}{T_{sound}(t) - T_{sound}(t=0)}. \quad (5.2)$$

Here, $C(t)$ is the thermal contrast, $T_{defect}(t)$ and $T_{defect}(t=0)$ are respectively temperature over defect area at time t and the beginning of the process $t=0$. Temperatures over sound area at time t and $(t=0)$ are respectively $T_{sound}(t)$ and $T_{sound}(t=0)$. A third definition of the thermal contrast is presented as:

$$C^r = \frac{\Delta T}{T_{sound}(t)}. \quad (5.3)$$

where C^r is known as the running contrast, it is less affected by surface optical properties if emissivity and absorptivity parameters are the same for both defect and sound areas. The input heat pulse shape and duration affects weakly the running contrast parameter. Finally, the fourth contrast parameter is named normalized contrast and is given by:

$$C^n = \frac{T_{defect}(t)}{T_{defect}^m(t^m)} - \frac{T_{sound}(t)}{T_{sound}^m(t^m)} \quad (5.4)$$

where $T_{defect}^m(t^m)$ is the maximum temperature for defect area and $T_{sound}^m(t^m)$ is the maximum temperature for sound area. The normalized contrast is independent on both absorptivity variation and heating non-uniformly but it depends on heat pulse shape and duration [14].

Figure 5.3 (a, b, c and d) shows respectively ΔT -image, contrast, running-contrast and normalized contrast curves for the sample of Figure 5.1. The curves with green dash-dotted line are contrast curves over the randomly chosen sound pixel and contrast curves with red line are related to the central pixels of the defects. Comparison of these contrast curves to the absolute temperature curves depicted in Figure 5.2 indicates they can be classified in different classes depending on their pixel thermal properties as defect or non-defect. After having classified pixels into defect and non-defect classes, then the pixels corresponding to defects can also be classified into different classes with respect to their depths. It should be mentioned that in this sample, the contrast curves corresponding to the defects located at depths 1.8 mm or deeper are approximately the same as the contrast curves for sound pixels. In these cases, we can not classify those pixels as a non-defect pixel. This means there are limits for maximum depth estimation which depends on our setup parameters (heat source power, pulse duration), defect thermal properties or defect size and specimen thermal parameters. For instance in this case the parallel to the fiber thermal conductivity is 8.75 times greater than the perpendicular thermal conductivity meaning only relatively close to the surface defect can be detected by TNDE (that is about $1.8\text{-}2 \text{ mm}$ at most in the case of CFRP specimens for which $k_{||}$ is about 10 times greater than k_{\perp} to the fiber).

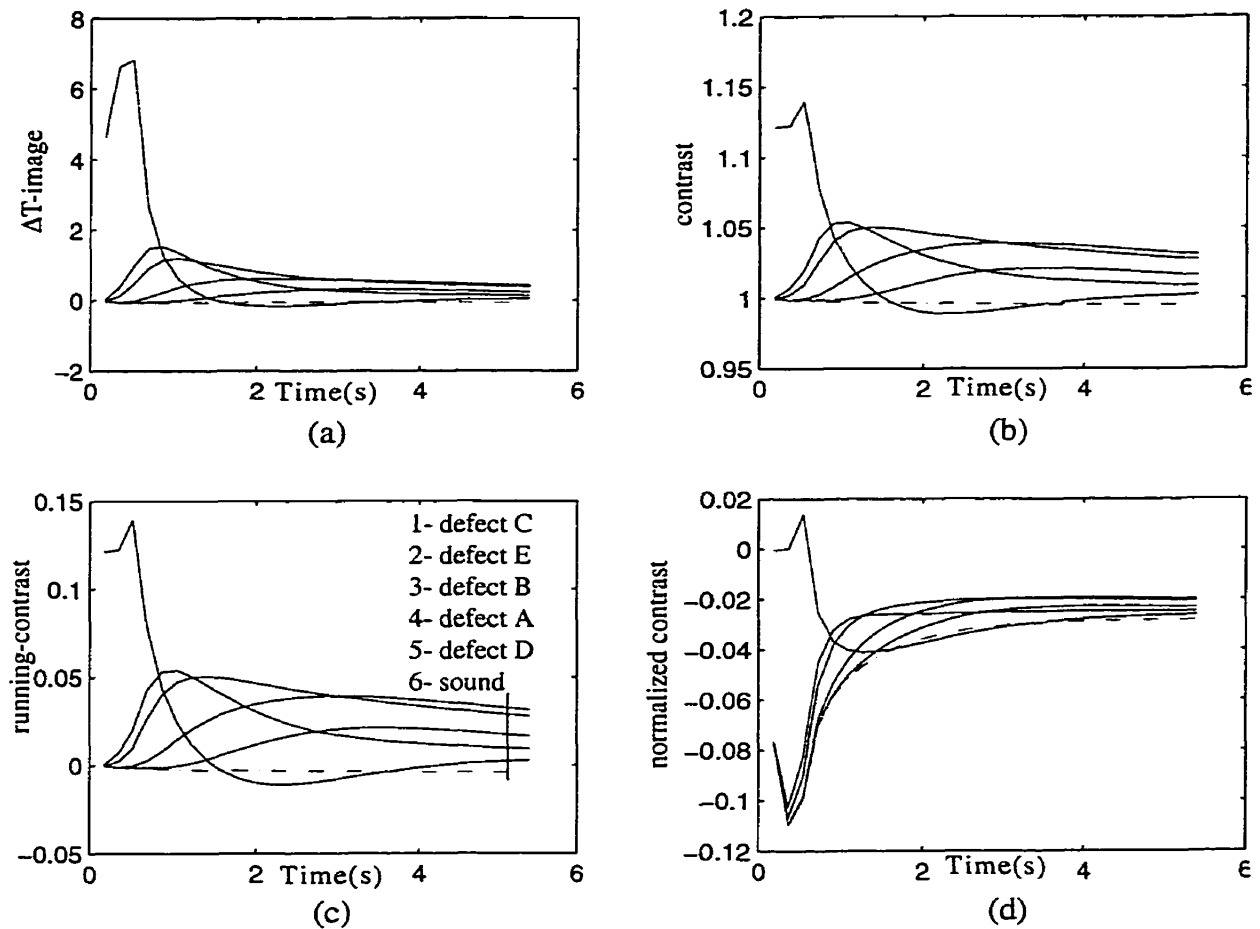


Figure 5.3 Temperature contrast vs. time curves for one randomly chosen sound pixel (green) and central pixels of five air defects (red) which are located in the CFRP block at depth 0.2, 0.6, 0.7, 1.0 and 1.4 mm (Figure 5.1). (a) ΔT -image, (b) contrast, (c) running-contrast and (d) normalized contrast.

5.3 Defect Detector Network

Neural networks can be considered as parallel processors. They are composed of a large number of highly interconnected processing elements (neurons) working together to solve specific problems. In this study we are only interested in multi-layer perceptron networks (MLP) which are supervised networks (chapter 4). The MLP network is a nonparametric technique for performing a wide variety of detection and estimation tasks.

The MLP network can be trained using the back propagation algorithm which has been probably the most used learning algorithms in the recent years. This algorithm is applied to a wide variety of real problems [15].

The most important problems that must be solved when a back-propagation NN is used are the determination of the number of neurons in each layer, the connections and their weights. In feedforward networks (MLP), connection weights are initialized to random values and then adjusted during training procedure to satisfy a specific error goal. We have examined many different feedforward network architecture as defect detector. This study indicated there is a correlation between the maximum defect depth at which the contrast over a defect area is different from contrast over a sound area and the optimum number of units in the hidden layers.

After different tests, we settled for a $30 \times 15 \times 1$ defect detector network whose architecture is shown in Figure 5.4. This network was trained using 130 input-output pair vectors extracted from the samples which contained air delamination defects in different depth and configurations, 105 input vectors were running-contrast curves over defects area and 25 were over sound area. Figure 5.5 illustrates maximal points of input curves and desired output which is '0' for non-defect pixel and '1' for defect pixel.

The trained network was provided with nine other simulated samples containing five air delamination defects as the same shape of defects which were used during the training procedure. As shown in Figure 5.6, the deepest defect is located at depth 1.4 mm and the shallowest defect is located at depth 0.1 mm . The network output results for these test samples are shown in Figure 5.7 and Figure 5.8. Figure 5.7 shows that the detector network detected all the defects in nine simulated samples. The white and black pixels in this figure define respectively defect and sound areas. Figure 5.7 shows the error pixels (white pixels) which are 3.2% of the total pixels. This means the network correctly classified 96.8% of the total pixels.

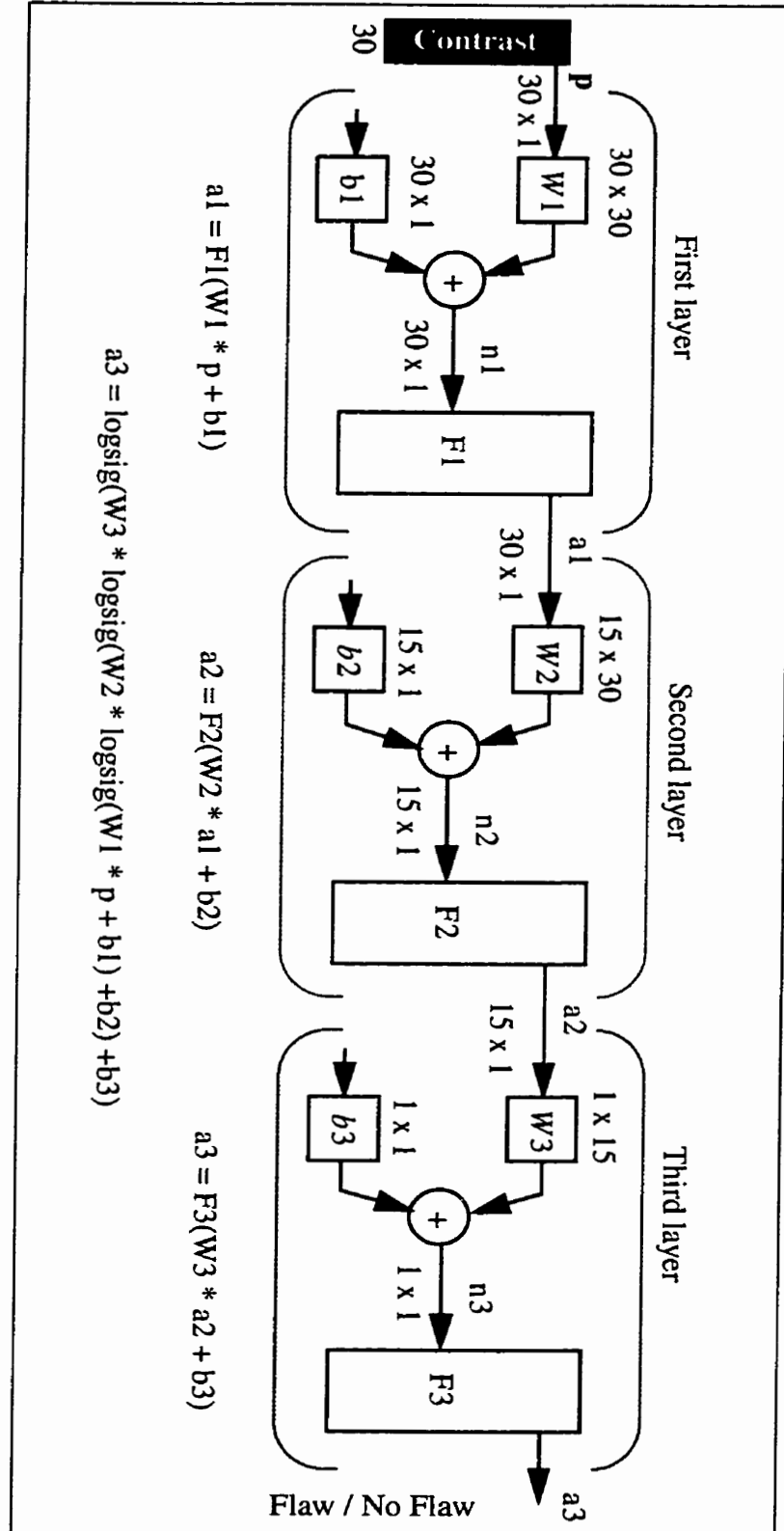


Figure 5.4 A three layer defect detector network architecture.

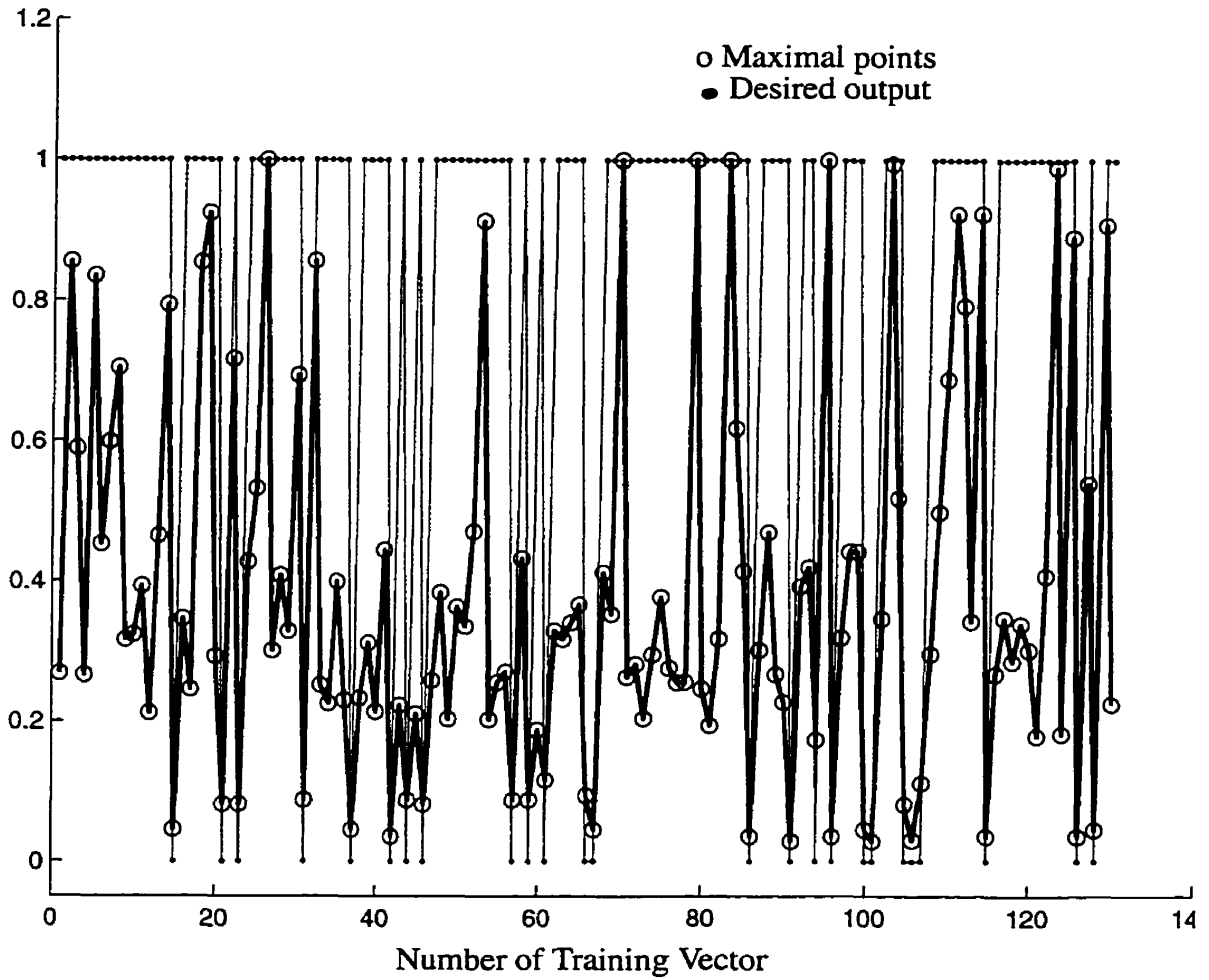


Figure 5.5 The maximal points of thermal contrast curves and corresponding desired outputs.

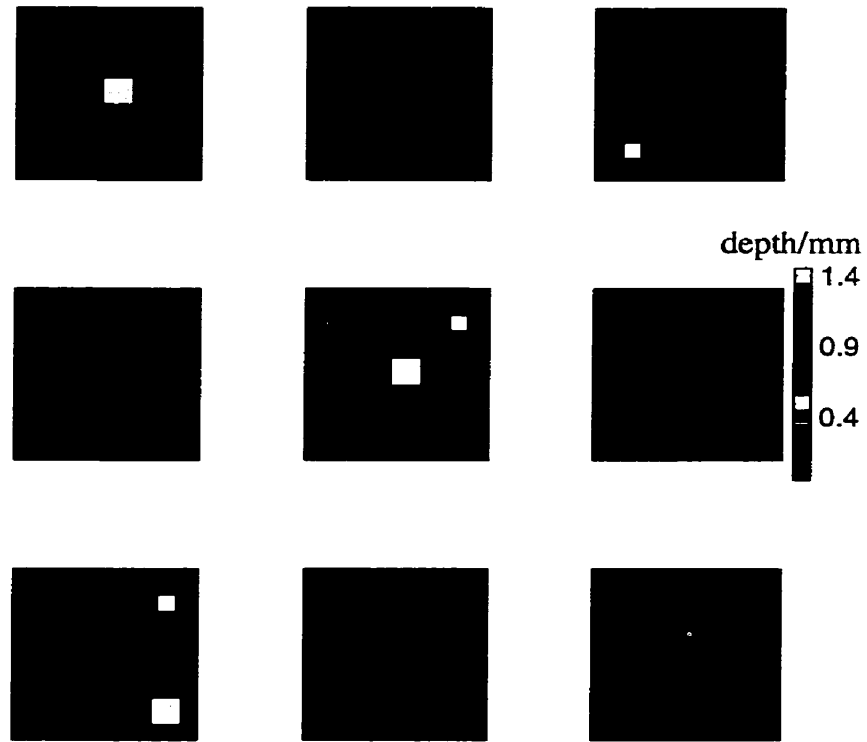


Figure 5.6 The simulated samples depth profile which were deployed to examine defect detector network performance.

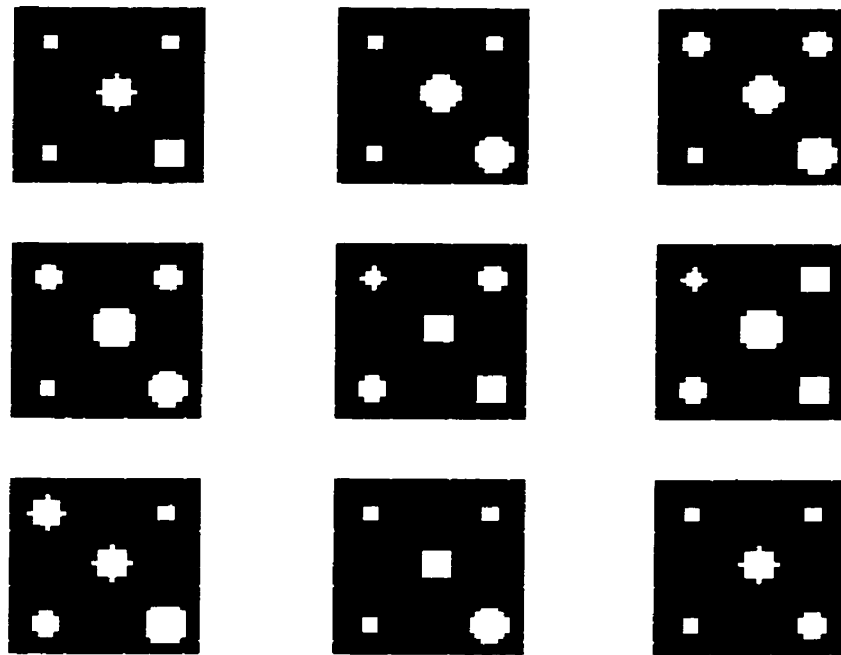


Figure 5.7 Defect detector output images for nine different simulated data sets, white pixels represent defect areas.

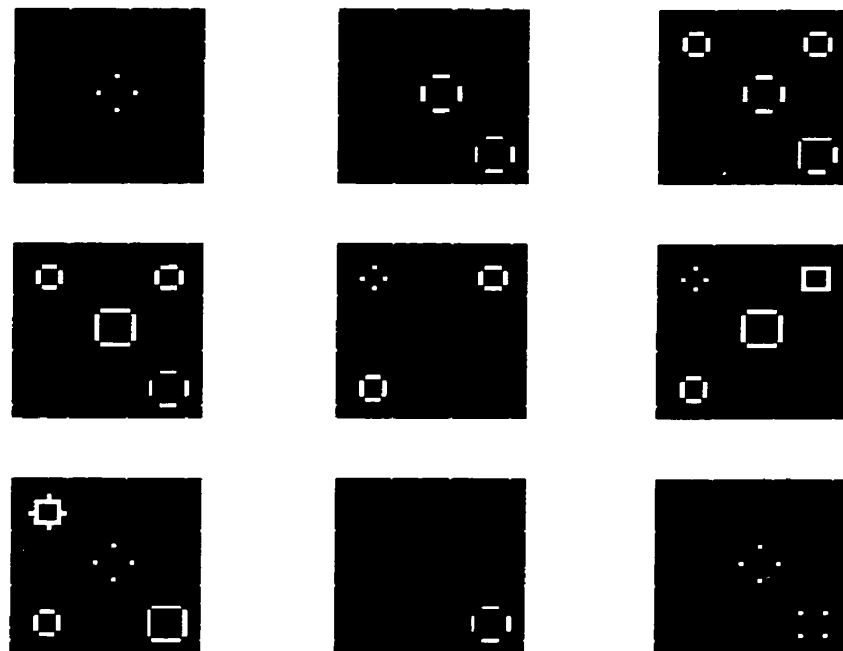
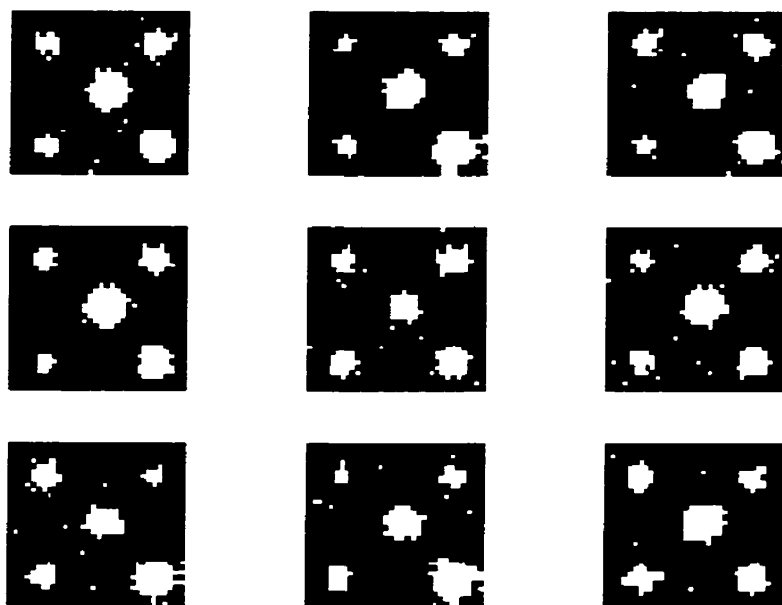


Figure 5.8 Error images for the above defect detector output results. White pixels shows pixels incorrectly detected as defect or non-defect pixels.

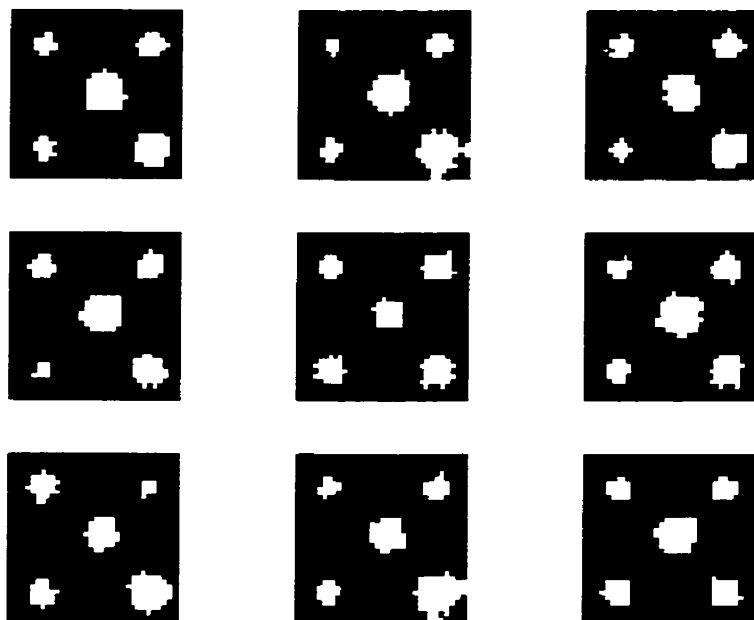
Table 5.1 Cincinnati Electronics IRC-160 noise standard deviation

$T(^{\circ}\text{C})$	$\sigma_T(^{\circ}\text{C})$
9.2	0.054
11.6	0.050
17.6	0.045
23.0	0.039
27.6	0.033
31.0	0.029
34.1	0.027
36.4	0.025
38.2	0.023
39.8	0.022
41.5	0.020
42.8	0.019
44.2	0.019
45.3	0.019
46.2	0.019
50.5	0.021

The second experiment involved the use of additive noisy data to examine the proposed network performance. The task was similar to the one above but noisy data was generated based on white Gaussian noise with different temperature noise standard deviations $\sigma_T(^{\circ}\text{C})$ as input test signals. The temperature noise standard deviations at different temperatures for the available Cincinnati Electronics IRC-160 infrared camera are given in Table 5.1 [16]. As seen in Table 5.1 the Cincinnati Electronics IRC-160 noise standard deviation decreases when the specimens temperature increases. Also, we know that in active thermography the sample is heated for a short period of time by the heating source. Consequently, the sample surface temperature will be above the ambient temperature (about 25.0°C) for most of our applications. Therefore, we can suppose the Cincinnati Electronics IRC-160 noise standard deviation in the worse case for our applications is $\sigma_T(^{\circ}\text{C}) = 0.039$ or smaller. Despite of this, the previous experiment data sets were contaminated with white Gaussian noise with noise standard deviation $\sigma_T(^{\circ}\text{C}) = 0.054$ and also, in a second trial with $\sigma_T(^{\circ}\text{C}) = 0.039$. The detector network output results for these additive noisy input data sets are respectively presented in Figure 5.9 (a) and (b). In this experiment for both cases the defect detector is able to reveal all defects contained in the sample. However the network output results are degraded by the presence of white Gaussian noise in the input data sets. For contaminated



(a)

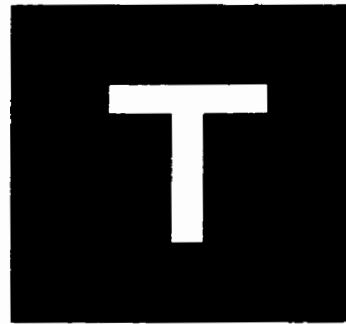


(b)

Figure 5.9 Defect detector output images for the simulated data sets which are contaminated with a white Gaussian noise (a) $\sigma = 0.054$ and (b) $\sigma = 0.039$.

input data sets with noise of $\sigma_T(^{\circ}\text{C}) = 0.054$, the overall output results error is *11.2%* and with the noise with $\sigma_T(^{\circ}\text{C}) = 0.039$, it is *6.3%*.

In order to investigate the lateral extension of defects on the output results, the network was provided with the temperature contrast vectors extracted from the surface temperature evolution of the sample shown in Figure 5.10. The defects in previous tests are enough distanced from each other and for each defect, all pixels are laid at same depth with regular defect shapes. Therefore, temperature perturbations due to the defects are symmetrical in defect areas and around them. In next test, the sample contains a T-shape air defect (Figure 5.10 (a)) in which the pixels depth gradually changes (Figure 5.10 (b)). This type of defect requires a three dimensional heat transfer modeling such as our 3-D thermal simulation implemented on the Maspar computer.



Sample seen from top-view

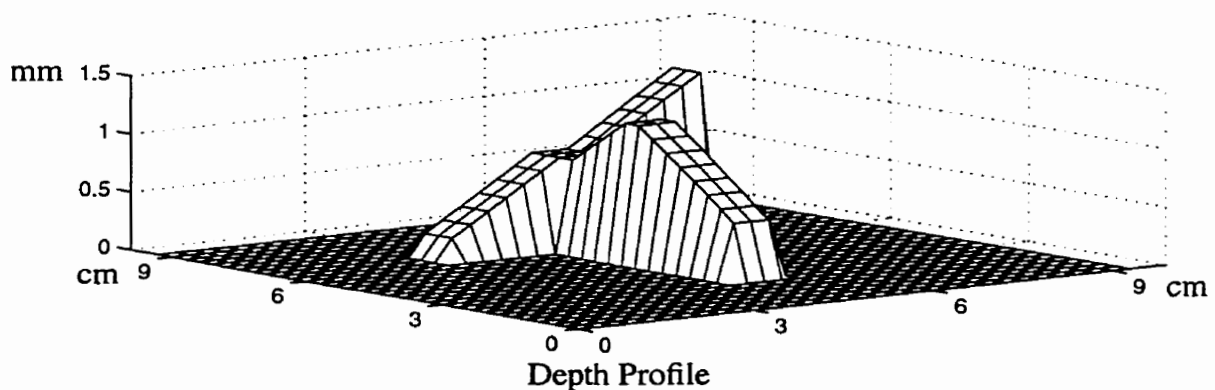


Figure 5.10 A CFRP sample containing a T-shape air defect with shown depth profile.

In this case the network correctly classified about 95% of the image pixels and the T-shape defect as well as shown in Figure 5.11 (a). The network error image is shown in Figure 5.11 (b). This confirms that the lateral defect effect is more significant in shallow defect areas (see arrows).



Figure 5.11 The detector network output result: a) White area detected as defect; b) the error pixels (white) which are incorrectly classified as defect or sound pixels.

5.4 Experimental Results for Detector Network

The network classification ability is now evaluated in this section using real thermal data sets. In our laboratory, all the available CFRP samples contained TeflonTM delamination defects. Therefore, we have to provide simulated samples containing TeflonTM delamination defects in order to train the detector network.

In this simulation procedure, we suppose the samples surface are submitted to a heat source with power of about $100 \text{ KW} / \text{m}^2$ for a 0.5 second period of time. Similarly to the previous study, each sample contains five TeflonTM defects with different size at different depths. One of the sample is depicted in Figure 5.12.

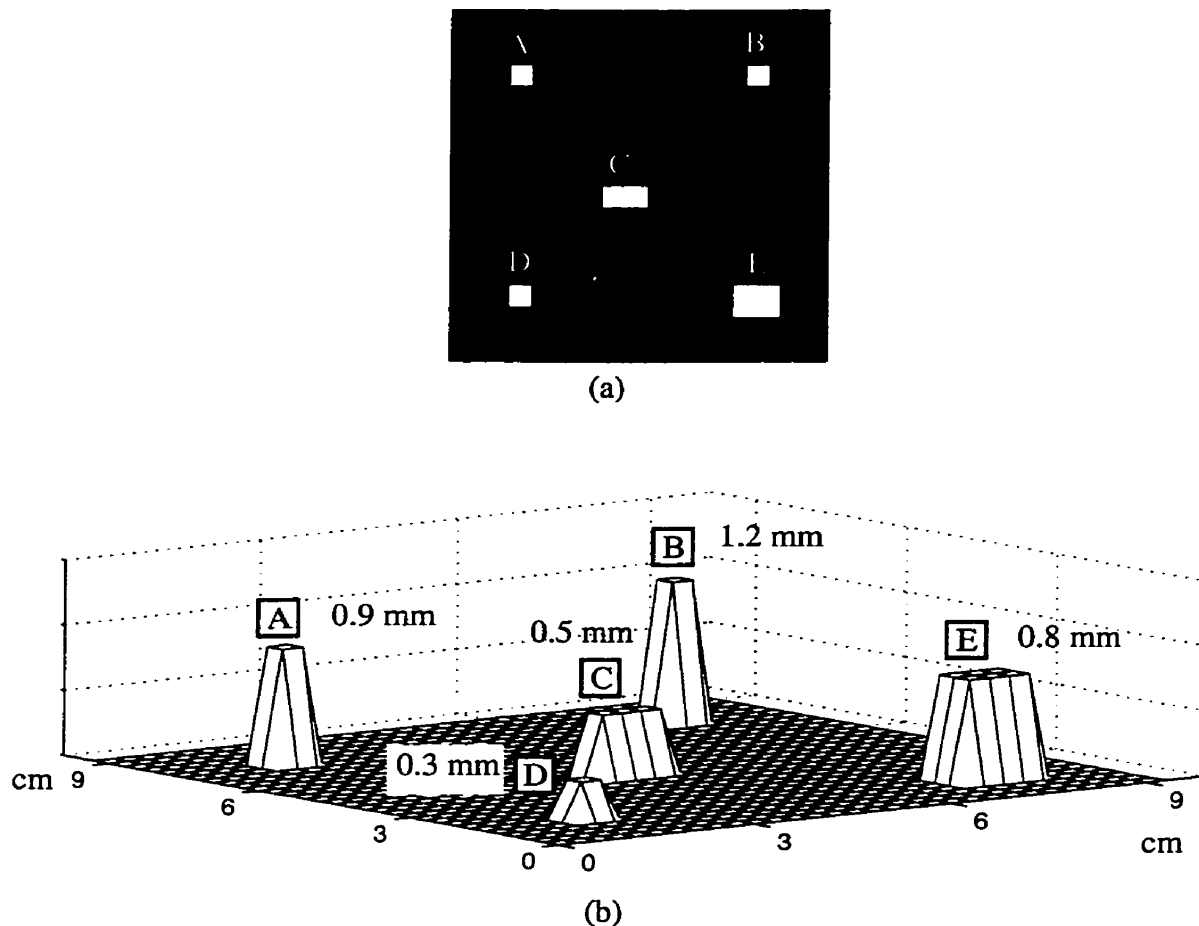


Figure 5.12 One of the simulated CFRP sample containing TeflonTM defects. It is used in the training procedure for experimental results: a) top-view of the sample; b) the sample depth profile.

The simulated contrast data in this study shows that the contrast signal over a TeflonTM defect with dimension $0.6 \text{ mm} \times 0.6 \text{ mm} \times 100 \mu\text{m}$ is considerably different from sound area if its depth is smaller than 1.1 mm such as for defects A, C, D and E. The contrast signal is the same as sound pixel if the defect is located deeper than 1.1 mm like defect B. This is due to low thermal conductivity perpendicular to the fiber as said before. The central pixel contrast signals for these defects are shown in Figure 5.13. The running contrast signals corresponding to defects A, C, D and E can be classified into different classes comparing to the sound area contrast signal. However the contrast signal corresponding to defect B will be classified to the same class as the sound area (we intentionally added 0.005

as offset to this contrast signal just for being distinguishable from the sound pixel contrast signal (the dash-doted curve in Figure 5.13)).

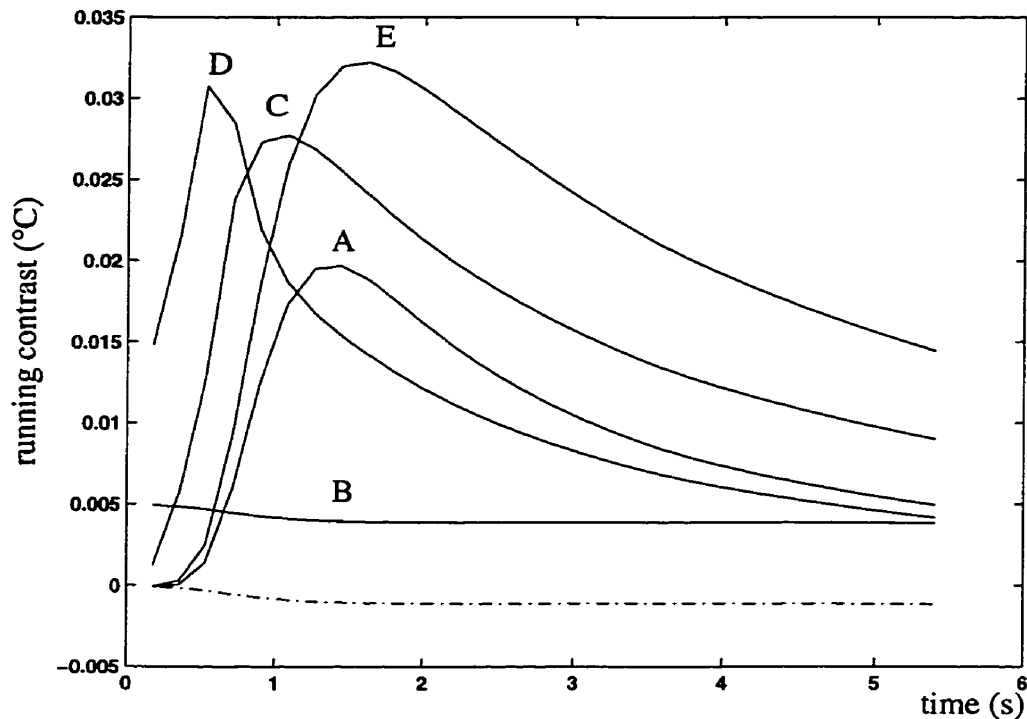


Figure 5.13 The running contrast signal over TeflonTM defects A, B, C, D, E and sound area (dash-doted curve) for the sample shown in Figure 5.11. The defects depth are respectively 0.9, 1.2, 0.5, 0.3, and 0.8 mm.

Moreover for each defect in which all the pixels laid in the same layer, the number of representative pixels depend on the defect size. The simulated data for CFRP sample containing TeflonTM defect shows that the temperature contrast amplitude for each defect pixel is related to the pixel distance from the defect center due to the lateral thermal diffusion [17]. The maximum contrast occurs at the central pixel while the minimum contrast belongs to the farthest pixel from the defect center. For example, Figure 5.14 shows contrast curves of all 12 pixels in defect E region. Although, the amplitude of these contrast signals vary over pixels of the defect laid at fixed depth from sample surface, the time of the maximum amplitude is grossly the same for all of them. Therefore, it is sufficient to define four representative pixels among these 12 pixels to correctly represent defect E to the network during the training procedure.

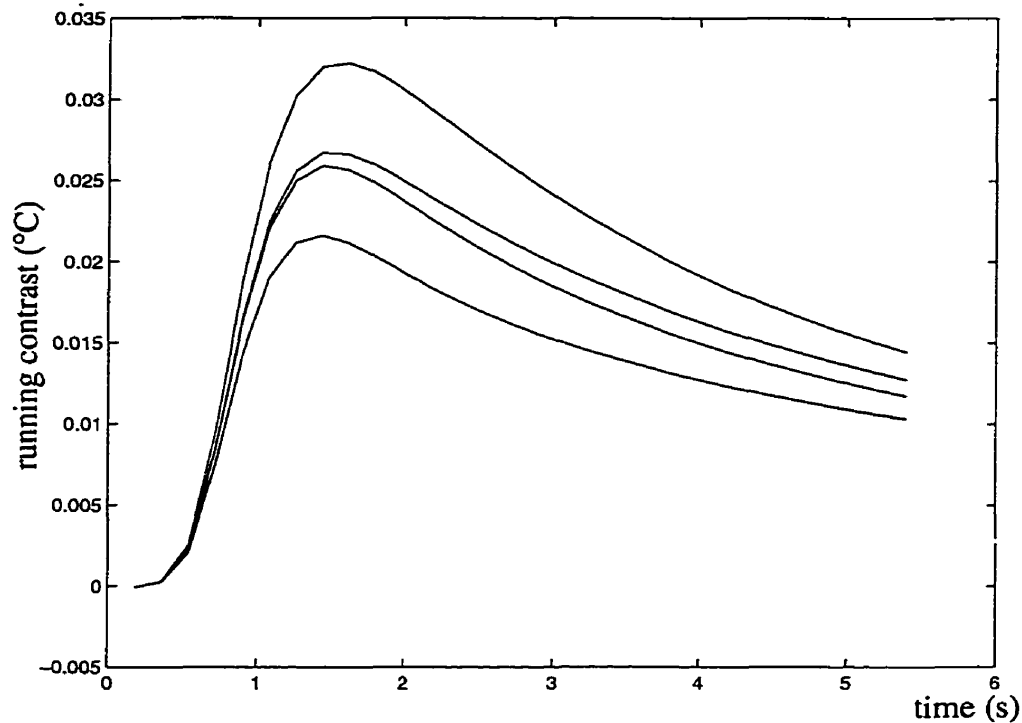
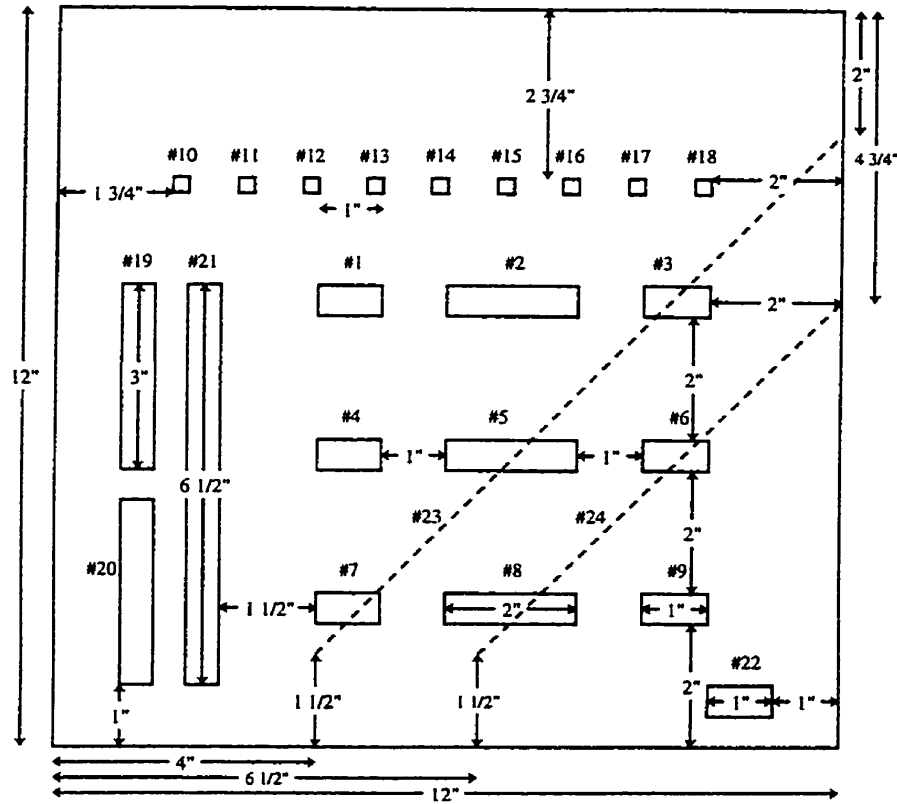


Figure 5.14 The running contrast signal curves for all defect E pixels which shows they can be classified in four categories.

Considering the above mentioned criteria, the defect detection network was trained with 136 normalized contrast vectors chosen from both sound and defective areas. After training, two CFRP samples were used in the testing phase. The geometry of the first sample which contains various inserted rectangular TeflonTM defects with thickness $50 \mu m$ at different depths is shown in Figure 5.15. Many experiments were conducted to record the sequential temperature profiles for different areas of this CFRP sample. In these experiments, first, the sample is heated by two flash lamps with a total power of $80 kW$ and then the surface temperature profiles are recorded for 5 seconds. Unfortunately, this procedure did not revealed all of the known buried defects. This is mainly due to the highly anisotropic nature of CFRP non-uniform heating, flash heating (the heating period is too short to penetrate deep within the specimen), noise and other errors in the experimental procedure.

CFRP sample drawing



all TEFLON inserts - smallest thickness possible (50µm ok)

INSERTS	LAYERS	DEPTH
#1,10	1-2	0.006"
#2,11	3-4	0.018"
#3,12	5-6	0.030"
#4,13	7-8	0.042"
#5,14,19,20,21,22	9-10	0.054"
#6,15	11-12	0.066"
#7,16	13-14	0.078"
#8,17	15-16	0.090"
#9,18	17-18	0.102"

SPECIAL DEFECTS

#23 a cut in layers 9 and 10 starting on the upper-right edge and ending somewhere after insert #7 far from the lower edge. The cut should cross inserts #3, #5, #7.

#24 a cut in layers 11 and 12 starting on the right edge and ending somewhere after insert #8 far from the lower edge. The cut should cross inserts #6, #8.

Figure 5.15 The CFRP sample layout which is used to test the experimental performance of the detector network (sample courtesy of ITEF, CNR, Padova, Italy).

Nevertheless useful data was obtained from these experiments. For defect areas #1 (depth = 0.15 mm) and #2 (depth = 0.46 mm) the recorded infrared data was filtered both in time and spacial domains. Next the running contrast vector was given as input to the network. The maximum contrast image and detector network output results for this experiment are shown in Figure 5.16. In the maximum contrast image (Figure 5.16 (a)), we can observe only defect #2 with ambiguity on its border and also noise all over the image. It seems that most part of this noise is due to the non-homogenous thermal properties of the CFRP sample that can not be reduced or completely removed by conventional data processing methods. The detector network result for these contrast input vectors, supposing that the reference pixel temperature (sound pixel) is the average of the whole sample temperature is given in Figure 5.16 (b). As seen in this figure, the network is able to reveal both defects #1 and #2. Figure 5.16 (c) shows the network output image when we choose another pixel in the left-up corner area as reference pixel. In this figure false alarm pixels are significantly reduced. From these two binary images we obtain the third binary image in which both defects are more clearly detected (Figure 5.16 (d)). Further erosion and dilatation processing could help cleaning up the resulting image, this is however not the goal of the present work[19].

The second test was done on another CFRP sample which contains two circular TeflonTM defects with 10 mm diameter at depth 2 and 3 mm. In this experience the sample was also heated by the flash heating source and the surface temperature was recorded for 5 second. The maximum contrast image is shown in Figure 5.17 (a). In this image one can roughly detect one of the defects while non-uniform heating is evident all over the sample. Now if we suppose the average contrast signal, as reference contrast signal then the detector network output obtained is the image represented in Figure 5.17 (b). Although, false alarm pixels are seen all over the network output image, both defects are well detected. Moreover, in this case, if we choose another pixel as sound pixel we obtain a different result such as shown in Figure 5.17 (c) in which just one of the two defects is revealed but with false alarm pixels significantly reduced.

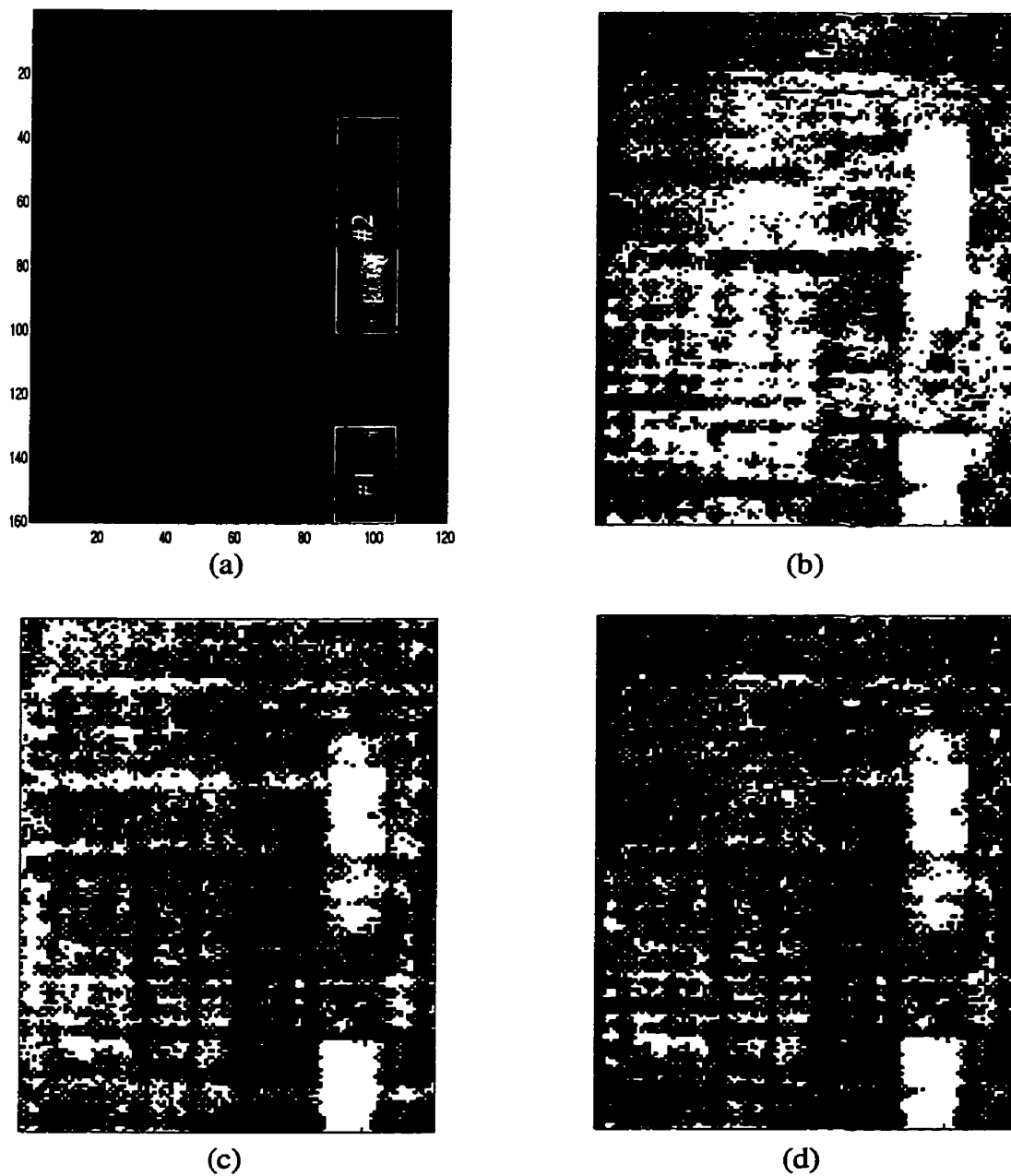


Figure 5.16 The detector network output results and maximum contrast images over defects #1 and #2. (a) maximum contrast image; (b) the network output image supposing average contrast as reference contrast; (c) the network output image supposing one of the upper-left pixels as sound pixel; (d) logical (AND) combination of images (b) and (c).

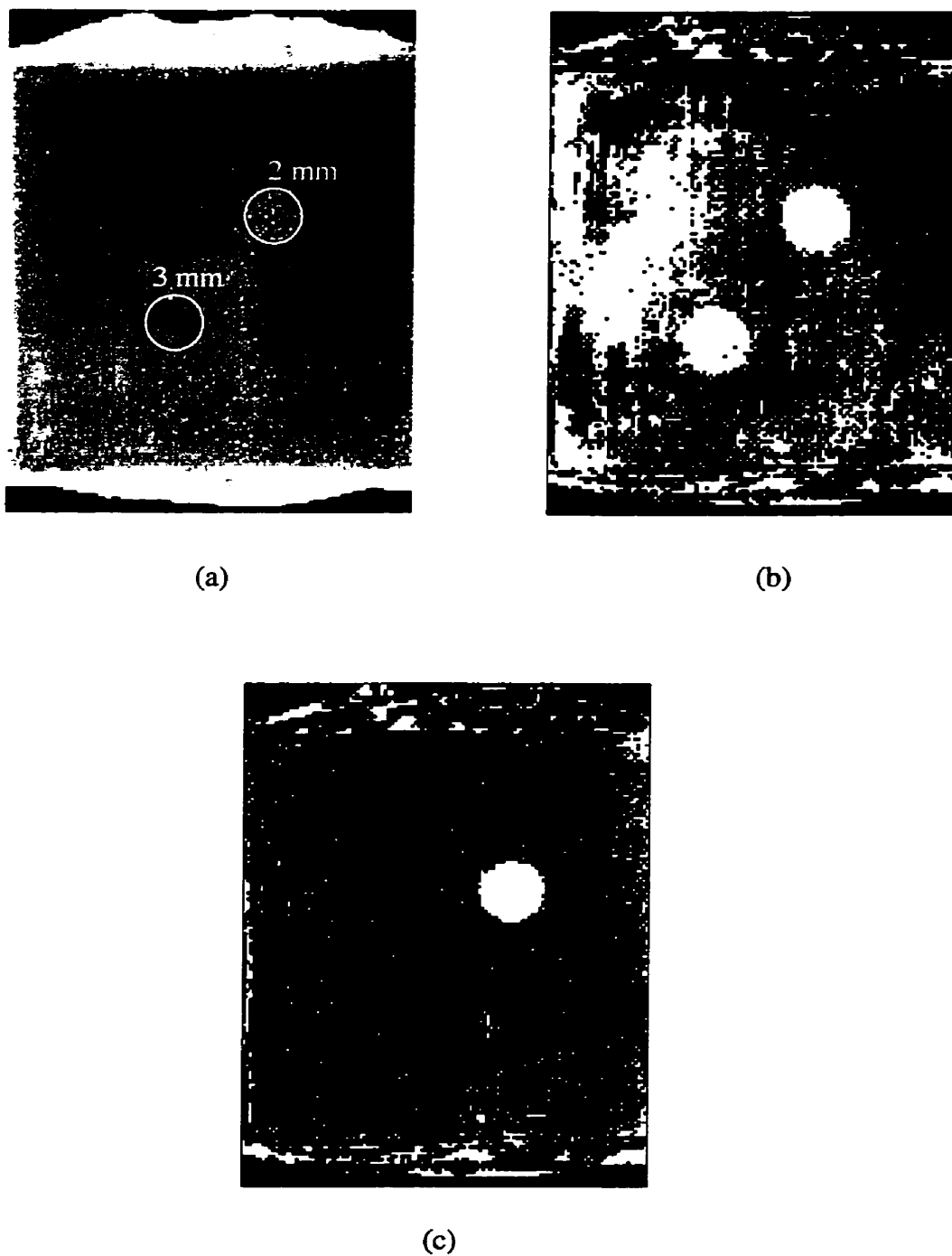


Figure 5.17 The detector network output results and maximum contrast images for the CFRP sample containing two circular TeflonTM defects with 10mm diameter at depth 2 and 3 mm. (a) maximum contrast image; (b) the network output image supposing average contrast as reference contrast; (c) the network output image supposing one of the upper-left pixels as sound pixel.

5.5 Defect Depth Estimation Network

Extraction of the subsurface defect properties such as depth, thermal resistivity and size is called inverse problem in TNDE. Many research works have been conducted to solve the inverse problem in TNDE in recent years. Analytical solution for some simple geometries can be derived by using Green Functions but for most practical cases, such a solution becomes more complex or impossible [2], [18].

As said before artificial neural networks (ANN) are modern alternative to classical data analysis methods and they have been employed to solve real complex problems in many applications. In this section, a depth estimator network is trained on mathematical modeling data generated to simulate an experiment such as the specimen of Figure 5.1. The simulated CFRP samples contain air gaps with $100\ \mu\text{m}$ thickness as defects at different depths. The simulated data study shows that an air gap defect can produce considerable contrast signal on the sample surface, if we restrict ourselves to stimulated conditions proposed in section 5.4 (that is to detect defects up to depth $1.5\ \text{mm}$). The estimator network with 20 input, 15 hidden and 15 output neurons was provided with about 140 input/output vectors as training set.

The input vectors for the depth estimator network are contrast vectors as for the defect detector network but now the output vectors are defined as pixel depth. If the pixel processed belongs to the sound area the output vector value will be zero. Otherwise if it is a defect pixel with specific depth then the output vector value should correspond to the defect pixel depth (expressed in mm).

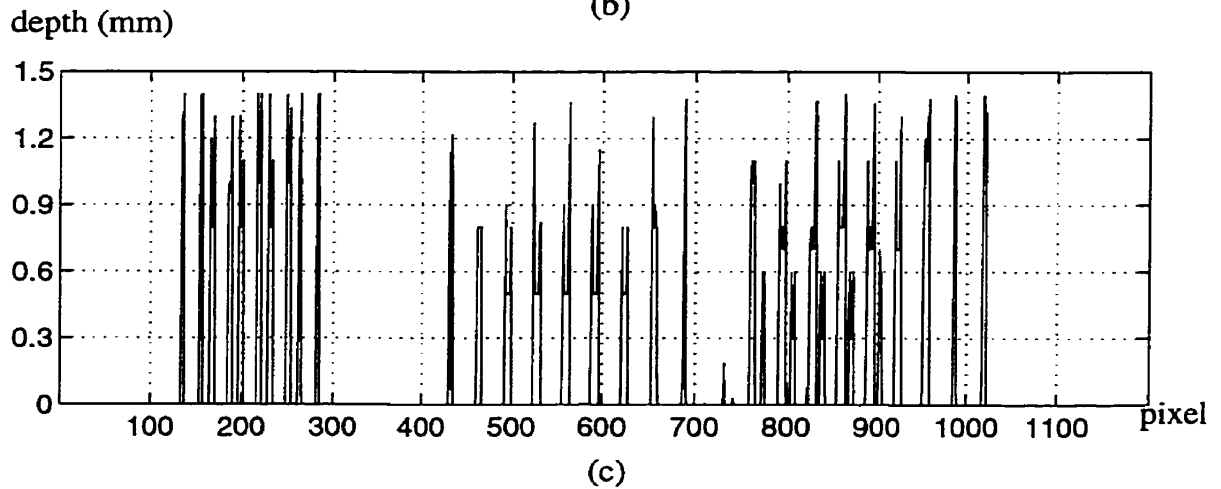
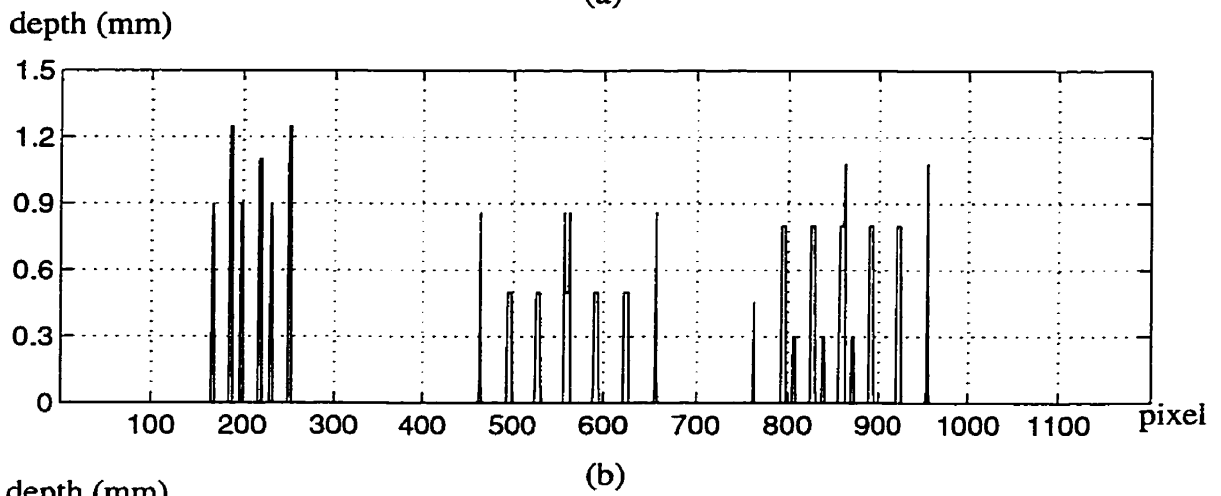
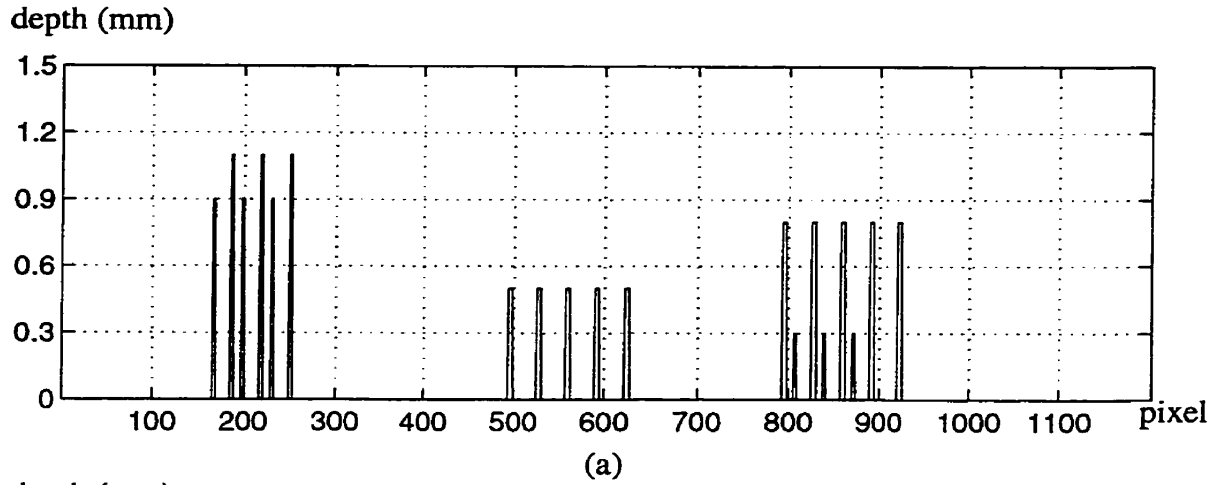


Figure 5.18 The original and estimated defect depth profile for a sample which was used during training procedure: (a) original depth; (b) estimated depth for input data without noise; (c) estimated depth for contaminated input data with a Gaussian noise ($\sigma = 0.033$ and $\eta = 0$).

The estimator network performance is also tested by both simulated and experimental data. The first data set is obtained from the same sample which was used during training procedure. The contained defects have respectively been located at depth $1.1, 0.9, 0.5, 0.8,$ and 0.3 mm. The original and estimated depth profiles pixel by pixel are shown in Figure 5.18. Figure 5.18(b) shows the network response to input contrast data without additive noise while Figure 5.18(c) depicts the estimated depth profile for contaminated input data with a Gaussian noise ($\sigma = 0.033$ and $\eta = 0$). Comparing these results with the original depth profiles, we find out that the network can precisely estimate all defect depths. The estimated defect depths are $1.2, 0.9, 0.5, 0.8$ and 0.3 mm. The additive noise increases the error pixels and in some case modifies the estimated depth. This can be seen in Figure 5.19.

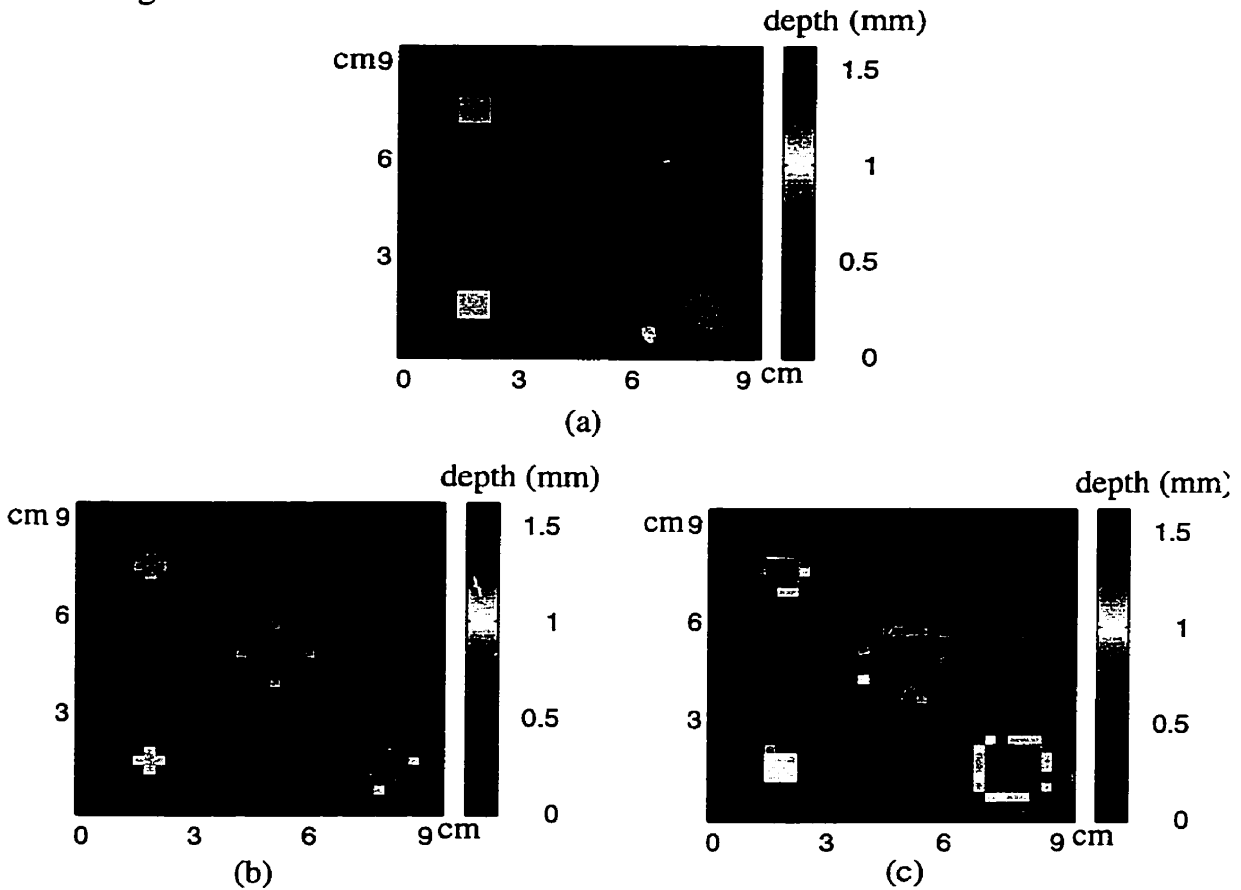


Figure 5.19 The original and estimated depth images for a sample which was used during the training procedure: (a) original depth; (b) estimated depth for input data without noise; (c) estimated depth for contaminated input data with a Gaussian noise ($\sigma = 0.033$ and $\eta = 0$).

We tested another data set which was not used in the training phase. This sample contained the same type of defects as the previous sample but with depths of 0.1 , 0.4 , 1.2 , 1.4 , and 0.5 mm. The estimator network detected four out of five defects and estimated their depth appropriately (Figure 5.20 (c)). Despite of having an high amplitude contrast data, one of the defects which is located at depth 0.1 mm was not detected by the network. This can be due to the training data set which did not provide contrast signal for such a close to the surface defect.

We also examined the estimator network performance with a simulated data set extracted from the sample which contains a T-shape defect as shown in Figure 5.10. The depth is gradually changed row per row or column per column as seen in Figure 5.21 (a). Although, such kind of defects was not present in the training set, the network was able to estimate accurately the depth of the pixels. The network output is depicted in Figure 5.21 (b). This figure shows that most of error pixels have estimated depths greater than their neighbor defect pixels depth. To show the estimated depth accuracy, we represented the depth profile by removing all of the error pixels in Figure 5.21 (c). This figure shows that the estimated depth profile is quite exact as compared with the sample profile in Figure 5.21 (a).

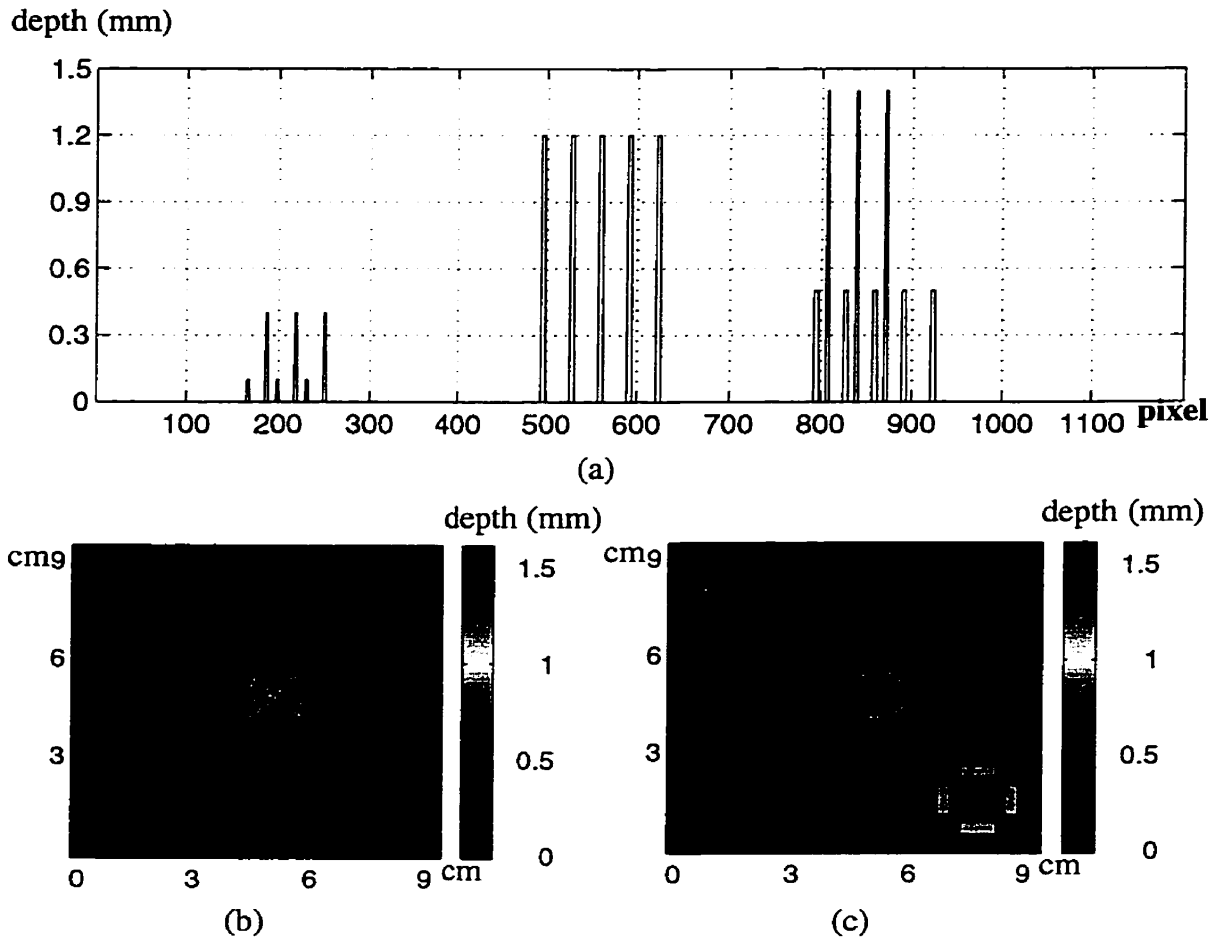


Figure 5.20 The estimator network response to a data set which has not been used during training phase: (a) and; (b) original and; (c) estimated depth profile.

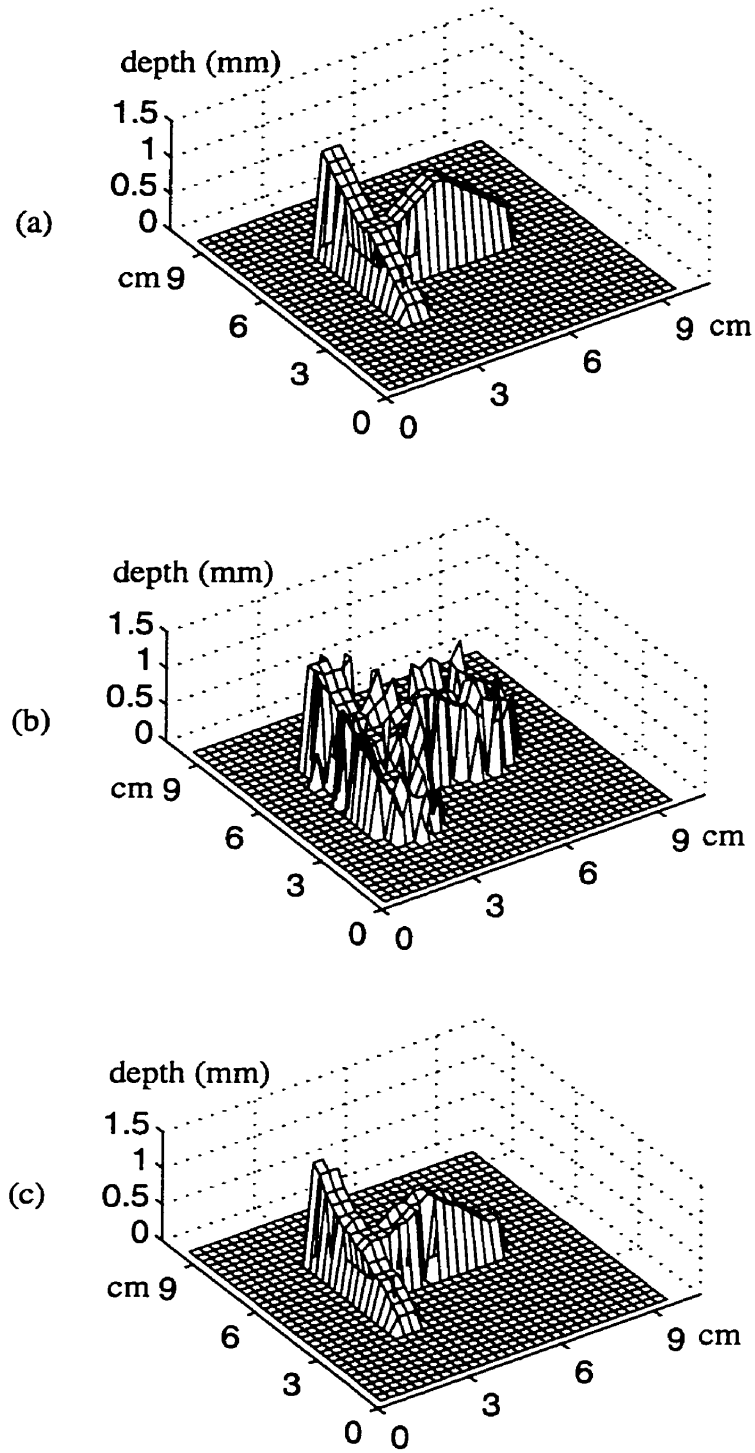


Figure 5.21 Depth profiles of a CFRP sample which contains a T-shape air defect: (a) the modeled sample depth profile; (b) estimated depth profile; (c) the estimated depth profile with error pixels removed from the plot.

5.6 Experimental Results for Estimator Network

As mentioned in section 5.4 the available CFRP specimens contain TeflonTM delamination defects such as the one shown in Figure 5.15. Considering simulated results explained in section 5.4, it was said that we can detect and classify defects up to 1.1 mm under the sample surface. If the required accuracy is $100\ \mu\text{m}$ then the depth estimator should be able to classify the input vectors into 11 different classes. One of such a network that we propose as estimator network is built with 15 input, 15 hidden and 4 output neurons. This network is trained with 136 simulated contrast /depth vectors. The selected pixels are the same as those chosen for the detector network training set. After training, we provide the experimental data such as for the sample shown in Figure 5.15 to the estimator network. The network is able to detect and estimate both defect presence and depth. The estimated depth is about 0.3 mm for one and 0.4 mm for the other defect as shown in Figure 5.22 and Figure 5.23. Referring to Figure 5.15, depths should be 0.15 mm and 0.46 mm . However, these values are obtained from the construction layout of the specimen, they are not measured values, this possibly explain the noted differences (e.g. shifting of prepreg during curing).

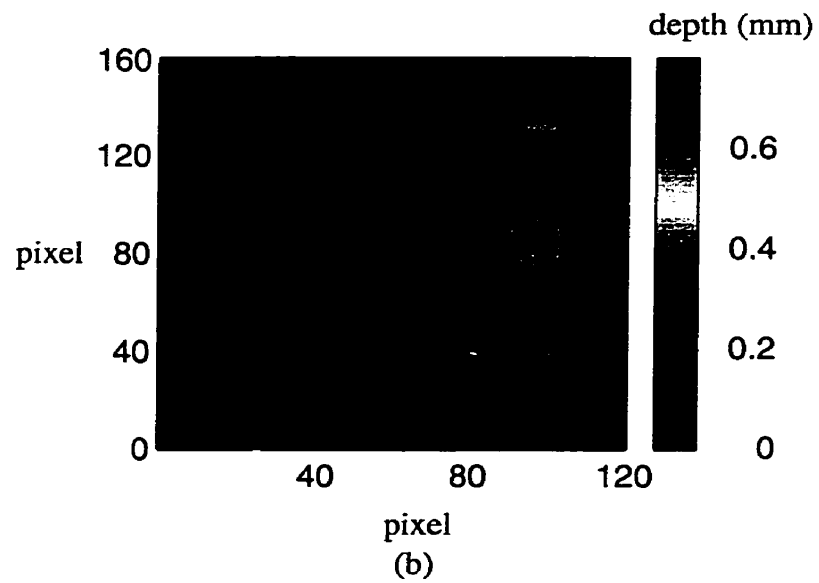
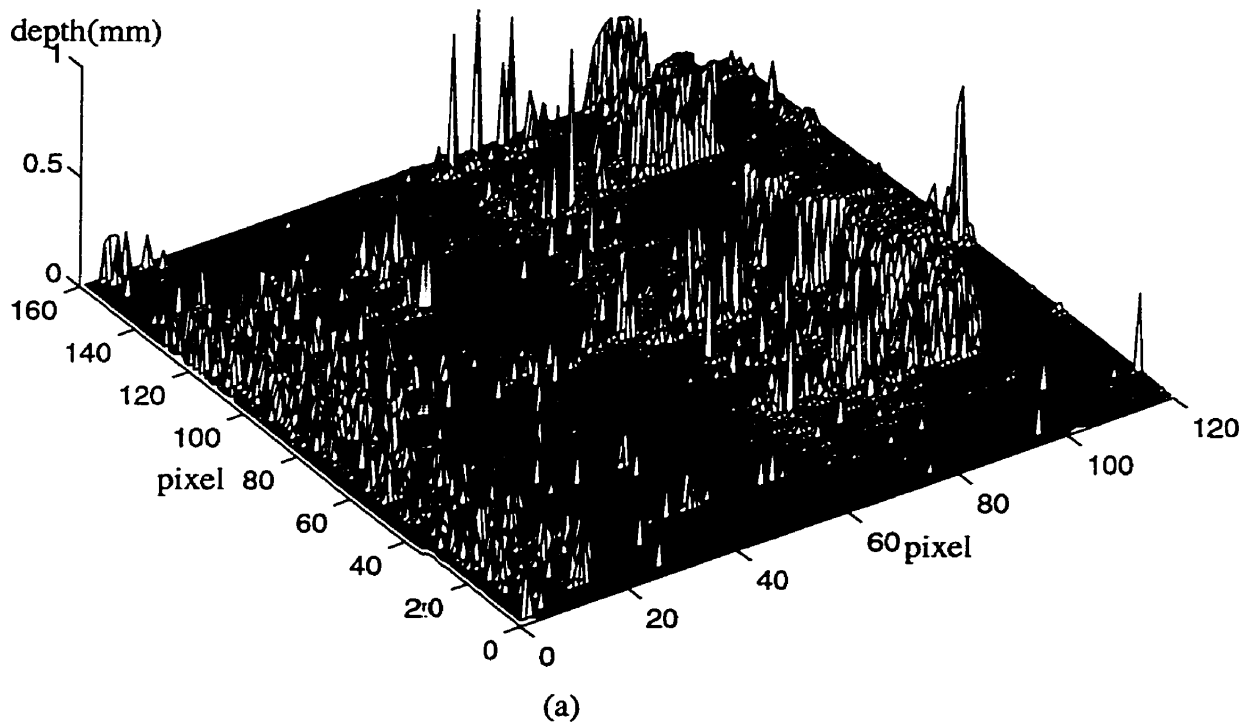


Figure 5.22 The estimator neural network output for a CFRP sample containing TeflonTM defect: (a) 3D depth profile: (b) depth image (sample of Figure 5.14)

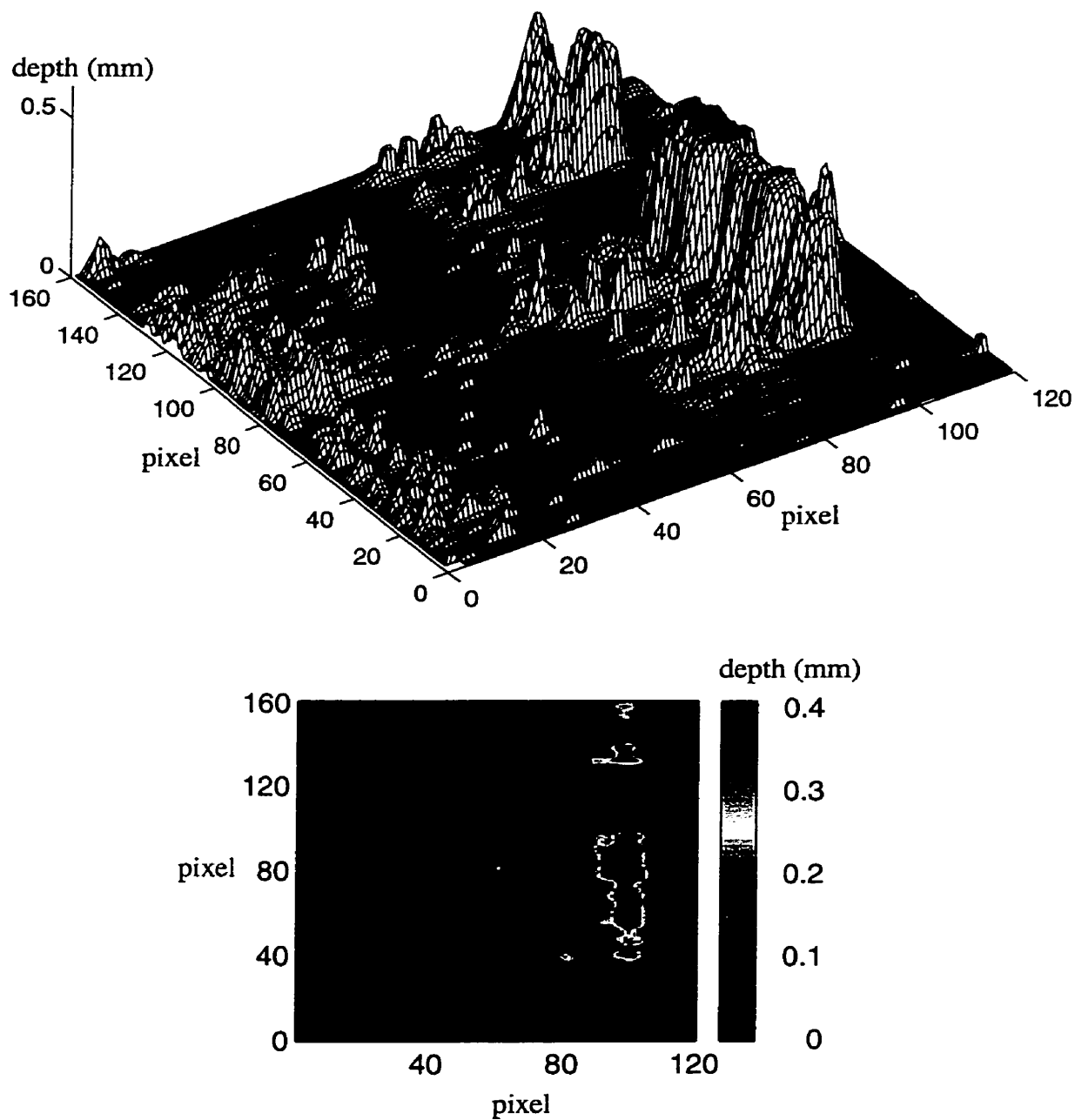


Figure 5.23 Filtered output of the estimator neural network for a CFRP sample containing TeflonTM defect: (a) 3D depth profile; (b) depth image (sample of Figure 5.14).

5.7 Conclusion and Contributions

Thermal data, raw temperature and contrast data, presented here showed that raw temperatures for defect region and sound area which are very close prevents reliable classification of different regions. To enhance raw temperature difference between sound and defect regions we used the thermal running contrast data curves to obtain better classification results. Two multilayer backpropagation neural networks were employed for defect detection and depth estimation of specimens under investigation in TNDE. The simulated data results have shown that if the networks are properly trained they can accurately detect and estimate defect depth even if the input data is contaminated with noise. Also, experimental results have demonstrated that NN trained by mathematical modeling data can provide a reliable mean to characterize defect parameters in TNDE. This is one of the contribution of this work to TNDE.

To maintain a high degree of classification accuracy, the networks should be trained by representative and non-redundant data sets. Training time for detector network, depending on the number of training set vectors, is about two to ten minutes using back propagation learning algorithm and for estimator network, it varies from ten minutes to two hours.

5.8 References

- [1] X. Maldague, "Nondestructive Evaluation Of Materials By Infrared Thermography", Springer-verlag London Limited, 1993.
- [2] J. C. Krapez and P. Cielo, 'Thermographic NonDestructive Evaluation: Data Inversion Procedures, Part I: 1-D Analysis and experimental results. Res Nondestruct Eval 3(2): 81-100 1991
- [3] V. Vavilov, "Thermal nondestructive testing", short history and state-of-art, QIRT 92, Eurotherm Series 27, Éditions Eurotherm. Paris 1992.
- [4] X. Maldague and S. Marinetti, "Pulse Phase infrared thermography", J. Appl. Phys., Vol. 79, No. 5, 1 March 1996.
- [5] M. R. Azimi-Sadjadi and S. A. Stricker, "Detection and classification of Buried Dielectric Anomalies Using Neural Networks-Further Results", IEEE Transaction on Instrumentation and Measurement, Vol. 4. 3, No. 1 February 1994.
- [6] X. Miao, M. R. Azimi-Sadjadi and B. Tian, "Detection of Mine and Minelike Targets Using Principal Component and Neural-Network Methods", IEEE Transaction on Neural Networks, Vol. 9, No. 3, May 1998.
- [7] X. Maldague, Y. Largouët, J. P. Couturier, "A study of defect depth using neural networks in pulsed phase thermography: modeling, noise, experiments," Rev. Gén. Therm. 37, 704-717, Elsevier, Paris, 1998.
- [8] S. Vallerand, A. Darabi, X. Maldague, "Defect Detection in Pulsed Thermography: A Comparison of Kohonen and Perceptron Neural Networks," SPIE: Thermosense XXI, R. N. Wurzbach, D. D. Burleigh eds., 3700: 20-25, Orlando, Fl, April 1999.

- [9] Y. Largouët, A. Darabi, X. Maldague, "Depth Evaluation in Pulsed Phase Thermography with Neural Network," Review of Progress in Quantitative NDE, D. O. Thompson et D. E. Chimenti eds, Plenum, 18A: 611-617, 1998.
- [10] D. R. Prabhu and W. P. Winfree, "Neural Network Based Processing of Thermal NDE Data for Corrosion Detection", QNDE, D. O. Thompson et D. E. Chimenti eds, Plenum, vol. 12, 1993.
- [11] P. G. Bison, C. Bressan, R. Disarno, E. Grinzato, S. Marinetti and G. Manduchi, "Thermal NDE of delamination in plastic materials by neural network processing", QIRT 94-Eurotherm Series 42-EETI ed., Paris 1995.
- [12] P.G. Bison, S. Marinetti, G. Manduchi, E. Grinzato, "Improvement of Neural Network Performances in Thermal NDE," in 3rd International Workshop - Advances in Signal Processing for NDE of Materials, X. Maldague ed., American Soc. of NDT, TONES, 3, 221-227, 1998.
- [13] E. Grinzato, V. Vavilov, P. G. Bison, S. Marinetti, C. Bressan "Methodology of processing experimental data in Transient Thermal NDT" Proc. SPIE, Vol. 2473, 1994
- [14] H. Trétout, D. David, J. Y. Marin and M. Dessendre, "An Evaluation of Artificial Neural Networks Applied to Infrared Thermography Inspection of Composite Aerospace Structures," Review of Progress in Quantitative Nondestructive Evaluation, Vol. 14, pp. 827-834, D. O. Thompson and D. E. Chimenti, Plenum Press, New York, 1995
- [15] E. Verma, "Fast Training of Multilayer Perceptrons", IEEE Transaction on Neural Networks Vol. 8, No. 6, November 1997.
- [16] S. Marinetti, X. Maldague, and M. Prystay, "Calibration Procedure for Focal Plane Array Cameras and Noise Equivalent Material Loss for Quantitative Thermographic NDT", Materials Evaluation, March 1997.

- [17] V. Vavilov, X. Maldague, B. Dufort, F. Robitaille and J. Picard, "Thermal nondestructive testing of carbon epoxy composites: detailed analysis and data processing", NDT&E International Volume 26 number 2, 85-95, 1993
- [18] J. C. Krapez, X. Maldague, P. Cielo, "Thermographic NonDestructive Evaluation: Data Inversion Procedures, Part II: 2-D Analysis and experimental results. Res Nondestruct Eval 3: 101-124 1991.
- [19] E.R. Dougherty, "An Introduction to Morphological Image Processing," SPIE Press, vol. TT9, 161 p., 1992

CHAPTER 6

Defect Characterization in TNDE Based on Neuro-Fuzzy Computation Techniques

6.1 Introduction

Similar to neural networks, fuzzy systems estimate a function without a mathematical model of how outputs depend on input data. This property gives opportunity to the system to learn from experience with numerical or linguistic data. This classifies them as model-free estimator systems. Fuzzy systems are based on fuzzy sets which were first proposed in 1965 by Lotfi A. Zadeh [1]. Fuzzy sets are extended forms of conventional “Boolean” sets that can handle the concept of partially true values between “completely true” and “completely false,” to deal with vagueness and uncertainty related to human linguistic and thinking principles of every day life [1], [2], [3], [4].

In many areas such as pattern recognition, communication, control, and so on, system modeling is an essential aspect, but on the other hand, traditional quantitative modeling techniques have significant limitations to solve other problems. Neuro-Fuzzy computing approaches to system modeling also attracted the attention of many researchers in the past several years [5]. This attraction is based on two key advantages of neuro-fuzzy systems. First, comparing to traditional quantitative modeling techniques, these systems are model-free and they do not require a mathematical description of the system. On the other hand, neuro-fuzzy methods possess both the low-level learning and computational power of neural networks and advantages of high-level human-like thinking of fuzzy systems [6], [7].

To build-up a fuzzy system, first one should provide linguistic variables in place of or in addition to numerical variables. Then, the system requires some IF-THEN fuzzy rules to characterize simple relations between fuzzy variables. Finally, complex relationships should be established by fuzzy reasoning algorithms for proposed fuzzy system. In general, fuzzy system modeling can be classified in two basic types. The first type was pioneered by Mamdani and Asilian in 1975. This system was applied to the regulation of a steam engine. The antecedent and consequent variables of IF_THEN rules are fuzzy in this system. This kind of model is also considered as a qualitative system modeling which uses human-like language expression [8]. The second type of fuzzy system modeling method, uses fuzzy inputs and rules but its outputs are non-fuzzy sets. This type of fuzzy model was initially proposed by Takagi and Sugeno [9]. It provides a powerful tool for modeling of complex nonlinear problems.

6.2 Fuzzy Logic

6.2.1 Definitions

To understand fuzzy logic, first the concept of a fuzzy set should be studied. A fuzzy set is an extension of a two-valued (crisp) set in which the boundary of each class is clearly defined. Let A and B be subsets of the universe X . The principle of crisp set theory union, intersection, complement, equality, and inclusion, are defined as follows:

- Union:

$$A \cup B = \{x|x \in A \text{ or } x \in B\} \quad (6.1)$$

- Intersection:

$$A \cap B = \{x|x \in A, x \in B\} \quad (6.2)$$

- Complement of A:

$$\bar{A} = \{x|x \notin A\} \quad (6.3)$$

For example: suppose the universe X defines the number of people ages:

$$X = \{0 \leq x \leq 130\},$$

the subset A is the people ages under 35 years old:

$$A = \{x|x \in X, x \leq 35\}$$

and subset B is the people ages above 15 years old:

$$B = \{x|x \in X, x \geq 15\}.$$

The union, intersection and complementary of subsets A and B can be given as:

$$A \cup B = X = \{0 \leq x \leq 130\}$$

$$A \cap B = \{x|x \in X, 15 \leq x \leq 35\}$$

$$\bar{A} = \{x|x \in X, x > 35\}.$$

The properties for ordinary set, such as associative, distributive, double negative, commutative, De Morgan, and idempotent laws are well known and for more details, the reader is referred to logics or mathematics books [10].

As seen in the example the crisp set contains objects that satisfy precise properties required by its characteristic function. For example, consider subset A which can be defined by its characteristics function X_A as:

$$X_A(x) = \begin{cases} 1 & \text{if } x \in X, x \leq 35 \\ 0 & \text{otherwise} \end{cases}$$

The characteristic functions of sets A , B , and the union, intersection and complementary of subsets A and B can be shown graphically as in Figure 6.1.

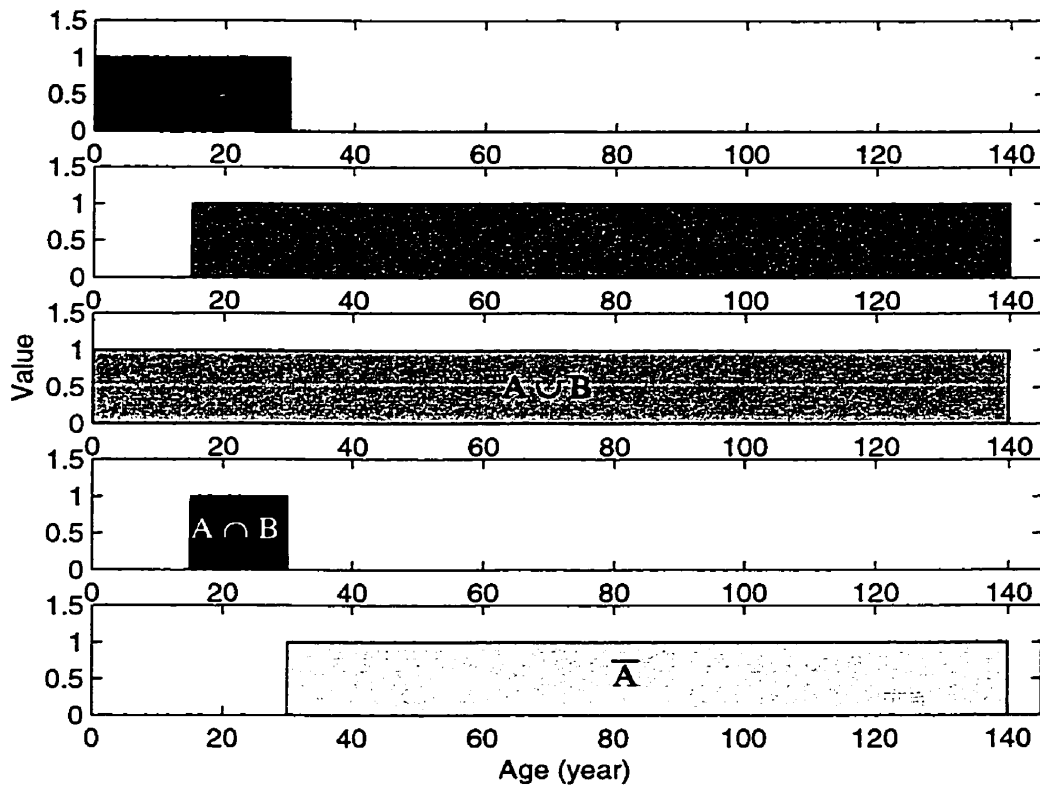


Figure 6.1 The characteristic functions for crisp sets A , B , and their union, intersection and complements.

In contrast, fuzzy set contains objects that satisfy imprecise properties of their membership functions. Sets such as children, young, or old people are examples of a fuzzy sets. In these examples the boundary of each set is not clearly defined. Lets, consider the young people set. It is difficult to classify people into “young” or not “young” people class. To being young is a matter of degree that can vary from teenagers to old people. To express the degree of being a child, young or old, we use membership function. The membership function for any fuzzy set maps sets objects into unit interval $[0, 1]$. Value “0” denotes the object does not belong to the set and value “1” corresponds to the object which is completely matched to the set. There is no unique membership function for any fuzzy set since it depends on applications and properties which are desired for that set. Suppose A is a fuzzy set in universe X with membership function m_A . For each object, x in A , the value of $m_A(x)$ represents the grade of membership of x in A . If A and B are two fuzzy sets, the fuzzy set operations can be defined as follows:

$$\forall x \in X$$

- Union:

$$A \cup B \Leftrightarrow m_{A \cup B}(x) = \max(m_A(x), m_B(x)) \quad (6.4)$$

- Intersection:

$$A \cap B \Leftrightarrow m_{A \cap B}(x) = \min(m_A(x), m_B(x)) \quad (6.5)$$

- Complement:

$$m_{\bar{A}}(x) = 1 - m_A(x) \quad (6.6)$$

- Equality:

$$A = B \Leftrightarrow m_A(x) = m_B(x) \quad (6.7)$$

- and Inclusion:

$$A \subset B \Leftrightarrow m_A(x) \leq m_B(x). \quad (6.8)$$

Now, let us consider once again the previous example where the universe X is the people age. The people can be divided into three groups as child, young, and adult people represented respectively by fuzzy sets A , B , and C . The membership function for these might be given by:

$$m_A(x) = \begin{cases} 1 & \text{if } x \leq 10 \\ \frac{-1}{5}x + 3 & \text{if } 10 \leq x \leq 15 \\ 0 & \text{if } x \geq 15 \end{cases}$$

$$m_B(x) = \begin{cases} 0 & \text{if } x \leq 10 \\ \frac{1}{10}x - 1 & \text{if } 10 \leq x \leq 20 \\ 1 & \text{if } 20 \leq x \leq 25 \\ \frac{-1}{10}x + 3.5 & \text{if } 25 \leq x \leq 35 \\ 0 & \text{if } x \geq 35 \end{cases}$$

$$m_C(x) = \begin{cases} 0 & \text{if } x \leq 30 \\ \frac{1}{15}x - 2 & \text{if } 30 \leq x \leq 45 \\ 1 & \text{if } x \geq 45 \end{cases}$$

Figure 6.2 illustrates membership functions of these fuzzy sets. When comparing Figure 6.1 and Figure 6.2, differences between fuzzy set membership function and crisp-set characteristic function are clearly seen but their differences are more interesting when we consider the union, intersection, complement or other relations of subsets on both sets (fuzzy and crisp-set). For example in crisp-set theory the union of each set and its complement is equal to the universe while the intersection of each set with its complement results in an empty set. On the other hand, the union of each fuzzy set and its complement does not always give the universe and intersection of them is not the empty set. Figure 6.3 shows some of these properties of fuzzy sets. In this example, we employ the simplest membership functions (trapezoidal membership functions) which are formed using straight lines. In fact, the membership function can be an arbitrary convex curve varying between 0 and 1. The fuzzy set A is convex if [4]:

$$\begin{aligned} & \text{for } \forall x_1 \in X, \forall x_2 \in X, \forall \lambda \in [0, 1] \\ & m_A(\lambda x_1 + (1 - \lambda)x_2) \geq \min(m_A(x_1), m_A(x_2)). \end{aligned} \quad (6.9)$$

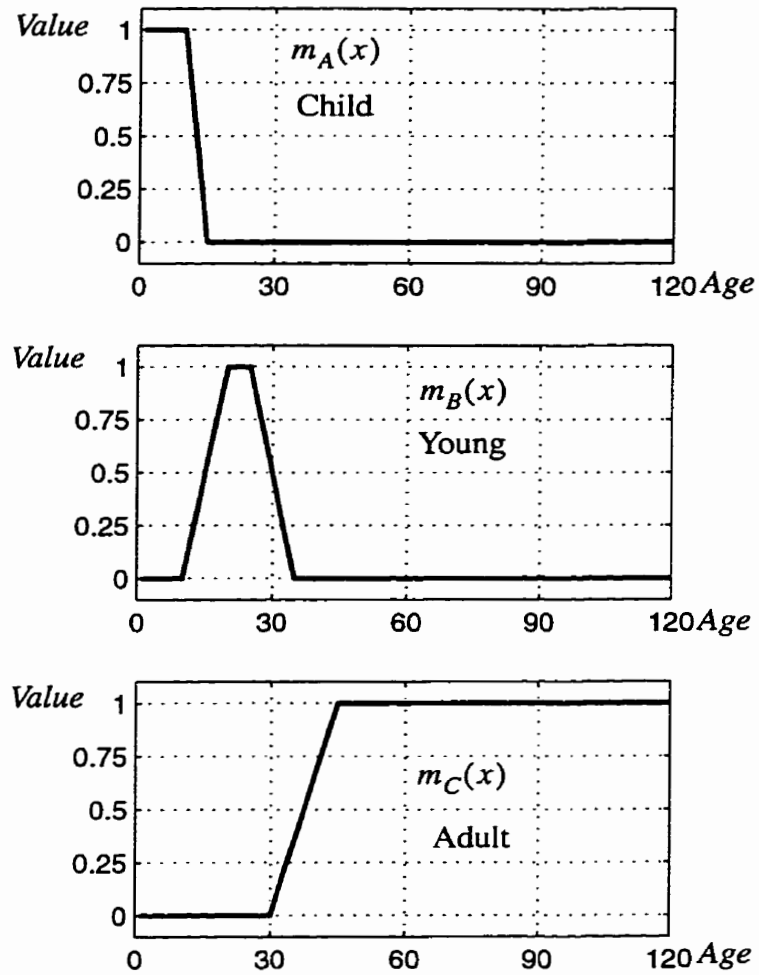


Figure 6.2 The membership functions for fuzzy sets A (Child), B (Young), C (Adult).

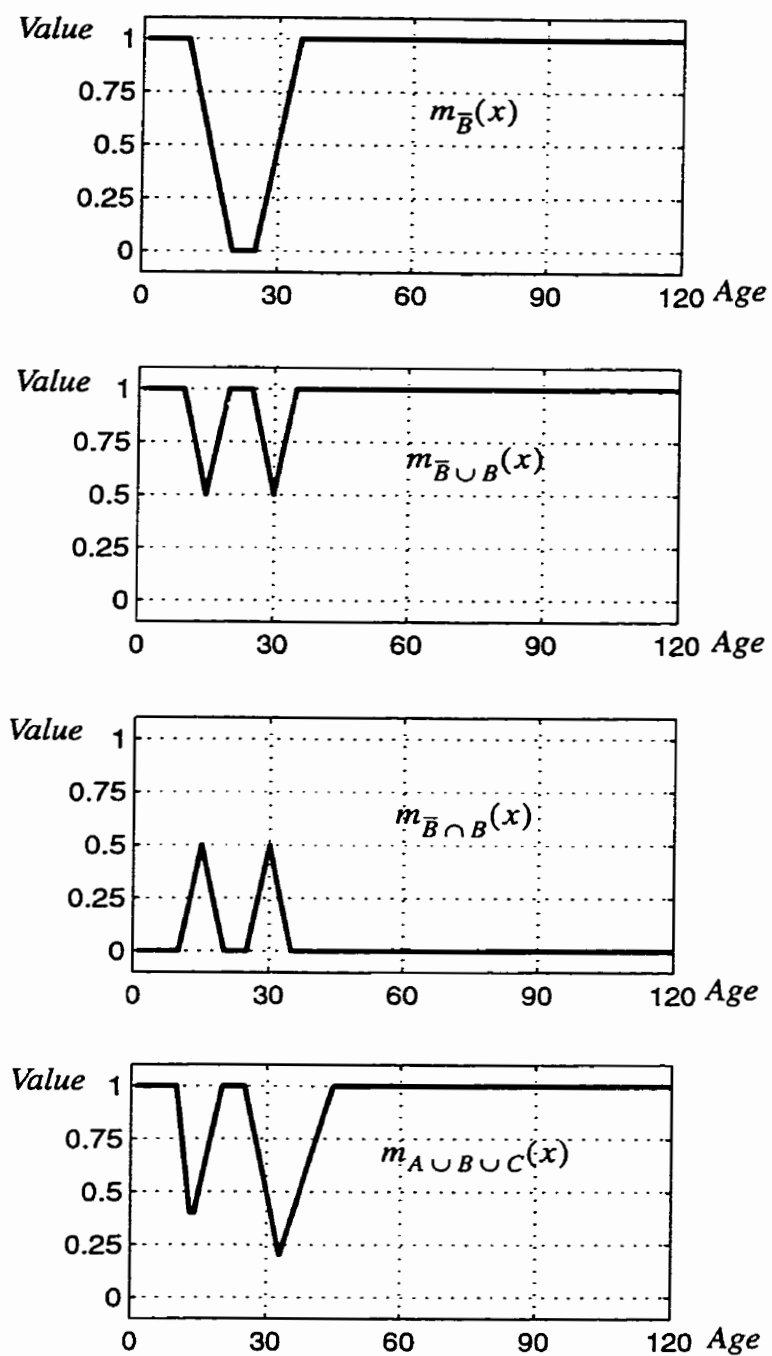


Figure 6.3 The membership functions for complement of fuzzy set B , union of fuzzy set B and its complement, intersection of fuzzy set B and its complement, and union of fuzzy sets A , B , and C .

6.2.2 Fuzzy Reasoning Mechanism

In fuzzy modeling, once input variables and their membership functions are defined, some inference rules (*if-then* rules) to perform fuzzy reasoning are needed. In general, two basic approaches are used to infer *if-then* rule in most applications of the fuzzy modeling systems. The fuzzy reasoning methods can be classified as the “traditional-fuzzy” modeling method, in which an a priori knowledge about the system is available, and the “classical-fuzzy” method which is based on the use of an input-output data relationship. The most popular of the traditional fuzzy reasoning method was first proposed by Mamdani and Asilian [8]. Additional to the input variables which are fuzzy sets for both reasoning methods, this inference method expects the output membership functions to be also fuzzy sets. The relations between fuzzy variables are given by composed conditional statements (*if-then* rules) which use the union or intersection operators called min-max operators. The general form of Mamdani fuzzy system rule using “and” operator is expressed by:

$$\mathbf{R}^i: \text{ If } x_1 \text{ is } X_1^i \text{ and } x_2 \text{ is } X_2^i, \dots, \text{ and } x_n \text{ is } X_n^i \text{ then } y \text{ is } Y_i. \quad (6.10)$$

Where \mathbf{R}^i is i^{th} rule of the system, $x_1, x_2, \dots,$ and x_n are input fuzzy variables, $X_1^i, X_2^i, \dots, X_n^i$ are input fuzzy sets, y is the output variable and Y_i is the i^{th} rule corresponding to the output fuzzy set. The true value of the antecedent part of i^{th} rule is derived from Eq. 6.10 using Eq. 6.5 as:

$$w_i = \min(m_{X_1^i}(x_1), m_{X_2^i}(x_2), \dots, m_{X_n^i}(x_n)). \quad (6.11)$$

Where w_i is the single value result of antecedent part that should be applied to the consequent part to get the i^{th} rule output value. Eq. 6.11 measures the adaptability of i^{th} rule to the input (x_1, x_2, \dots, x_n) and apply that result to the consequent part, this is known as an

implication. The implication process in fuzzy logics theory is similar to the binary logic. In binary logic the antecedent and consequent of an implication are either true or false but fuzzy theory permits the partial truth in antecedent and consequent part of fuzzy implication such as:

$$0.5p \rightarrow 0.5q.$$

Where p and q are the antecedent and consequent part variables of the implication. Therefore to obtain the output of each rule we should project the adaptability result to the consequent to specify a fuzzy set to be assigned to the output. The conclusion of the i^{th} rule is then given as:

$$m_{Y'_i}(y) = \min(w_p, m_{Y_i}(y)) \quad \forall y \in Y. \quad (6.12)$$

Where Y'_i is the conclusion fuzzy set of i^{th} rule and Y is the output universe. From aggregation of each rule conclusion fuzzy set, we can then obtain the final conclusion fuzzy set as:

$$m_{Y'}(y) = \max(m_{Y'_1}(y), m_{Y'_2}(y), \dots, m_{Y'_n}(y)) \quad \forall y \in Y. \quad (6.13)$$

In Eq. 6.13 Y' is called the aggregated output of the fuzzy system for a given input. Here, the “*max*” operand is chosen for aggregation process, but one can use any other functions depending on the application. To obtain the single output value, we need to defuzzify the aggregated fuzzy set. There are different methods of defuzzification such as *min*, *max*, *middle* and *centroid* calculation methods. The most popular defuzzification method is the centroid calculation which is given by [4]:

$$y_o = \frac{\int y m_{Y'}(y) dy}{\int m_{Y'}(y) dy} \quad (6.14)$$

where y_o is the single value output of the system.

Example: Let us consider a fuzzy system with two inputs (x_1, x_2) and one output (y) variables. The membership function of the variables is shown in Figure 6.4 and we suppose the following rules for this system:

R¹: If x_1 is X_1 and x_2 is X_3 then y is Y_2

R²: If x_1 is X_1 and x_2 is X_4 then y is Y_1

R³: If x_1 is X_2 and x_2 is X_3 then y is Y_3

R⁴: If x_1 is X_2 and x_2 is X_4 then y is Y_2

Figure 6.5 shows the reasoning process of each implication rules when the input x_1 and x_2 are respectively 30 and 35. As seen in the figure each rule takes the minimum value of the premises (the shaded part of first and second column in each row) and apply it to the consequence part to obtain the conclusion fuzzy set (the shaded part of third column). The aggregation process is done on all rule conclusions (third column) to give the final conclusion fuzzy set (the last row of third column). Then, defuzzification of this set by centroid method gives the system output as $y = 4.33$. Finally, Figure 6.6 shows the output surface (y) of the system versus its inputs (x_1, x_2).

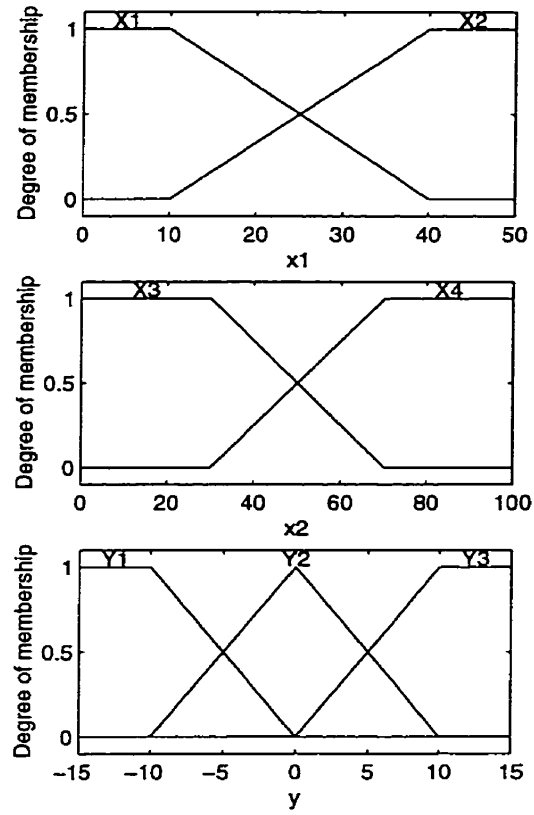


Figure 6.4 Membership functions for the inputs variables x_1 and x_2 and the output variable y .

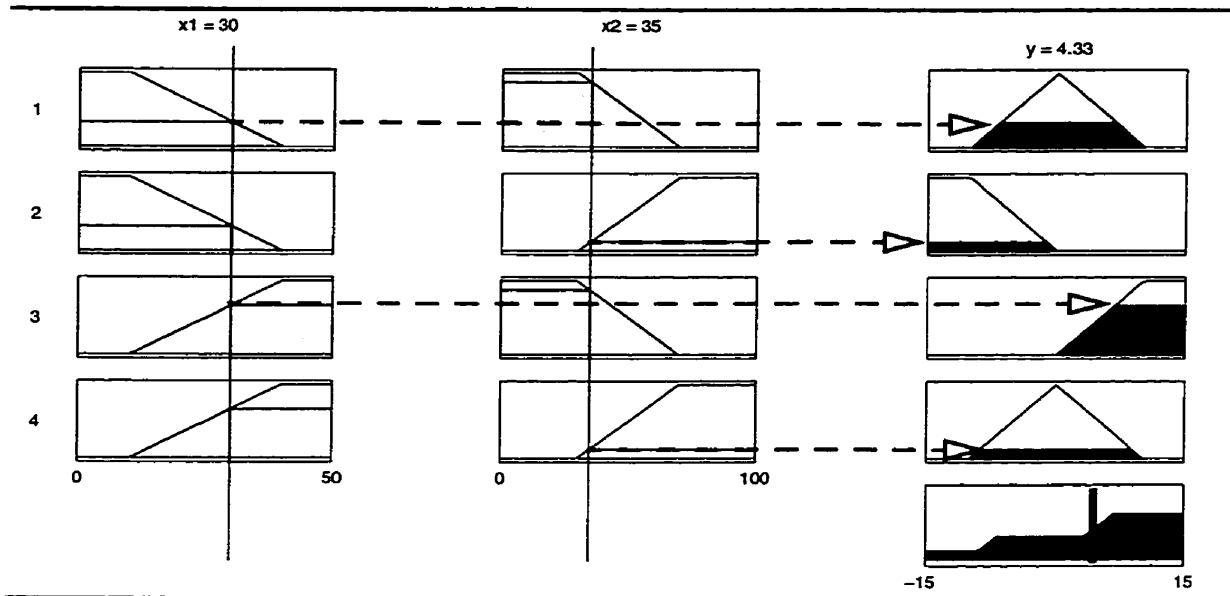


Figure 6.5 The reasoning process for a Mamdani fuzzy system with two inputs and one output variables and four rules. Given inputs are $x_1 = 30$ and $x_2 = 35$. The output value is $y = 4.33$, black vertical bar on the right bottom. It is calculated by the centroid method from the aggregated results of the rules.

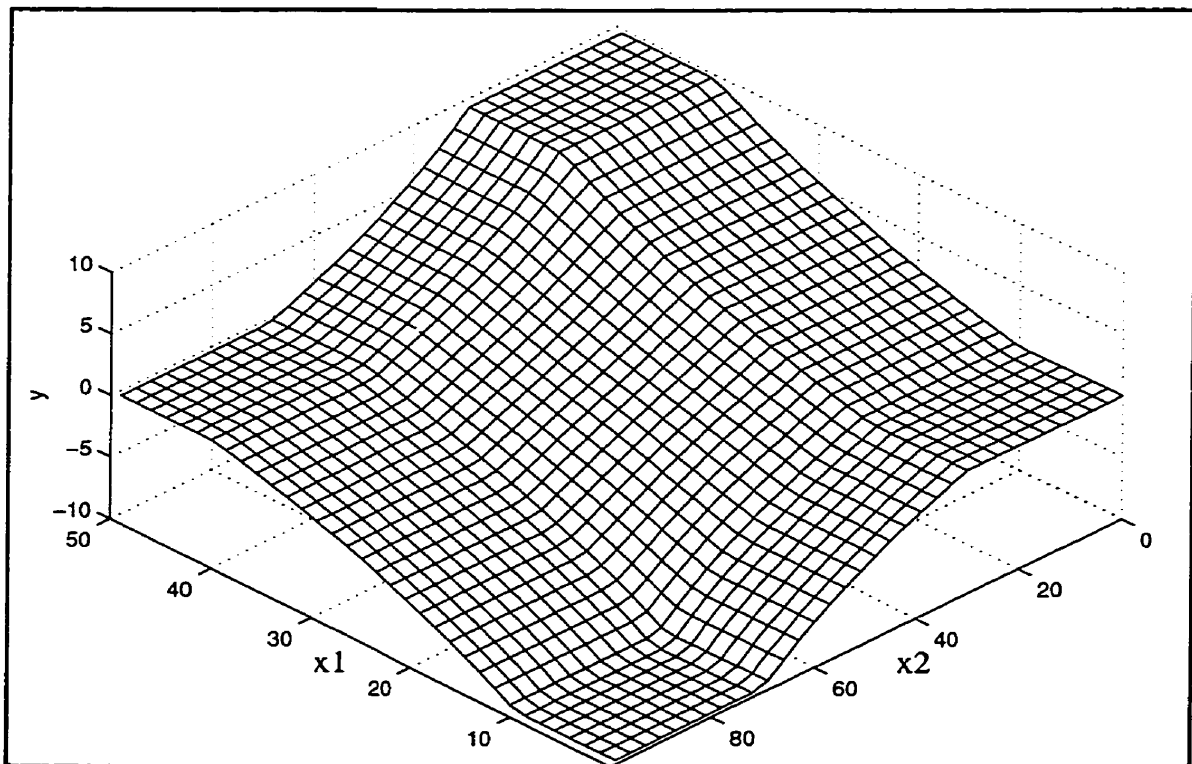


Figure 6.6 The output surface of the system following the Mamdani reasoning method.

The Mamdani type of reasoning contains linguistic variables with unimodal membership functions. They are linguistically understandable, but when we apply this method to multi-variable systems requiring many fuzzy variables, we have much difficulty to deal with compositional inference rules. T. Takagi and M. Sugeno suggested a mathematical approach to build-up a fuzzy system based on fuzzy partitioning of the input space [9]. In this method a linear input-output relationship is formed for each fuzzy subspace. The system output is given by the aggregation of the output conclusions of the rules. The general form of such a fuzzy rules is given as:

R^i : If x_1 is X_1^i and x_2 is X_2^i, \dots , and x_n is X_n^i then

$$y^i = C_0^i + C_1^i x_1 + C_2^i x_2 + \dots + C_n^i x_n \quad (6.15)$$

where R^i is i^{th} rule of the fuzzy system, x_1, x_2, \dots, x_n are input fuzzy variables, $X_1^i, X_2^i, \dots, X_n^i$ are input fuzzy sets and y^i is i^{th} rule output which is calculated by a given linear equation form the input values. In this equation, C_n^i is the coefficient of n^{th} input variable. Then, the system output is given by:

$$y = \frac{\sum_{i=1}^I w^i y^i}{\sum_{i=1}^I w^i} \quad (6.16)$$

where w^i defines the adaptability of the premises of the i^{th} rule that is expressed by:

$$w^i = \prod_{n=1}^N m_{X_n^i}(x_n). \quad (6.17)$$

In this equation, \prod stands for the *min* operation.

Example: Lets consider again the previous example which explained different steps of Mamdani fuzzy reasoning. We want now to handle this example with the Sugeno's reasoning method. We suppose that input variables membership functions are the same as in the previous example and the following rules are given:

$$\mathbf{R^1: \text{ If } x_1 \text{ is } X_1 \text{ and } x_2 \text{ is } X_3 \text{ then } y = 0.1x_1 - 0.2x_2 - 2}$$

$$\mathbf{R^2: \text{ If } x_1 \text{ is } X_1 \text{ and } x_2 \text{ is } X_4 \text{ then } y = 0.1x_1 - 0.2x_2 - 7}$$

$$\mathbf{R^3: \text{ If } x_1 \text{ is } X_2 \text{ and } x_2 \text{ is } X_3 \text{ then } y = 0.1x_1 - 0.05x_2 + 11}$$

$$\mathbf{R^4: \text{ If } x_1 \text{ is } X_2 \text{ and } x_2 \text{ is } X_4 \text{ then } y = 0.1x_1 - 0.05x_2 + 11}$$

Figure 6.7 shows the Sugeno reasoning process for this example. The input variables, x_1 and x_2 , are respectively set to 25 and 40. Each rule conclusion, the light bar, is related to the input variable values according to the expression given for each rule as a consequent part. Its adaptability, the dark bar, is defined by the *min* operation from membership degrees of given input variables.

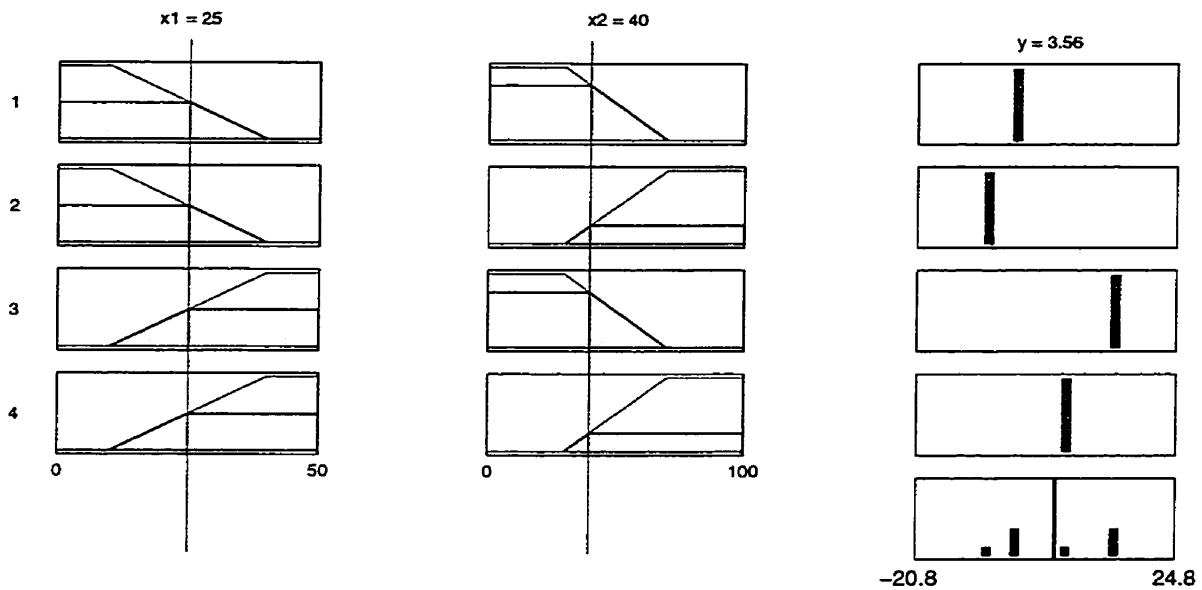


Figure 6.7 The reasoning process for a Sugeno fuzzy system with two inputs and one output variables and four rules. Given inputs are $x_1 = 25$ and $x_2 = 40$. The output value is $y = 3.56$, thin bar on the right bottom. It is calculated by the centroid method from the aggregated results of the rules.

The aggregated result, the blue bars, is shown on bottom of third column and the final conclusion, the red bar, is $y = 3.56$ while it was $y = 4.33$ for Mamdani reasoning method result for given $x_1 = 30$ and $x_2 = 35$. This difference is due to membership functions in consequent parts of both systems. Although, the output range for each rule is defined as in the previous example, from -15 to 15, the final output range of the system is changed, from -20.8 to 24.8. The output surface of the system is shown in Figure 6.8. It looks similar to the output surface of the fuzzy system reasoning with Mamdani method in the previous example.

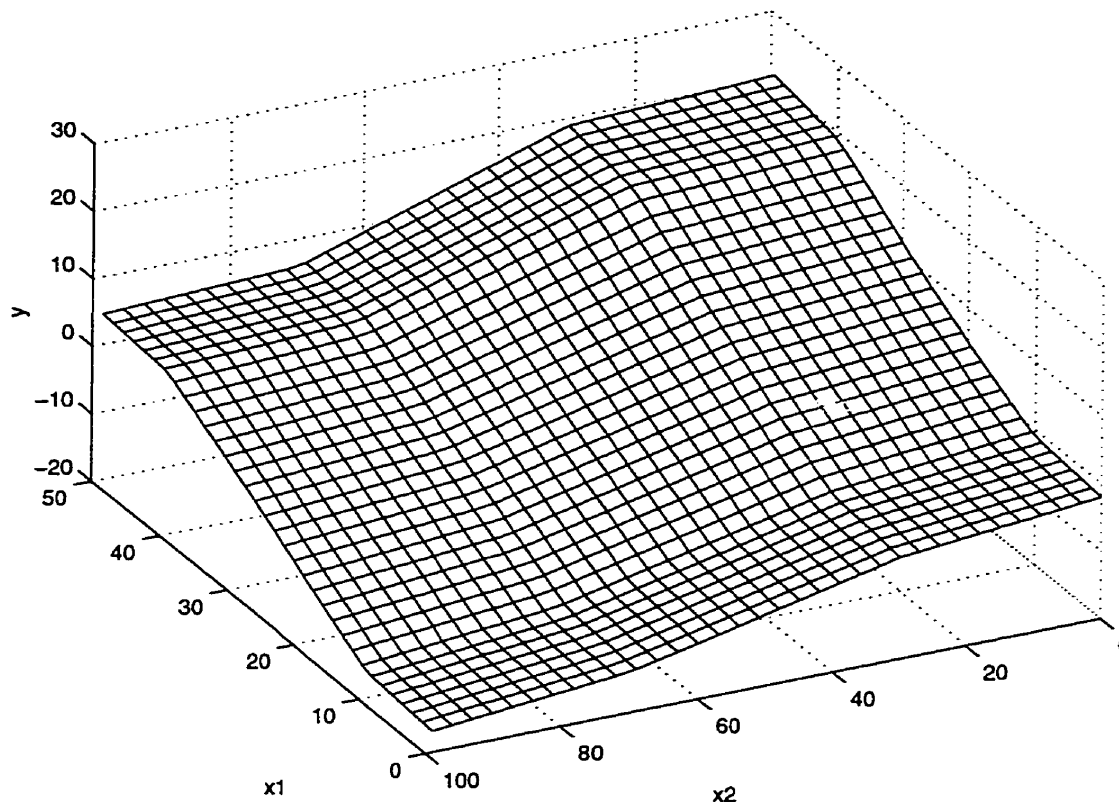


Figure 6.8 The output surface of the system with Sugeno reasoning method

One of the advantages of the Sugeno reasoning method is that we can reduce the number of implications [9]. To illustrate this, we suppose the above discussed fuzzy system has only two implication rules as:

$$\mathbf{R}^1: \text{ If } x_1 \text{ is } X_1 \text{ then } y = 0.1x_1 - 0.2x_2 - 4.5$$

$$\mathbf{R}^2: \text{ If } x_1 \text{ is } X_2 \text{ then } y = 0.1x_1 - 0.05x_2 + 8.$$

The linear equation in the consequent part of each rule takes into consideration the input variables x_1 and x_2 to find the position of the conclusion although its weight is obtained only by considering variable x_1 as shown in Figure 6.9. Figure 6.10 shows the

behavior of this system. It is obvious that the output of the Sugeno fuzzy system with four implication rules is much flexible but this system output results is still acceptable.

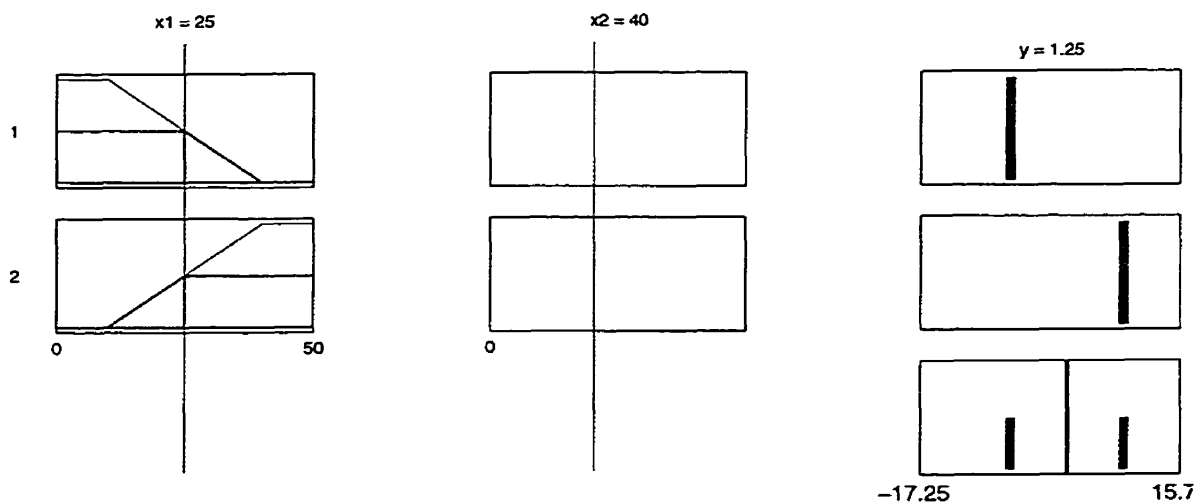


Figure 6.9 The reasoning process for a Sugeno fuzzy system with two inputs and one output variables and two rules. Given inputs are $x = 25$ and $x = 40$. The output value $y = 1.25$, as shown by the red thin bar on the right bottom.

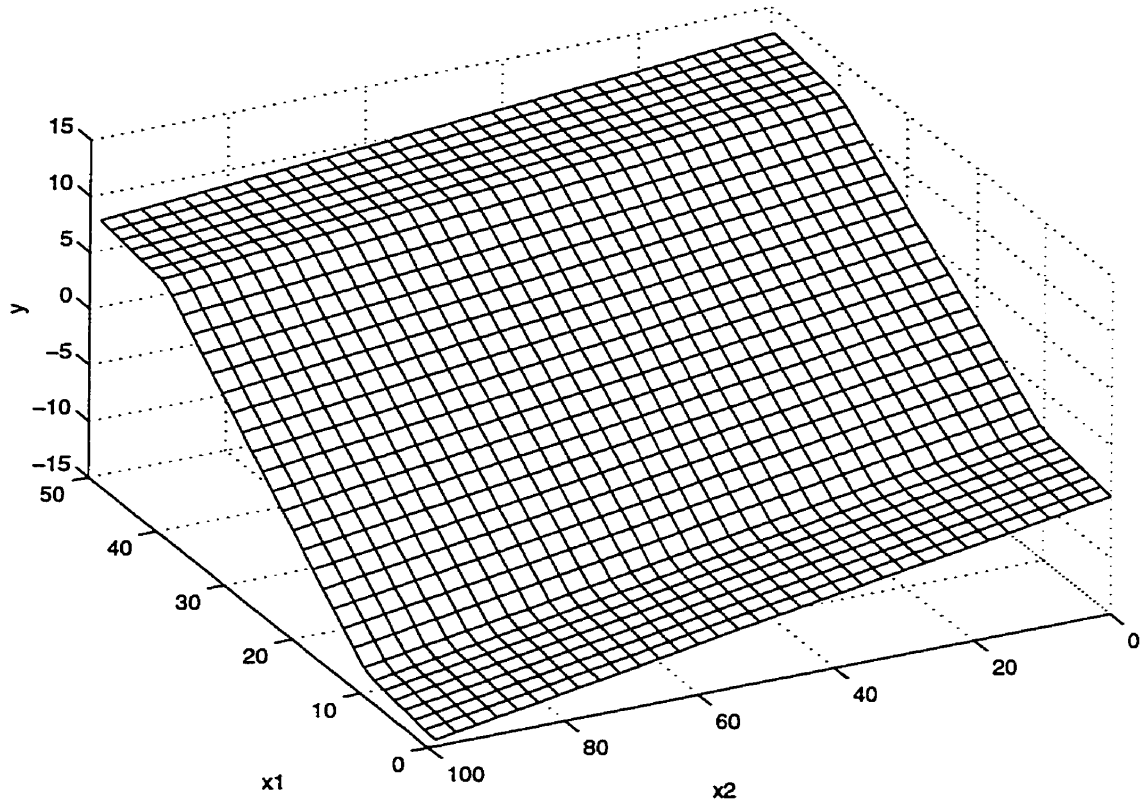


Figure 6.10 The output surface of the Sugeno fuzzy system with two implication rules.

6.3 Neuro-Fuzzy Defect Depth Estimation

The conventional fuzzy system modeling uses a single model to describe the global behavior of a system. This kind of fuzzy system modeling needs a large number of rules to represent the behavior of a sophisticated system. The Takagi-Sugeno-Kang (TSK) system modeling method divides the input space to subspaces and gives a simple model for each input subspace which are called submodel of the system [9], [11]. Combining these submodels then describes the global behavior of the system. On the other hand, since the consequent part of implications are explicitly expressed by the input variables, some learning algorithms can be employed to identify system parameters [12]. Several approaches have been proposed to generate fuzzy *if-then* rules, from training data, based on TSK fuzzy model. One such an approach is called the Adaptive-Network-Based Fuzzy Inference System (ANFIS). ANFIS is a class of adaptive multi-layer feed-forward network

that is functionally equivalent to a fuzzy inference system. Each neuron in ANFIS applies a particular function on incoming signals as well as a set of parameters relating to the neuron. To identify the adaptive network parameters, this fuzzy inference method employs a hybrid learning algorithm which combines the gradient method and least squares estimate (LSE). Not only can this hybrid learning algorithm guarantee to find global minima but it also cut down the convergence time of the network due to decreasing dimensions of research space in the gradient method [13].

ANFIS, which has the advantages of both the low-level learning and computational power of neural networks and the high-level of human-like thinking of fuzzy inference systems, can be applied to complex nonlinear problems such as defect depth estimation in TNDE. This section is dedicated to defect depth estimator using ANFIS. As discussed earlier the number of rules will exponentially augment while increasing the number of input variables to the system. For example, if we consider thermal contrast vectors, 16 sampled points for each vector as inputs to the system and suppose two labels for each sampled point, then the ANFIS requires 2^{16} initial rules! This complicates the reasoning process and is beyond fuzzy system modeling goals. Therefore, the system should be provided with less characteristics data points. It is reported that under some circumstances the defect depth can mathematically be expressed as a function of the maximum contrast and its occurrence time. Such a relation for graphite epoxy specimens is given by [14]:

$$Z_{def} = 0.6722 \sqrt{t_{Cmax}} (C_{max})^{-0.258} . \quad (6.18)$$

Where Z_{def} is defect depth, t_{Cmax} is time of the maximum contrast and C_{max} is maximum contrast on the specimen surface.

Here, we will provide four additional informative parameters such as time of half-rise contrast $t_{1/2Cmax}^-$, time of half-decay $t_{1/2Cmax}^+$ and their related contrast for the ANFIS depth estimator. These parameters are shown in Figure 6.11 for a simulated TeflonTM defect at depth 0.7 mm , the difference between half-rise and half-decay contrasts is due to the sampling time. Now, we will propose two ANFIS depth estimators, one for the CFRP samples containing TeflonTM defects and the other for samples with air defects. First, the

ANFIS depth estimators are provided with training vectors as shown in Figure 6.12. Each training vector has seven variables which are t_{Cmax} , $t_{1/2Cmax}^+$, $t_{1/2Cmax}^-$, their related contrast as inputs, and depth corresponding to the chosen pixel as the output of the estimator.

If we assign two membership functions to each input variables, then the ANFIS systems have 64 rules. The initial membership function for each input variable is two equally spaced bell-shape functions with enough overlap within the range as shown in Figure 6.13. The training process takes about 2 minutes on a Sun workstation (ULTRA 30). This is shorter than the training process time of the depth estimator using neural network of the previous chapter. The final membership functions of input variables and system error for TeflonTM defect depth estimator ANFIS are respectively shown in Figure 6.14 and Figure 6.15. As seen in Figure 6.14, the shape of the membership functions changed during the training process to minimize the output error of the estimator.

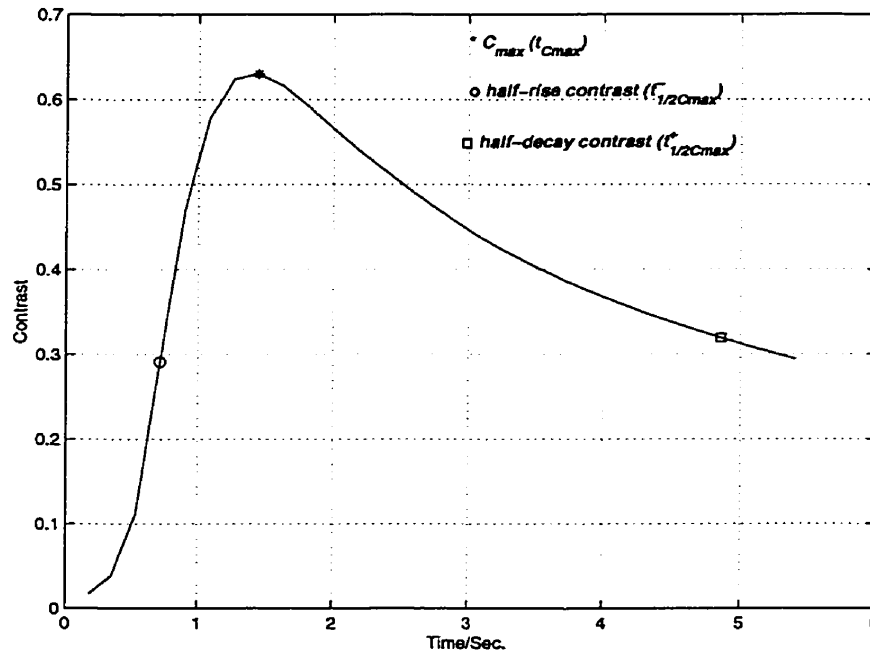


Figure 6.11 Normalized contrast curve on the surface of a CFRP sample over a TeflonTM subsurface defect at 0.7 mm depth. The circle, star and square points are respectively half-rise, half-decay and maximum contrast. Their occurrence time serves to define an input vector for the ANFIS depth estimator. The difference between half-rise and half-decay contrast amplitudes is due to their sampling time.

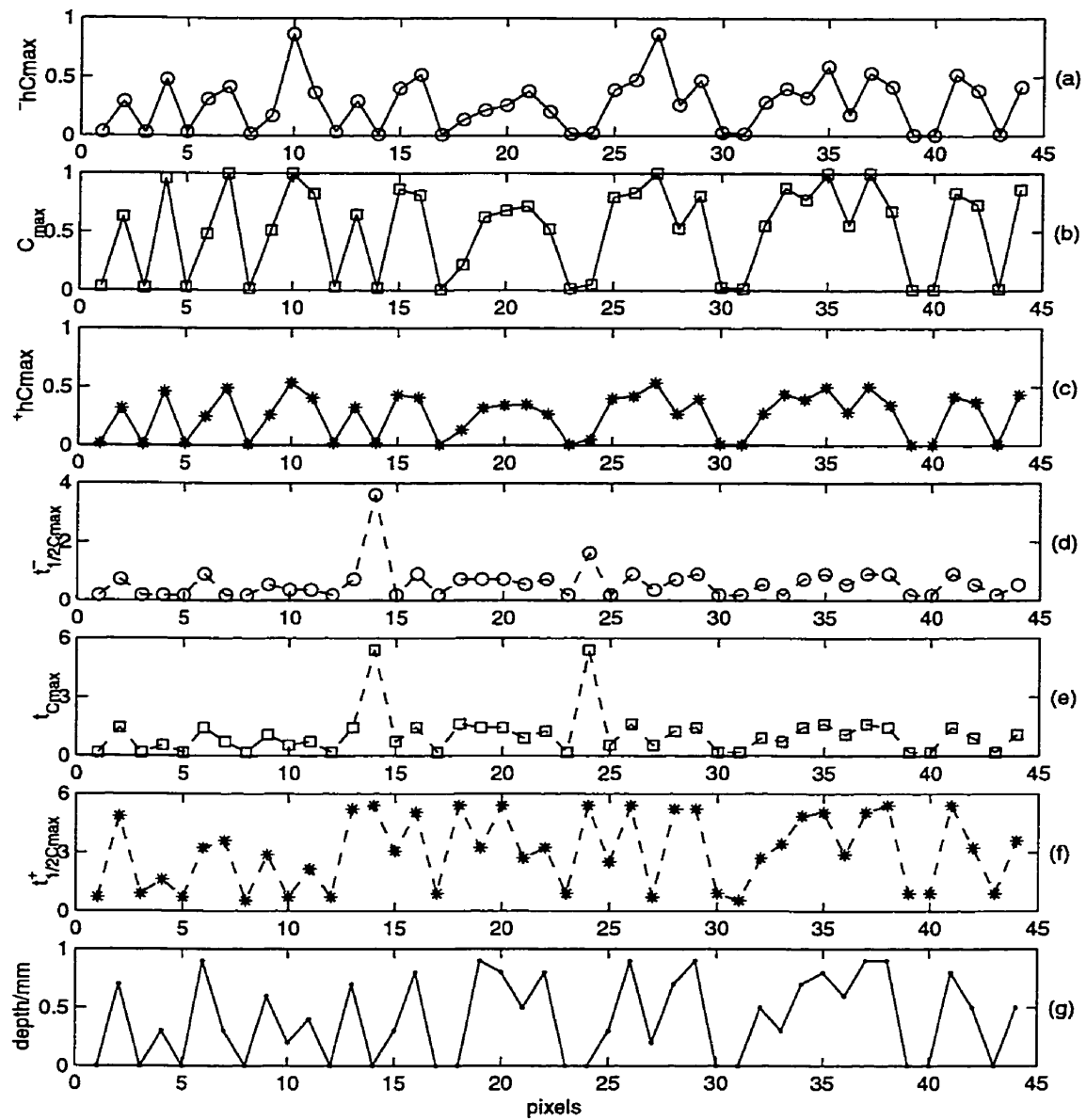


Figure 6.12 Training set for ANFIS depth estimator. The vectors extracted from simulated data of CFRP samples containing TeflonTM defects at various depths. (a) half-rise contrast (b) maximum contrast (c) half-decay contrast (d) half-rise contrast time (e) maximum contrast time (f) half-decay contrast time (g) depth.

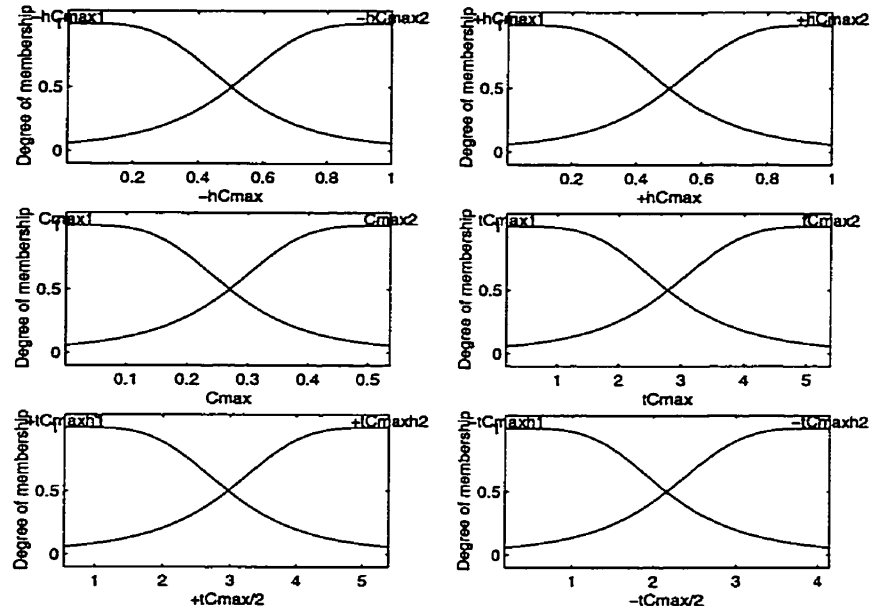


Figure 6.13 Initial membership functions of input variables for ANFIS depth estimator: half-rise contrast ($-hC_{max}$), maximum contrast (C_{max}), half-decay contrast ($+hC_{max}$), half-rise contrast time ($-tC_{max}/2$), maximum contrast time (tC_{max}), half-decay contrast time ($+tC_{max}$).

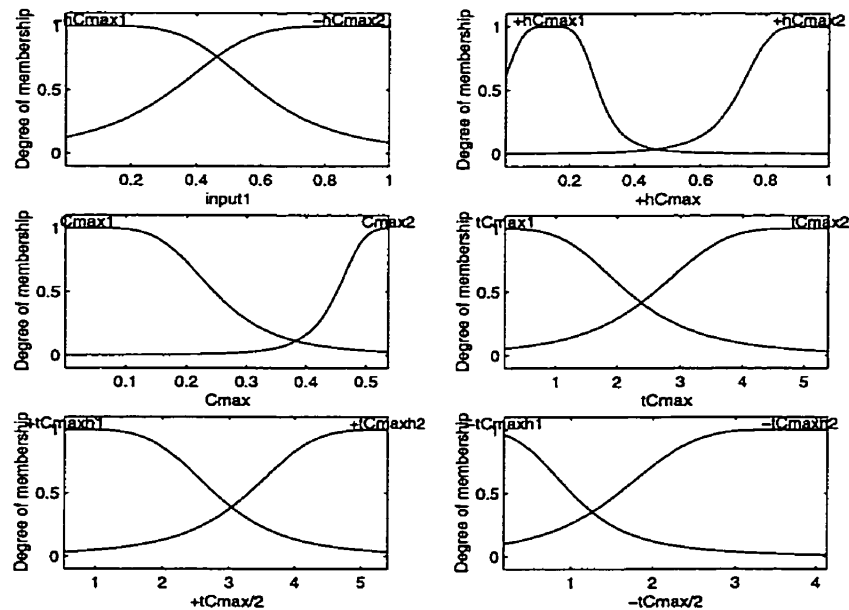


Figure 6.14 Final membership functions of input variables for buried TeflonTM in CFRP samples ANFIS depth estimator: half-rise contrast ($-hC_{max}$), maximum contrast (C_{max}), half-decay contrast ($+hC_{max}$), half-rise contrast time ($-tC_{max}/2$), maximum contrast time (tC_{max}), half-decay contrast time ($+tC_{max}$).

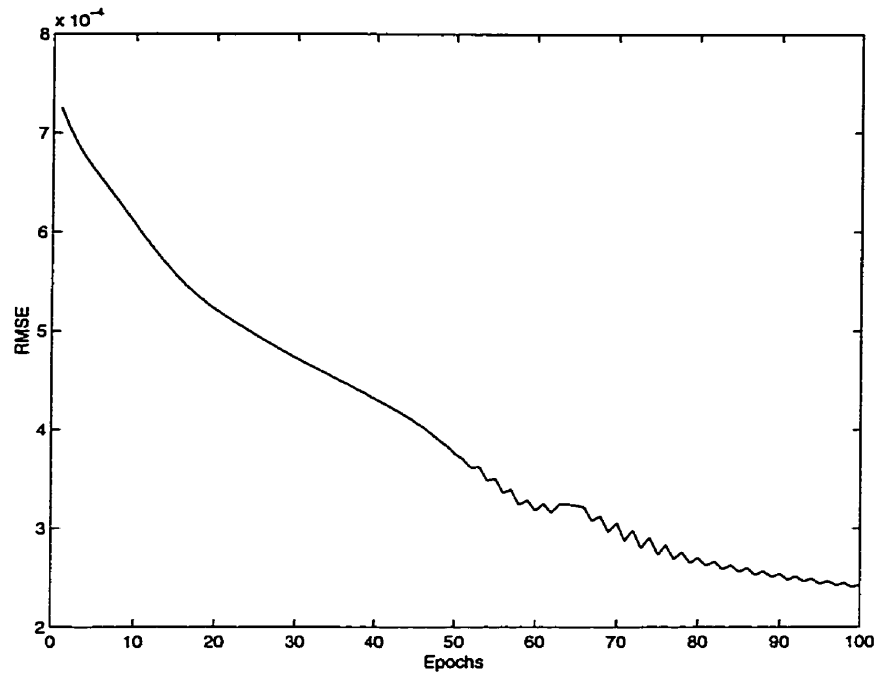


Figure 6.15 RMSE (root mean squared error) curve for buried TeflonTM in CFRP samples ANFIS depth estimator.

To examine the subsurface air defect, with the ANFIS depth estimator, we take the input data extracted from the CFRP sample containing a T-shape air defect as shown in Figure 5.10. The estimated depth profile without any post processing is shown in Figure 6.16 (b). This figure shows that the ANFIS depth estimator is able to estimate simulated defect depths as well as the neural network depth estimator proposed in chapter 5. If the detected error pixels are removed, the estimated depth for defect pixels becomes as illustrated in Figure 6.16 (c). Comparing this figure with original depth profile shown in Figure 6.16 (a) confirms precision and reliability of the ANFIS depth estimators. The estimated depth profile error is depicted in Figure 6.16 (d) and the estimated depth profile error in which the error pixels have been removed is shown in Figure 6.16 (e). The average relative error over defect area is 8.66%. The 3-dimensional estimated depth profile is shown in Figure 6.17.

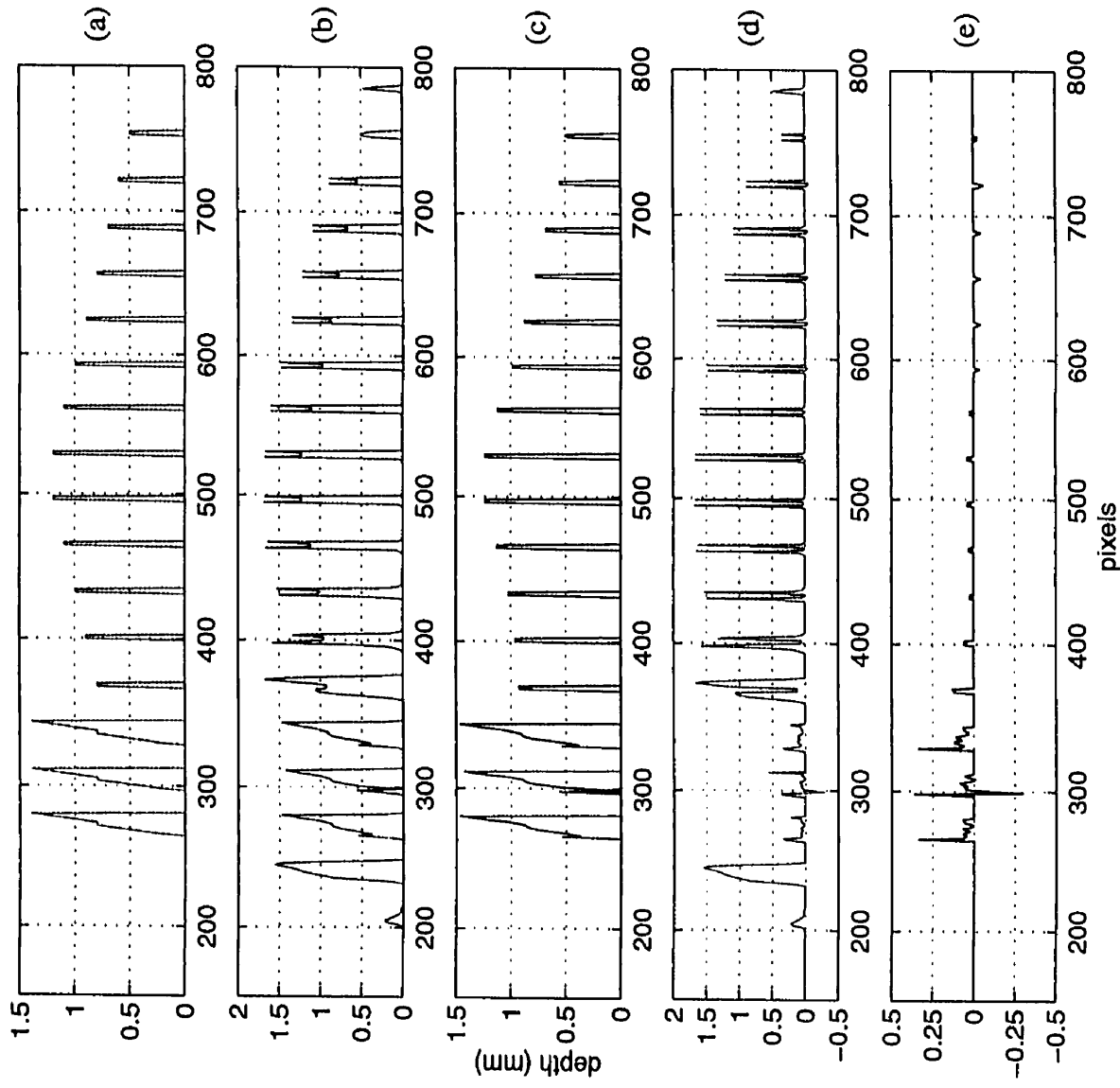


Figure 6.16 Depth profile for T-shape air defect buried in CFRP sample. (a) Original depth profile (b) estimated depth profile of air defect by ANFIS depth estimator (c) the estimated depth profile in which error defect pixels have been removed (d) the estimated depth profile error (e) the estimated depth profile error in which error defect pixels have been removed.

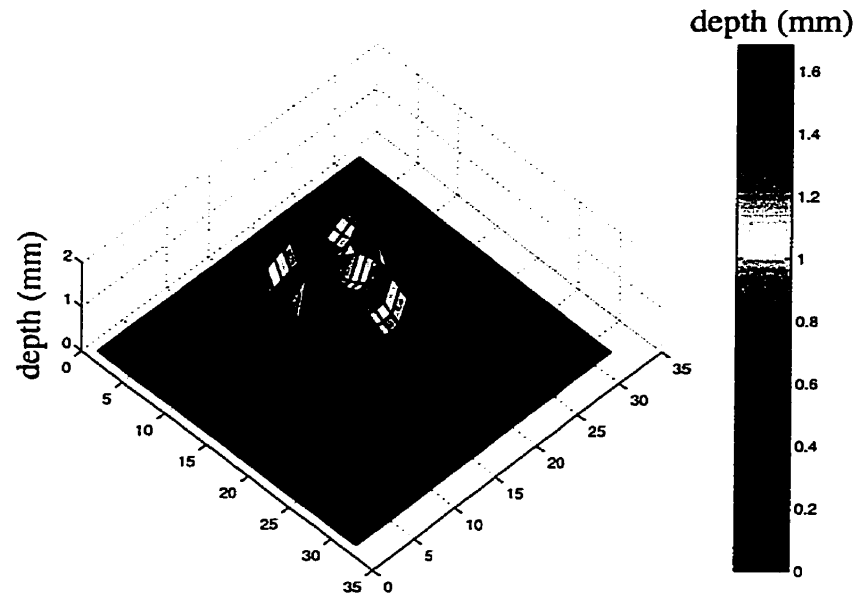


Figure 6.17 3-D estimated depth profile of the subsurface air defect ANFIS depth estimator for T-shape air defect buried in CFRP sample.

As mentioned in chapter 5, the available simulated data for the CFRP samples containing TeflonTM defect are only valid for defects greater than 1 mm depth. On the other hand the Maspar is now unfortunately out of operation in our laboratory, so that we could not modify the set-up parameters to have new reliable data for the training process. This means we have access to limited data to work with CFRP samples containing TeflonTM defects for the experimental part of our project. Nevertheless we used the available data for training the TeflonTM defect ANFIS depth estimator.

After training the TeflonTM defect ANFIS depth estimator, we provided the input data extracted from the real IR images presented in section 5.5 for a CFRP sample with rectangular TeflonTM defects (Figure 5.15). The ANFIS depth estimator output is shown in Figure 6.18. Although, the ANFIS depth estimator reveals both defect and estimated their depth, there is still a lot of noise that prohibits visualization of the estimated depth profile over defects. Therefore, the output is filtered using a median mask and depth profile is represented in Figure 6.19. This figure shows that the estimator classify some other than defect region pixels as defect. This is due to both non-uniform heating of the sample surface

and non-homogeneity of thermal properties in this CFRP sample. Nevertheless, the estimated depth over defect region somehow agrees with the result of estimated depth by the neural network depth estimator. Moreover, it seems that the defects are revealed more clearly by ANFIS depth estimator as compared to neural network depth estimator results in Figure 5.22 and Figure 5.23.

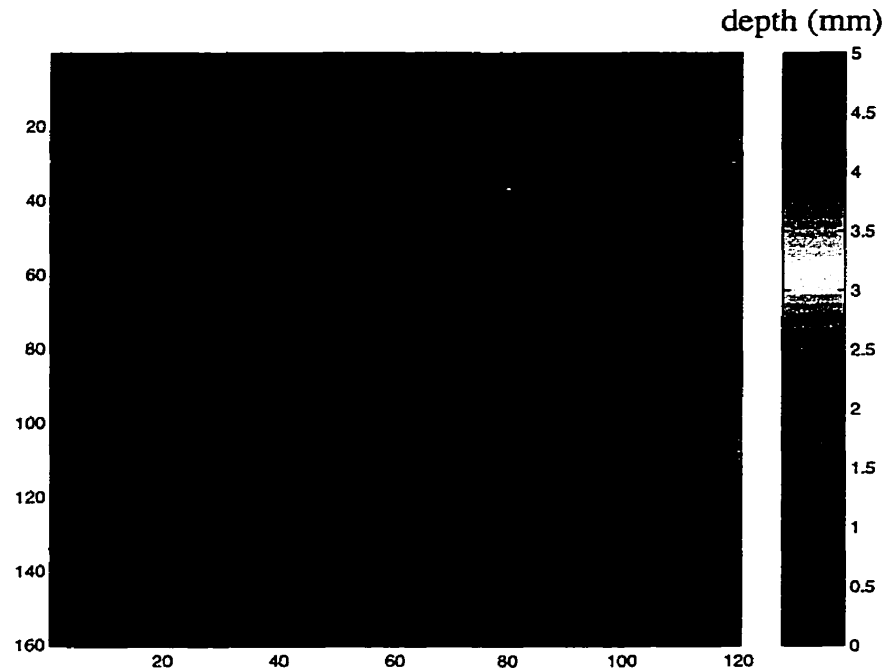


Figure 6.18 Estimated depth image of TeflonTM defect by ANFIS depth estimator for sample shown in Figure 5.15 (to be compared with Figure 5.16 (d), p. 97 and Figure 5.22, p. 106.

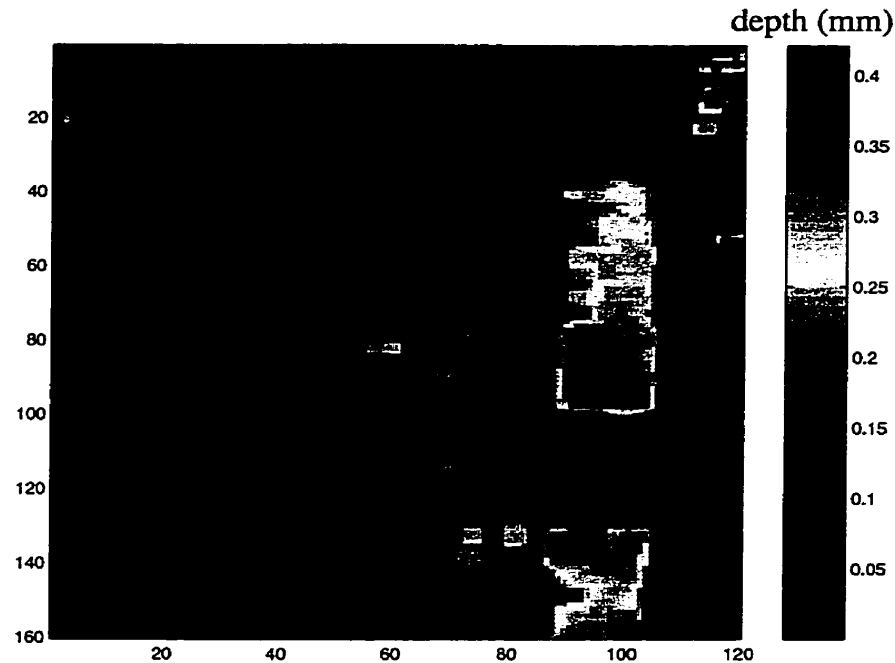


Figure 6.19 TeflonTM defect ANFIS estimated depth image which has been filtered by a median filter. Two defect at depth between 0.25 mm and 0.35 are clearly seen.

6.4 Conclusion and Contributions

We have discussed the concept of fuzzy sets and demonstrated their advantages for data interpretation and classification as compared with crisp set theory. Two fuzzy system modeling approaches, Mamdani and TSK fuzzy models, were reviewed. TSK model permits to divide complex problem to simple submodels where in each submodel a linear relation can simply be established between its premiss and consequence parts. We also described how an adaptive-network based fuzzy inference system (ANFIS) can employ an hybrid learning algorithm to define if-then rules for a complex system expressed with a training set. Finally we proposed a neuro-fuzzy depth estimator based on ANFIS system modeling. The proposed defect depth estimator was tested on simulated and real experimental data. The results showed this new approach brings both accuracy and short training time for quantitative thermal testing method. This is another contribution of this thesis to the TNDE field [15].

6.5 References

- [1] L. A. Zadeh, "Fuzzy sets". *Inform. Control*, Vol. 8, pp 338-353, 1965
- [2] L. A. Zadeh, "Outline of a New Approach to the Analysis of Complex System and Decision Processes", *IEEE Trans. Syst. Man, Cybern.*, vol. 3, pp. 28-44, 1973.
- [3] B. Kosko, "Neural Networks and Fuzzy Systems", Englewood Cliffs, NJ: Prentice-Hall, 1992.
- [4] K. Tanaka, "An Introduction to Fuzzy Logic for Practical Applications", Springer-Verlag, 1997
- [5] M. R. Emami, I. B. Türksen, and A. A. Goldenberg, "Development of A Systematic Methodology of Fuzzy Logic Modeling", *IEEE Trans. Fuzzy Syst.* vol. 6, no. 3, pp. 346-361 Aug., 1998.
- [6] M. Sugeno and T. Yasukawa, "A Fuzzy-Logic-Based Approach to Qualitative Modeling", *IEEE Trans. Fuzzy Syst.* vol. 1, no. 1, pp. 7-31 Feb. 1993.
- [7] C. F. Juang and C. T. Lin, "An On-Line Self-Construction Neural Fuzzy Inference Network and Its Applications", *IEEE Trans. Fuzzy Syst.* vol. 6, no. 1, pp. 12-32 Feb. 1998.
- [8] E. Mamdani and S. Asilian, "An Experiment in Linguistic Synthesis with a Fuzzy logic Controller", *International Journal of Man Machine Studies*, vol. 7, pp 1-13, 1975.
- [9] T. Takagi and M. Sugeno, "Fuzzy identification of systems and its application to modeling and control", *IEEE Trans. Syst. Man, Cybern.*, vol. SMC-15, pp. 116-132, Jan. 1985.
- [10] M., Morris, "Digital Design," 2e edition, 1991.

- [11] M. Sugeno and G. T. Kang, "Structure identification of fuzzy model", *Fuzzy Sets Syst.*, vol. 28, pp. 15-33 1988.
- [12] J. Yen, L. Wang and C. W. Gillespie, "Improving the interpretability of TSK fuzzy models by combining global learning and local learning", *IEEE Trans. Fuzzy Syst.* vol. 6, no. 4, pp. 530-537 Nov. 1998.
- [13] J. S. R.r Jang, "ANFIS: Adaptive-Network-Based Fuzzy Inference System", *IEEE Trans. Syst. Man, Cybern.*, vol. 23, No. 3, pp. 665-685, May/June. 1993.
- [14] X. Maldague, "Nondestructive Evaluation of Materials by Infrared Thermography", Springer-verlag London Limited, 1993.
- [15] A. Darabi, X. Maldague, "Defect Depth Estimation Using Neuro-Fuzzy System in TNDE," *QIRT*, July 2000 (abstract accepted).

CHAPTER 7

Conclusion

7.1 Summary

In this study, we successfully applied neural network and neuro-fuzzy computing techniques to solve inverse problems of defect detection and depth estimation in TNDE. Over the last few years many approaches were introduced in quantitative infrared thermography and most of them can deal only with specific cases to characterize subsurface defects. The presented results show that neural network and neuro-fuzzy computing methods provide an effective tool for reliable inspection in complex TNDE tasks.

To achieve the proposed method objectives, we first reviewed the 3-D heat conduction problem applied to infrared thermography. The numerical solution of this problem was developed and its result compared with analytical solution for a simple homogeneous specimen case. Our numerical solution is able to model any nonsymmetrical and non-homogeneous sample containing simultaneously many defects in randomly

chosen positions. This numerical modeling was implemented on a parallel architecture such as the MasPar computer. Comparisons made with the analytical solution and with a commercially available software (Thermo-Heat) confirm that our numerical modeling precision is adequate to simulate TNDE tasks.

Two neural networks were next proposed as defect detector and defect depth estimator. These were trained by back-propagation learning algorithm using simulated thermal contrast as input signals. To converge efficiently the proposed neural networks, we used Levenberg-Marquardt learning rule. Although, this learning rule is fast and converges upon a stationary point which may be global minima, it needs a high capacity memory and long training time. Both detector and estimator networks were tested with simulated and real experimental data.

The detector network was able to reveal all defects in most of the modeled cases and in two experimental samples. The deepest defect was located 3 mm under the sample surface even if the training set included defects with only depths up to 1.1 mm (CFRP samples with TeflonTM defects). It was also shown that the detector network is robust to noise: correct detection rate dropped from 96.4% for simulated data to 88.8% for simulated data contaminated with white noise ($\mu = 0$ and $\sigma = 0.054$). Another experiment showed that the detector network is sensitive to defect thermal properties. For instance the network was trained with data extracted from samples including air delamination defects and was then presented data extracted from samples containing TeflonTM defects. In such a case the detector network revealed nothing defective. This could be used with profit in some applications.

The depth estimator results showed that if the network is provided with appropriate and representative training data then supervised neural network can estimate defect depth with required precision (depending on modeling geometrical parameters). The experiments on a simulated sample including T-shape air defect demonstrated that the estimator network is able to evaluate the defect pixels depth with 12% of average relative estimation error. The estimator network could not measure both circular defect at depth 2 and 3 mm in the case of the experimental sample represented in Figure 5.16 due to their depth but nevertheless it

was able to evaluate defect depth for the sample shown in Figure 5.15. This was due to limited availability of the training set for the estimator network for the samples contained Teflon™ defects.

As mentioned previously, the backpropagation learning algorithm suffers from convergence to local minima unless we use rules such as Levenberg-Marquardt learning rule to guarantee the network to converge to global minima, (this requires more computer memory and training time). To benefit from low-level learning and computational power of neural networks and advantages of high-level human-like thinking of fuzzy systems, we next proposed a depth estimator based on neuro-fuzzy modeling systems. The neuro-fuzzy system used in this work is called Adaptive-Network-based Fuzzy Inference System (ANFIS). It employs the Takagi-Sugeno-Kang (TSK) inference method to establish output results. ANFIS uses an hybrid learning rule in which the gradient method and the least squares estimate (LSE) are combined to identify the system parameters. This hybrid learning rule can decrease the dimension of the search space, cut down substantially the convergence time and guarantee to find the global minimum point.

The proposed neuro-fuzzy depth estimator was also tested on both simulated and experimental data. This new quantitative TNDE method provides better results as compared to the neural network based depth estimator. The average relative estimation error was measured as 8.7% over a T-shape air defect with neuro-fuzzy depth estimator while it was measured as 12% for the same sample with neural network based depth estimator. Experimental tests were carried out with both depth estimators as illustrated in Figure 5.22 and Figure 6.19. Comparing these figures, we conclude that the defects outline are better determined with neuro-fuzzy depth estimator with a depth value of about 0.3 mm for both cases. It should be noted that the neural network based depth estimator was trained with the full thermal contrast curve as input which contains 16 sampling points while we trained the neuro-fuzzy depth estimator with only maximum, half-maximum contrast points and their occurrence time as input vector. If we apply maximum, half-maximum contrast points and their occurrence time as input vector to the neural network based depth estimator, its results would be worse and in many cases it would not be possible to detect

subsurface defects. However, neuro-fuzzy depth estimator is too sensitive to noise as compared to neural network depth estimator.

7.2 Contributions

The main accomplished contributions of this research are:

- 3-D heat conduction numerical modeling applied to asymmetrical and non homogenous samples in TNDE and its implementation on a parallel architecture [1].
- Analytical solution of the heat conduction problem applied to pulsed thermography [1].
- Neural network based defect detector and depth estimator applied to non homogenous samples such as Carbon Fiber Reinforced Plastic (CFRP) in TNDE, modeling, noise study and experimental tests. [2], [3]
- Neuro-fuzzy based defect depth estimator applied to non homogenous samples such as CFRP in TNDE, modeling and experimental test [4].

7.3 Future work

The 3-D heat conduction modeling applied to pulsed thermography was developed on the MasPar parallel architecture now out of order. Therefore, the program should be adapted to sequential computer or to another existing parallel architecture. The program should also be modified to simulate samples containing mixed defects (defect with different thermal properties). This would provide extensive data set to train neural networks or fuzzy systems allowing to better design neural networks or fuzzy system as defect classifiers.

The training procedure of multilayer perceptron neural networks using back propagation algorithm is slow and uncertain. This causes on-line quantitative procedure to be an obstacle in on-line TNDE. To overcome this problem some modified algorithms such as NN-MLP (nearest-neighbor-based multilayer perceptron) could be employed instead. In this research work, the training sets were extracted by human intervention from simulated

data in relatively simple cases. Thus an automated method should be used to extract training data sets for more complex cases using for instance dedicated algorithms.

Finally it would be interesting to make use of PPT (Pulsed Phase Thermography) data or entire contrast curve data as input to the fuzzy depth estimator. This can be another open research work in quantitative TNDE.

7.4 References

- [1] A. Darabi, X. Maldague, "Thermal Modeling in TNDE," CSNDT J. (in preparation).
- [2] Y. Largouët, A. Darabi, X. Maldague, "Depth Evaluation in Pulsed Phase Thermography with Neural Network," Review of Progress in Quantitative NDE, D. O. Thompson et D. E. Chimenti eds, Plenum 18A: 611-617, 1998
- [3] S. Vallerand, A. Darabi, X. Maldague, "Defect Detection in Pulsed Thermography: A Comparison of Kohonen and Perceptron Neural Networks," SPIE: Thermosense XXI, R. N. Wurzbach, D. D. Burleigh eds., 3700: 20-25, Orlando, Fl, April 1999.
- [4] A. Darabi, X. Maldague, "Defect Depth Estimation Using Neuro-Fuzzy System in TNDE," QIRT, July 2000 (abstract accepted).

APPENDIX

The Analytical Solution of the Heat Conduction Problem Programming Code

$$T(0, t) = \frac{QL}{k_z} \left(Fo + \frac{2}{\pi^2} \sum_{m=1}^{\infty} \frac{1}{m^2} (1 - e^{-m^2 \pi^2 Fo}) \right) \text{ for } 0 < t < \tau_h \quad (\text{A.1})$$

$$T(0, t) = \frac{QL}{k_z} \left(Fo_h + \frac{2}{\pi^2} \sum_{m=1}^{\infty} \frac{1}{m^2} \left(e^{-m^2 \pi^2 (Fo - Fo_h)} - e^{-m^2 \pi^2 Fo} \right) \right) \text{ for } t > \tau_h \quad (\text{A.2})$$

The Analytical Solution to the Heat Conduction Problem expressed by Eqs. (A.1) and (A.2) has been written on Matlab software as follow:

```

%*****
%
% Analytical Solution of Transient Heat Conduction
% Problem Applied to TNDE
%
% Author : Akbar Darabi
%
```

```

% Date: March 12th 1998
%
%*****
%
function [Temperature,
Time]=analytic_solution(alpha,Q,Hc,L,kz,l,n,z,Tpulse,deltat,tho1,tmax)

%Initialization Parameters
% For Example: alpha=0.42*(10^(-6)); Q=100000; Hc=20; L=0.002;kz=0.8; l=0.001;
n=100; z=0; Tpulse=0.5; deltat=0.06; tho1=0.5;tmax=5.5;

% Initialization

Time=0:deltat:tmax;
Foh=(alpha*Tpulse)/(L^2);

temp=0;

% Surface Temperature Computation

for kk=1:length(Time)

    temp1=0

    if (Time(kk)<tho1)

        for mm=1:n
aa=1/(mm^2);
bb=1-exp(-(mm^2)*(pi^2)*(alpha*Time(kk))/(L^2));

            temp1=temp1+aa*(bb);
        end
    else

        for mm=1:n
aa=1/(mm^2);
bb=exp(-(mm^2)*(pi^2)*(alpha*Time(kk))/(L^2));
cc=exp(-(mm^2)*(pi^2)*(alpha*(Time(kk)-tho1))/(L^2));

            temp1=temp1+aa*(cc-bb);
        end
    end
end

```

```
temp=((Q-Hc*temp)*L/kz)*(Foh+(2/(pi^2))*temp1);  
Temperature(kk)=temp;  
end  
  
% Displaying  
  
figure  
plot(Time, Temperature, 'O-k')  
hold on  
  
xlabel 'Time (s)'  
ylabel 'Temperature \circC'  
legend('Analytic Solution')
```